Nanoscale Electronic Properties in GaN Based Structures for Power Electronics Using Electron Microscopy

by

Shanthan Reddy Alugubelli

A Dissertation Presented in Partial Fulfilment
of the Requirement for the Degree
Doctor of Philosophy

Approved November 2019 by the
Graduate Supervisory Committee:

Fernando A. Ponce, Chair
Martha McCartney
Nathan Newman
Yuji Zhao

ARIZONA STATE UNIVERSITY

December 2019

ABSTRACT

The availability of bulk gallium nitride (GaN) substrates has generated great interest in the development of vertical GaN-on-GaN power devices. The vertical devices made of GaN have not been able to reach their true potential due to material growth related issues. Power devices typically have patterned *p-n*, and *p-i* junctions in lateral, and vertical direction relative to the substrate. Identifying the variations from the intended layer design is crucial for failure analysis of the devices. A most commonly used dopant profiling technique, secondary ion mass spectroscopy (SIMS), does not have the spatial resolution to identify the dopant distribution in patterned devices. The possibility of quantitative dopant profiling at a sub-micron scale for GaN in a scanning electron microscope (SEM) is discussed. The total electron yield in an SEM is shown to be a function of dopant concentration which can potentially be used for quantitative dopant profiling.

Etch-and-regrowth is a commonly employed strategy to generate the desired patterned *p-n* and *p-i* junctions. The devices involving etch-and-regrowth have poor performance characteristics like high leakage currents, and lower breakdown voltages. This is due to damage induced by the dry etching process, and the nature of the regrowth interface, which is important to understand in order to address the key issue of leakage currents in etched and regrown devices. Electron holography is used for electrostatic potential profiling across the regrowth interfaces to identify the charges introduced by the etching process. SIMS is used to identify the impurities introduced at the interfaces due to etch-and-regrowth process.

To Venky, Paddu, and Srilu

ACKNOWLEDGEMENTS

I would like to express my sincerest gratitude to Prof. Fernando A. Ponce for his support and style of advising throughout my time here at ASU. I was always given the freedom to formulate my own problem statement and explore the topic at my own pace. The discussions with him have greatly broadened my perspective of the field. I am greatly indebted to Dr. David Smith for recommending me to Dr. Ponce. I would like to deeply thank Prof. Martha McCartney for guiding me through the experimental electron holography, her continual support, and all the interesting discussions we had. I would like to acknowledge all the valuable discussions with Prof. Robert Nemanich. I would like to acknowledge our collaborators Prof. Yuji Zhao and his students Houqiang Fu and Kai Fu, for all the interesting devices which enabled this work. I would like to acknowledge Dr. Shery Chang for training me on the Titan microscope. I would like to acknowledge my group members Alec Fischer, Hongen Xie, Shuo Wang, Hanxiao Liu, and Po-Yi Su for their constant support throughout my time at ASU. I would like to thank Karl Wiess, Ken Mossman, Sisouk Prasavath for all their help with the microscopes, and sample preparation processes. I would like to thank my friends and family who have been the support system throughout this fascinating journey. A great shout out to awesome lunch discussions with my dear Desi gang. I acknowledge the use of facilities within the Eyring Materials Center at Arizona State University.

TABLE OF CONTENTS

Page

ACKNOWLEDGEMENTS iii

LIST OF TABLES vii

LIST OF FIGURES viii

CHAPTER

1. INTRODUCTION 1

1.1 Fundamentals of Power Electronics 2

1.2 *p-n* vs *p-i-n* Junctions 5

1.3 Gallium Nitride for Power Electronics 7

2. CHARACTERIZATION TECHNIQUES 11

2.1 Electron Microscopy 12

2.2 Scanning Electron Microscopy 15

2.2.1 Instrumentation 15

2.2.2 Electron Specimen Interaction 16

2.2.3 Electron Yields 19

2.2.4. Detection of Secondary Electrons 21

2.3 Transmission Electron Microscopy 23

2.3.1 Instrumentation 23

2.3.2 Electron Scattering in a TEM 26

2.3.3 Bright Field, Dark Field, and High Resolution Imaging 27

2.4 Electron Holography 28

2.4.1 Instrumentation 30

CHAPTER Page

2.4.2 Interference and Holographic Fringe Formation 31

2.4.3 Reconstruction of Phase and Amplitude 35

2.4.4 Electrostatic Potential From the Phase 38

2.4.5. Sample Preparation for Electron Holography 40

2.5 Secondary Ion Mass Spectroscopy (SIMS) 45

2.5.1 Introduction to SIMS 45

2.5.2 Magnetic Sector Mass Analyzer 49

2.5.3. Depth Resolution and Sensitivity 52

2.5.4. Quantitative Impurity Analysis in GaN With O_2^+ or Cs^+ as Primary Ions . 55

3. DOPANT PROFILING OF *P-I-N* GAN STRUCTURES IN SEM 60

3.1 Introduction 60

3.2 Experimental 62

3.2.1 Sample Preparation 62

3.2.2 Secondary Electron Detection and Imaging 62

3.2.3 The Specimen as a Detector 63

3.3 Results and Discussion 64

3.3.1 Dopant Contrast Using SE Detector at Various Primary e-beam Energies . 64

3.3.2 SE Yield Dependence on e-beam Energy for *p*-, *i*-, and *n*-GaN 65

2.3.3 SE Yield Dependence on Mg Concentration in *p*-GaN 68

3.3.4 Effect of the Nature of the Surface on Secondary Electron Emission 69

3.3.5 Effect of Beam Dwell Time and Exposure Time 71

3.3.6 Applications on High Power Devices 72

CHAPTER Page

4. STUDY OF ETCH AND REGROWN INTERFACES IN GAN *P-I-N* STRUCTURES 77

4.1 Introduction 77

4.2 Experimental Details 79

4.2.1 Reactive Ion Etching of GaN 79

4.2.2 Samples for Electron Holography Studies 81

4.3 I-V and C-V Measurements of GaN *p-i-n* Structures 82

4.4 TEM and SIMS Studies on GaN *p-i-n* Structures 86

4.4 Electrostatic Potential Analysis on GaN *p-n* Junction 91

4.5 Electrostatic Potential Analysis on GaN *p-i-n* Junctions 92

4.5.1 Un-interrupted GaN *p-i-n* Structures 92

4.5.2 Etched and Regrown GaN *p-i-n* Structures 94

4.5.4 Etched and Regrown GaN *p-i* Junction with an Insertion Layer 102

4.6 Conclusion 103

5. CONCLUSIONS AND OUTLOOK 104

5.1 Dopant Profiling using SEM 104

5.2 Etched and Regrown GaN *p-i-n* Diodes 106

REFERENCES 108

APPENDIX

A. LIST OF PUBLICATIONS DURING THE STUDY TOWARDS THE DOCTORAL DEGREE 116

LIST OF TABLES

Table Page

2.1. List of Characterization Techniques Used in This Work and Their Purpose 12

2.2 Comparison of Wavelength and Resolution for Microscopy Using Light and Electrons as Probing Sources 12

2.3. Comparison of Thermionic and Field Emission Electron Gun 25

2.4. Polishing Parameters for Wedge Polishing TEM Specimen 42

2.5. Secondary Ion and Molecular Species Monitored for Identification of Impurities in GaN Matrix with O_2^+ and Cs^+ Beams. 56

4.1. Parameters for ICP Etching of GaN 80

LIST OF FIGURES

Figure Page

1.1. Analogy of a Transistor with a Gate, Source, and a Drain 2

1.2. Specific On-Resistance vs. Breakdown Voltage for Various Materials 3

1.3. Examples of Devices with Vertical and Lateral Architectures 4

1.4. Typical I-V Characteristics of a P-N Diode 5

1.5. Net Doping Density and Drift Layer Thickness Estimated for Desired Breakdown for GaN *P-I-N* Diodes 7

1.6. Example of a GaN VJFET with Typical Voltages at the Source, the Drain and the Gate 9

2.1. Schematic Diagram Showing Various Signals Generated Due to Primary Electrons with the Sample 14

2.2 Schematic Diagram of a Scanning Electron Microscope 15

2.3. Schematic Diagram Showing Interaction Volume of Electrons in a Sample. Maximum Penetration Depth of Electrons in GaN 17

2.4. Typical Energy Distribution of Emitted Electrons for a Material Excited with 2 kV Electron Beam. 18

2.5 Typical Electron Yield Distribution as a Function of Primary Beam Voltage 20

2.6. Experimentally Measured Secondary (δ) and Backscattered Electron Yield (η) for Various Elements 21

2.7 Schematic Diagram of an Everhart-Thornley Type SE Detector 22

2.8. Schematic Diagram of a TEM in Imaging Mode and Diffraction Mode. 24

Figure Page

2.9. Schematic Diagram of an Off-Axis Electron Holography Setup..... 30

2.10 Geometric Arrangement of a Biprism in the Microscope Column..... 32

2.11 Electron Wave Interference Pattern for the Beam Passing Through (a) Specimen (b) Vacuum. (c) Line Profile of Reference Hologram with a Fringe Spacing Of ~ 1.7 nm 35

2.12. FFT of a Hologram Showing Center and Side Bands..... 36

2.13. Bonding of 1.5 X 2.5 mm Wafer Pieces for TEM Specimen Preparation..... 41

2.14. Schematic Diagram of a Sample on a Molybdenum (Mo) Grid..... 43

2.15. Schematic Diagram of the Magnetic Sector Cameca IMS 6f SIMS Instrument. 46

2.16. Collision Cascade Set in by the Interaction of Primary Ions with the Sample. 48

2.17. Schematic Diagram of Magnetic Sector Double Focusing Mass Analyzers, Including Electrostatic Analyzer (ESA), and Magnetic Sector (MS). 51

2.18. Schematic Diagram of Evolution of Intermixing in a Target Matrix Under the Impact of High Energy Primary Beam. 52

2.19. Schematic Diagram of a Monolayer (Red Layer) Being Smeared as the Crater is Being Dug from Left to Right. 53

2.20. True Dopant Concentration vs. Measured Dopant Concentration in SIMS 54

2.21. As Obtained Sims Data Obtained from a GaN Matrix for Different Species Using O_2^+ as Primary Beam..... 57

Figure Page

2.22. Magnified View of Signals from Ga, N and Mg Ions Shown in the Fig. 2.21. Primary Current Drift is Reflected in the Matrix Element Counts. 59

3.1. Schematic Diagram of Electronic Currents Flowing in and out of a Specimen in An SEM. 64

3.2. SE Image and SE Emission Intensity Profile of The *P-I-N* Gan Structure Acquired at 2 kV and Beam Current of 53 Pa 65

3.3.(A) Variation in Electron Yields For *p*-GaN, *n*-GaN, And *i*-GaN Plotted for Primary E-Beam Energies Ranging From 0.25 kV To 12 kV. (B) SE Yield Difference Between *p*-GaN and *n*-GaN For Corresponding E-Beam Energies. Inset Shows SE Images of *P-I-N* Structure At 0.25 kV, 2 kV, And 5 kV. 67

3.4. Schematic Diagram of Band Bending Near the Surface for *p*-GaN, And *n*-GaN. 68

3.5. Electron Emission Characteristics for Mg-Doped GaN. (A)Variation in Electron Yields as a Function of Primary E-Beam Energy for Various Mg Concentrations. (B) SE Emission Intensity Dependence on Mg Concentration for Different Primary E-Beam Energies. 69

3.6. SE Emission Intensity Profiles, and Images of a *P-I-N* GaN Structure with Surfaces that were Exposed to Air for 2 Days, Exposed to UV for 2 Hours, and Treated with HF After UV Exposure. 70

Figure Page

3.7. SE Emission Contrast (C_{pn}) of *P-N* GaN Structures, for Primary E-Beam Energies of 2 kV, 5 kV, and 10 kV: (A) As a Function of Electron Dose for a Single Scan. (B) As a Function of Total Exposure Time with an Electron Dose Rate of 30 μc/cm^2.s. The Raster Area in These Measurements is 15.5 μm X 11.7 μm. 72

3.8. SE Images of (A) Etched-And-Regrown *P-I-N* GaN Mesa Structure, (B) As-Grown *p*-GaN, (C) H_2 + RTA Annealed *p*-GaN. 73

3.9. (A) Schematic View of the Cross-Section of the Epilayers. (B) Fabrication Process for the Devices with Guard Rings. (C) Cross-Sectional Schematics of the Devices with GR. (D) Optical Microscopy Image (Top View) of the P-N Diodes with 10 GR. (E) SEM Images of the Cross-Section of the Devices with GR 74

3.10. Schematic Diagram of Trench Structures for Study of Leakage Current Dependence on the Trench Depth 75

3.11. Dopant Profiles of Trench Structures with Different Etch Depth..... 76

4.1. I-V Characteristics of Different GaN *P-I-N* Structures 83

4.2. Temperature Dependent I-V Characteristics of GaN *P-I-N* Structures with *p*-GaN Grown Directly Over Etched *I*-GaN in (A) Forward Bias (B) Reverse Bias 84

4.3. C-V Measurements for Regrown GaN *P-I-N* Diodes with and without Insertion Layer. 85

4.4. Two Beam Bright Field Images of Continuously Grown GaN *P-N* Junction with Different Mg Concentrations 86

Figure Page

4.5. Two Beam Bright Field Images of *P*-GaN Grown Directly over Etched *i*-GaN Surface for Different Mg Concentrations. Structure Schematic Diagram is Indicated. 87

4.6. High Resolution Image of Interface Region with *p*-GaN Grown Directly over Etched *i*-GaN. 87

4.7. SIMS Analysis of Mg, Si, C, and O Impurities on Etched-And-Regrown Structure Shown in the Inset 88

4.8. (A), (B) Mg And Si Profiles Obtained Simultaneously With O_2^+ Beam. (C), (D) Si, O, And C Profiles Obtained With Cs^+ Beam. The Structure is Indicated. These Measurements are Performed at ASU 89

4.9. Two Beam Bright Field Images of (A) *i*-GaN Regrown on Etched *i*-GaN Surface (B) *P*-Gan Grown on Etched *i*-GaN with a Thin Un-Doped Layer Between Them. (C), and (D) Show the SIMS Profiles of Mg, and Si Corresponding to Structures (A), and (B) 90

4.10. Electrostatic Potential of a Simple GaN *P-N* Junction Grown on 0.35° Mis-Cut GaN Substrate. 91

4.11. Electrostatic Potential Profile of Continuously Grown GaN *P-I-N* Structure with *i*-Gan Layer Thickness of (A) 10 μm (B) 0.1 μm. Inset Shows the Epilayer Structure. The Phase Image for the Structure in 1(B) is Shown Here..... 93

4.12. SIMS Profiles of Mg at the *P-I* Interface of Etched-and-Regrown GaN *P-I-N* Structures Corresponding to the *p*-GaN Layers with Mg Concentrations of 1, 3, and $7x10^{19}$ cm^{-3}. Notice Peak in the Mg Concentration Indicating Mg Accumulation at the Regrowth Interface. 95

Figure Page

4.13. (A) Electrostatic Potential Profile Indicating Accumulation of Negative Charge at the *i*-GaN and Positive Charge at the *p*-GaN Regions Next to the *P-I* Interface. Estimated Charge Densities Near the Regrowth Interfaces are Indicated on the Image. (B) SIMS Profiles of Mg, Si, C, and O at the *P-I* Interface of an Etched-and-Regrown GaN *P-I-N* Structure 96

4.14. Schematic Diagram Showing In-Plane and Out of Plane Tilt of the Interface with Respect to the Electron Beam. 98

4.15. Energy Profiles of a *p*-GaN Grown Directly Over Etched *i*-GaN Surface with Out of Plane Tilt of ~0.5^0 and ~1^0 Toward c-Axis. Extracted Phase for Each of the Energy Profiles are Shown, Where a Bright Band Can be Cleared Observed at the Interface 99

4.16. Potential Energy Profiles of a *p*-GaN Grown Directly Over Etched *p*-GaN Surface With Out of Plane Tilt of ~0.5^0 and ~1^0 Away From c-Axis. Extracted Phase for Each of the Energy Profiles are Shown, Where a Bright Band Can be Cleared Observed at the Interface. 100

4.17. Etched-and-Regrown GaN *P-I-N* Structure With 50 mm Undoped GaN Insertion Layer. Inset Shows the Epi-Layer Structure. (A) Electrostatic Potential Profile of the *P-I* Interface. Charges Near the Regrowth Interfaces are Indicated. (B) SIMS Profiles of Mg And Si. Corresponding Phase Image is Shown Here..... 102

5.1 Effect of Beam Current on the Contrast Reversal Between *p*-Layer and *n*-Layer. .. 105

1. INTRODUCTION

Electricity accounts for 40% of the total energy consumption in US in 2011, and this proportion may increase to 60% due to the growing use of data centers, hybrid electric vehicles and other transportation systems.[1,2] About 80% of all the electricity is expected to pass through a power electronic device between generation and consumption by 2030, which is twice the amount today. Current state-of-the-art power devices are made of silicon-based thyristors, field effect transistor or Insulated gate bipolar transistor designs. Recent studies show that around 10% of the annual worldwide power consumption is wasted in inefficient power conversion.[3] This is comparable to the total power generated by renewable energy sources, which brings in the need for efficient power conversion devices.

With the current rise in the use of data storage centers and electric vehicles, the demand for electric power converters is expected to grow continuously. With such applications, power conversion efficiency will be crucial. A power converter typically consists of a semiconductor switch and passive components. With the use of wide band gap semiconductors, the size of the passive components can be greatly reduced. This reduction in size is very advantageous for applications like electric vehicles where reduced size translates to increased fuel efficiency. Also, wide band gap semiconductors have lower operation temperatures that reduce the amount of heat sink.[4] This is very advantageous for applications like data centers where system cooling costs are significant.

1.1 Fundamentals of power electronics

A power semiconductor device is a key component in power electronics. Figure 1.1 shows an analogy of a simple transistor consisting of a source, a drain, and a gate. The purpose is to control the flow of electrons between the source, and the drain using a gate. Ideally, the transistor should have no resistance to current flow in the on-state, and it should be able to withhold the specified blocking voltage without any leakage currents.

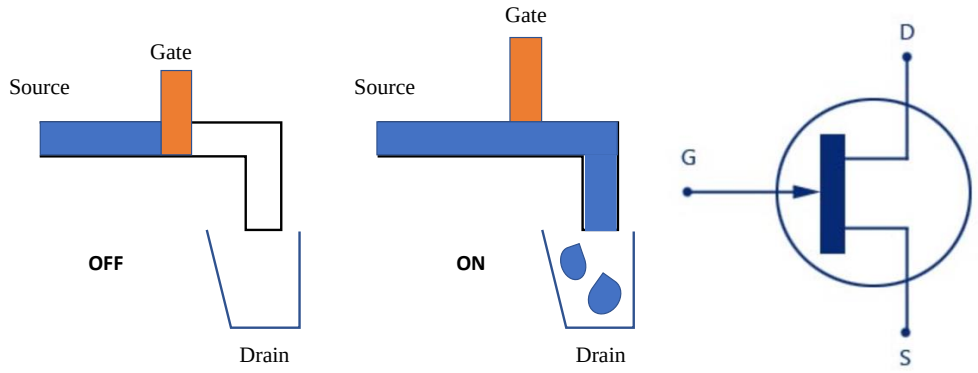

Figure 1.1. Analogy of a transistor with a gate, source, and a drain.

Current control in devices is achieved by using differently doped regions as source, drain, and gate. For example, a GaN based Vertical Junction Field Effect Transistor (VJFET) has a *p*-GaN region as the gate, an intrinsic region as the drift layer, and *n*-GaN regions acting as the source and the drain.[5]

An ideal power semiconductor device should have low on-state resistance (R_{on}) and large breakdown voltage (V_{BD}) in the off-state.[6] These parameters would depend on the material properties like band gap (E_g), and carrier mobility (μ_e). The choice of the material significantly affects the design, and the performance of devices. Table 1 shows relevant material properties of semiconductors commonly used in power electronics.

Table 1.1. Material properties of semiconductors commonly used in power electronic devices. Eg is the bandgap, μ_e is the electron mobility and Ec is the critical electric field.

Material	E_g (eV)	μ_e (cm^2/V.s)	E_c (MV/cm)
Si	1.1	1400	0.3
GaAs	1.4	8500	0.4
SiC	3.26	900	2.2
GaN	3.4	1200	3

The relation between the on-state resistance, the breakdown voltage, and the material properties is given by[6]

$$R_{on} = \frac{4 {V_{BD}}^2}{\varepsilon_S \mu_e {E_c}^3}$$

Both R_{on}, and V_{BD} increase with increasing drift layer (low doped layer) thickness. Figure 1.2 shows the calculated specific on-resistance (R_{on}) versus the breakdown voltage of some common materials used for power electronics. For the same R_{on}, materials with wider band gap can reach higher breakdown voltages.

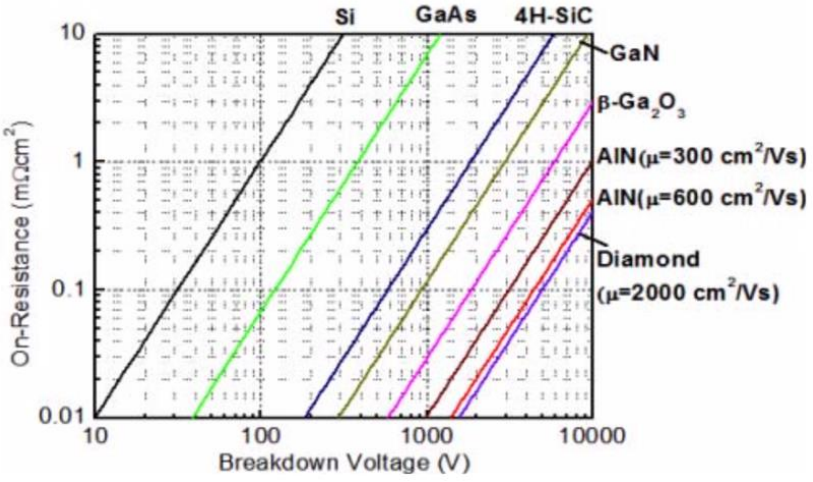

Figure 1.2 Specific on-resistance vs. breakdown voltage for various materials (Adapted from Ref. 7)

Traditionally, power electronics are made using silicon and SiC due to the availability of respective bulk substrates, and well-established processing technology.[1] Such substrates can help realize vertical architectures which are best suited for high power applications. In vertical devices, the blocking voltage is held vertically in the drift region between the source, and the drain. In lateral devices, the blocking voltage is held laterally between the source, and the drain.[7] Figure 1.3 shows examples of a vertical device and a lateral device. Vertical device architecture can help achieve higher breakdown voltages compared to lateral architectures. Significant improvements in size, efficiency, weight, and power density of systems has resulted from the improved performance of silicon-based power semiconductor devices.[8] However, devices based on silicon are rapidly approaching the fundamental material limits. Also, SiC based Schottky diodes have matured and are commonly used in applications requiring high efficiency. There has been a great interest in developing GaN based power electronics due to its superior material properties as compared to that of Si, and SiC.

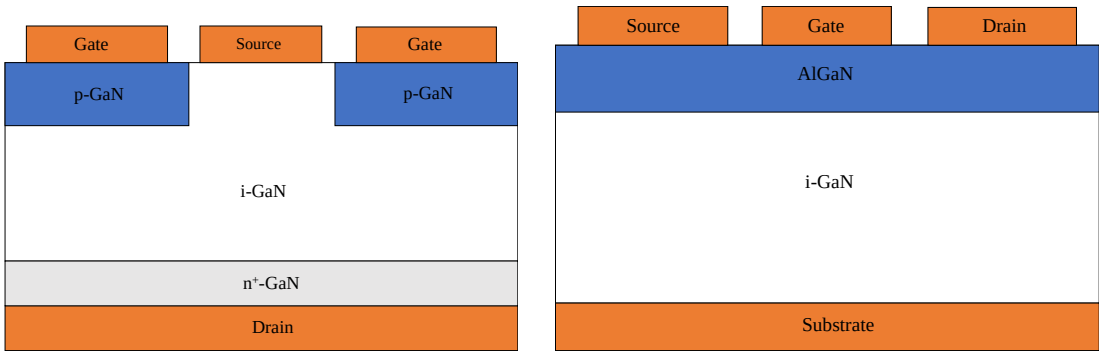

Figure 1.3 Examples of devices with vertical and lateral architectures.

1.3. *p-n* vs *p-i-n* junctions

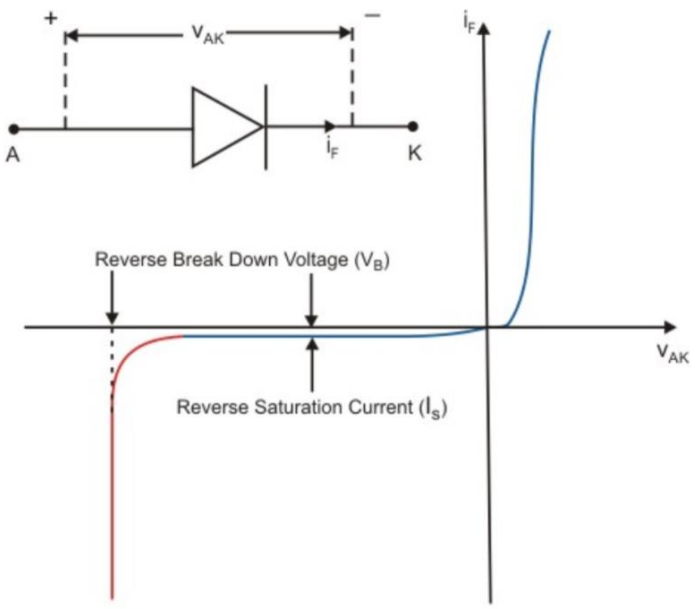

Figure 1.4 Typical I-V characteristics of a *p-n* diode.

Typical I-V characteristics of a simple *p-n* junction are shown in Fig. 1.4. Under forward bias, i.e. the p side at higher positive potential than the n side, the potential barrier is lowered, and a very large number of minority carriers are injected on both sides of the junction. The injected minority carriers eventually recombine with the majority carries as they diffuse further into the electrically neutral drift region.

Under reverse bias, the p side at higher negative potential than the n side. This reverse bias adds to the height of the potential barrier. The electric field strength at the junction and the width of the space charge region (depletion region) increase due to the absence of free carriers. On the other hand, the free minority carrier densities will be zero at the edge of the depletion region on either side. This gradient in minority carrier density causes a small flux of minority carriers to diffuse towards the depletion layer where they

are swept immediately by the large electric field into the electrical neutral region of the opposite side. This will constitute a small leakage current across the junction from the n side to the p side. There will also be a contribution to the leakage current by the electron hole pairs generated in the space charge layer by the thermal ionization process. These two components of current together is called the reverse saturation current I_s of the diode. Value of I_s is independent of the reverse voltage magnitude (up to a certain level) but extremely sensitive to temperature variation. When the applied reverse voltage exceeds some threshold value (for a given diode) the reverse current increases rapidly. The diode is said to have undergone reverse break down. Reverse breakdown is caused by a process of impact ionization. During impact ionization electrons are accelerated by the large depletion-layer electric field due to the applied reverse voltage that may attain sufficient energy to liberate another electron from the valence band of the material.[6] The liberated electron in turn may repeat the process. This cascading effect also called avalanche, may produce a large number of free electrons very quickly resulting in a large reverse current.

In order to hold large blocking voltages, the *i*-layer thickness must be high so as to have large depletion width and lower electric field values. The *i*-layer is also called the drift layer. The net doping density has to be decrease with drift region thickness, to sustain the large blocking voltage. Figure 1.5 shows estimated drift layer doping and thickness assuming an infinite planar junction and an ideal edge termination, with E_C = 3.3 MV/cm and μ_n = 1150 $cm^2/V \cdot s$ for GaN.

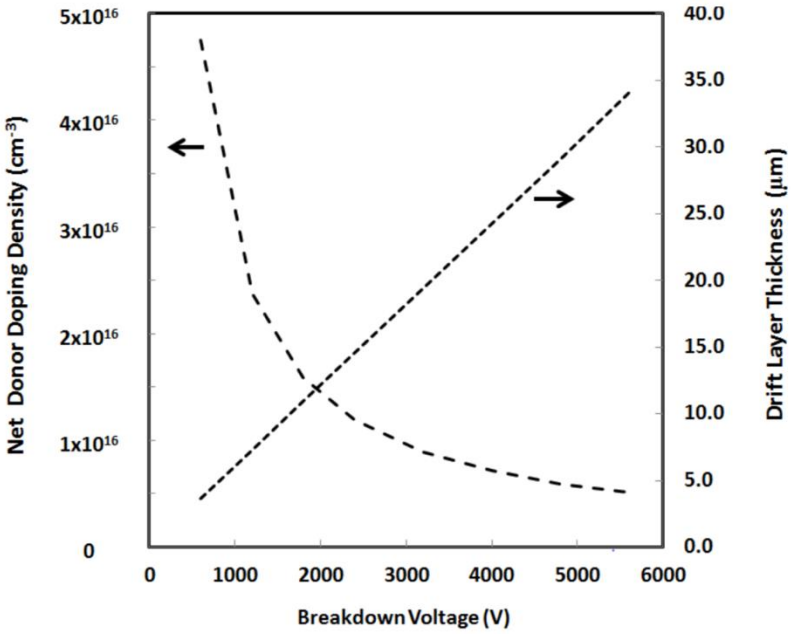

Figure 1.5. Net doping density and drift layer thickness estimated for desired breakdown voltages for GaN *p-i-n* diodes. (Adapted from Ref. 10)

For example, to design a GaN *p-i-n* diode with a breakdown voltage in the range of ~1200V, a drift layer of thickness ~10 μm, and a net doping density of ~1 x 10^{16} cm^{-3} is required.

1.3 Gallium Nitride for power electronics

III-nitride based power electronics have attracted much interest recently due to its superior material properties, and its successful application in light emitting diodes. Sapphire has been the preferred substrate for growth of III-nitrides.[9] Despite high lattice mismatch between the substrate and the epilayers, light emitting diodes produced from the III-nitrides are high performing, durable, and have been successfully commercialized.[9] The situation is different in III-nitride based power electronics on foreign substrates. They have been restricted to lateral architectures due to the unavailability of native substrates. Also,

GaN thin films grown on sapphire have a sub-optimal power device performance due to high dislocation densities (10^8-10^{10}cm^{-2}). The availability of GaN substrates has led to the development of vertical GaN-on-GaN power devices with dislocation densities of about 10^4 -10^6cm^{-2}, resulting in improved performance.[10]

GaN, with a wurtzite crystal structure, is grown either by hydride vapor phase epitaxy (HVPE) and/or organo-metallic vapor phase epitaxy (OMVPE).[11] HVPE is used for growing bulk GaN substrates, and the subsequent epilayers are grown using OMVPE. The GaN substrates used in this study were grown by HVPE with a carrier concentration of ~10^{18} cm^{-3}. In OMVPE, the growth temperature is close to 1000^{o}C at atmospheric pressure for GaN. The precursors were trimethylgallium (TMGa) and ammonia (NH_3), with H_2 as the carrier gas. Bis (cyclopentadienyl) magnesium (Cp_2Mg) and silane (SiH_4) were the sources for Mg and Si. Typically, GaN is grown on c-plane (0001). Given the anisotropy of the crystal, incorporation of Mg may vary with crystal orientation. This is very important for the power devices, where mesa structures are commonly employed. It has been found that the p-GaN grown on the mesa structures has a non-uniform Mg distribution.[12]

Figure 1.6 shows an example of a typical GaN based VJFET grown on GaN substrate which has regions that are doped differently. Knowledge of variations from the intended layer design is helpful in understanding device performance and failure mechanisms. Secondary ion mass spectroscopy (SIMS), routinely used for quantification of dopants in semiconductors, cannot resolve lateral variations, posing a significant challenge for developing advanced GaN power devices. In this dissertation, we show that low-voltage scanning electron microscopy (SEM) can provide an easy solution for

profiling dopant distribution in GaN-based thin film structures. We report on a novel method to quantify the dopants in an SEM using the specimen itself as a detector.

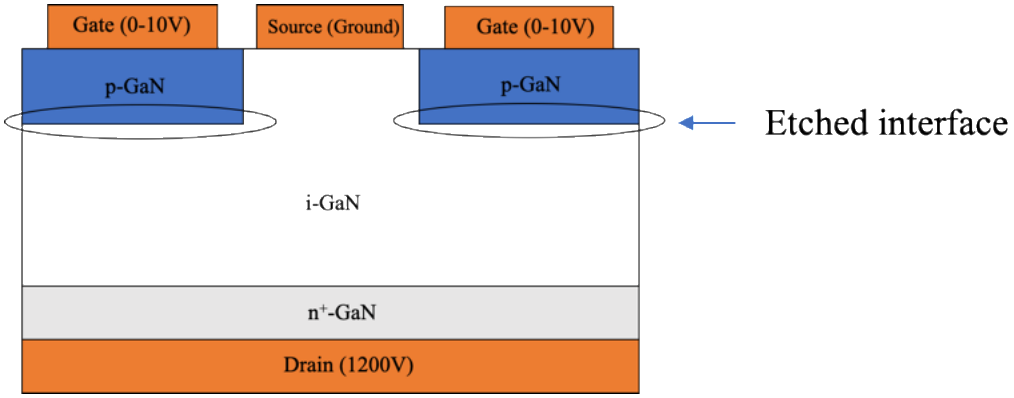

Figure 1.6. Example of a GaN VJFET with typical voltages at the source, the drain and the gate.

Devices with laterally patterned p-i or p-n junctions are typically achieved via etch-and-regrowth, or by ion implantation and annealing.[13,14] Etch-and-regrowth of desired layers offers much higher control in terms of achieving desired layer structure. Also, the doping efficiency is lower for the ion implantation technique. Due to the above-mentioned reasons, etch-and-regrowth is the preferred strategy for achieving patterned p-n junctions.

The VJFET shown in Fig. 1.6 is a normally-off transistor i.e. when there is no voltage on the gate, the *i*-GaN channel (below the source) is depleted resulting in no current flow from source to drain. The channel is conductive when a positive voltage is applied on the gate, thus letting the current pass through the channel. For off-condition, the blocking voltage is held between the gate and the drain, which is a *p*-*i*-*n* diode. A thick *i*-GaN layer is typically used to hold high blocking voltages. The *p*-*i*-*n* diode is typically under a reverse bias. With etch and regrowth, the quality of the interfaces is crucial for efficient operation of the device. Presence of etching damage or impurities near the regrowth interfaces can

result in higher leakage currents and lower breakdown voltages which is undesirable. Despite better theoretical performance characteristics with the patterned device structures, etched-and-regrown devices have higher leakage currents and lower breakdown voltages. For a simple as-grown (no etching) GaN p-i-n structure, the leakage current is about 3 nA at 600 V in reverse bias. The leakage current is about six orders of magnitude higher when the p-GaN is grown on etched i-GaN. It is crucial to understand the nature of the etched and regrown interfaces in order to address the poor device performance.

This thesis consists of five chapters. In the second chapter, the characterization techniques used are discussed in detail. It provides an insight into the working principles, limitations, and a basic framework for the chapters three, and four. In the third chapter, secondary electron (SE) emission from GaN *p-i-n* structures is discussed. SE emission is discussed from various differently doped GaN thin films using the SE detector, as well as the specimen itself as detector. Various factors affecting the SE emission process is discussed. The fourth chapter focuses on etched-and-regrown interfaces. TEM, SIMS, and electron holography are used for structural analysis, determination of impurity accumulation, and electrostatic potential profiling at the regrowth interface, respectively. The effect of the regrowth process on the diode performance is discussed. In the fifth chapter, further possible studies, and improvements for dopant profiling in an SEM, and regrowth process are discussed.

2. CHARACTERIZATION TECHNIQUES

GaN based power device designs consist of lateral and vertical *p*-*n* junctions. Vertical variation in dopant characteristics can be obtained during the growth. For lateral *p*-*n* junctions, some form of selective area doping is necessary. Some of the strategies that have been used for selective area doping are ion-implantation and etch-and-regrowth. In this work, Cl_2 based plasma etching is used for selectively etching trenches in the GaN film, followed by growth of *p*-GaN in the trenches. The etch-and-regrowth process introduces impurities at regrowth interfaces due to the growth interruptions and the etching process itself. Capacitance-voltage (CV) measurements on regrown GaN *p*-*i*-*n* diodes show the presence of charges at the regrowth interface. Also, the ideality factor for a regrown diode is higher than for the regular diode. Thus the etch-and-regrowth process affects the performance of the diodes. It is important to understand the nature of the regrowth interfaces in order to mitigate its effects on device performance. TEM is used to study the structural defects introduced by the etch-and-regrowth process. SIMS is used to identify the impurity accumulation at the interfaces. Any impurity accumulation can result in charge accumulation, which affects the electrostatic potential variations across the interfaces. Electron holography in TEM is used to profile bulk electrostatic potential variations, and charges across the regrowth interfaces. This can help identify the dopant type of the impurities at the interface.

To visualize the layer design of the devices with lateral and vertical *p*-*n* junctions, a technique with a sub-micron spatial resolution, sensitive to dopants is ideal. SIMS does not have the lateral resolution required for the identification of layer design. Scanning electron microscopy can be a great tool for observing dopant contrast as electron beam

provides with the required spatial resolution. The secondary electron emission is sensitive to surface chemistry and to the transport properties of the material, which is affected by doping types and levels. Below is the list of techniques used in this study.

Table 2.1 List of characterization techniques used in this work and their purpose.

Technique	Purpose
Transmission electron microscopy (TEM)	Structure, Electrostatic potential
Scanning electron microscopy SEM	Layer design, dopant profiles
Secondary-ion mass spectroscopy (SIMS)	Impurity, and doping levels

2.1 Electron microscopy

Electron microscopy is a versatile tool to characterize and understand structural, optical, and electronic properties of materials. The advantage of using electrons as a source to probe materials is the superior spatial resolution compared to light or X-ray sources. Typical wavelengths and resolution obtained using various microscopy techniques are listed in the table below.

Table 2.2 Comparison of wavelength and resolution for microscopy using light and electrons as probing sources.

Source	Wavelength	Resolution
Light	400-700 nm	200 nm
Electrons	2-40 pm	Sub nm

The resolution of an optical microscope is limited by the wavelength of the light source. Best obtainable resolution in an optical microscope using a confocal arrangement is about ~200 nm. A system of lenses are used to magnify and capture the images of small objects in an optical microscope. In an electron microscope, an electron gun is used to generate electrons, which interact with the specimen. The de Broglie wavelength of the electrons can be varied from 2 - 40 pm by changing the accelerating voltage of the electrons from 1 - 300 kV. Field emission guns are used to obtain coherent electron beams with high brightness. Given the charged nature of the probing source, electron optical lenses can be used to finely focus the probe. The resolution of the technique is limited by the spherical aberration of the lenses. Depending on the conditions and type of the microscopy, an electron probe with a sub-angstrom resolution is obtainable.[15] Materials can be studied in the length scales ranging from microns down to sub-nanometer which makes it a very versatile tool. Structural, optical, chemical, and potential variations in the specimen are some of the properties that can be studied using electron microscopy. High vacuum is necessary for the electron beam to reach the specimen unimpeded from the electron gun. Typically vacuum inside the microscope column is in the range of 10^{-5} - 10^{-8} Torr.

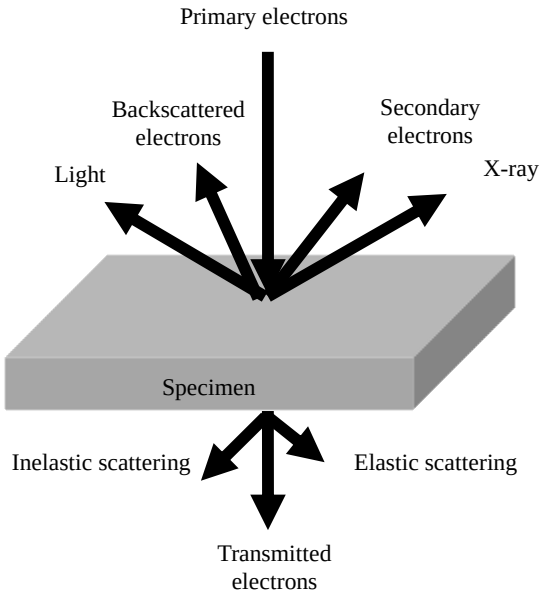

Figure 2.1 Schematic diagram showing various signals generated due to primary electrons with the sample.

There are numerous modes of electron microscopy which have unique advantage depending on the type of the application. Figure 2.1 shows various signals generated as a result of electron specimen interaction. There are various mechanism involved in generating the signals shown in the Fig. 2.1. Various signals can be exploited depending on the mode and setup of the electron microscope. Secondary electrons are typically used for studying the topographical information of the specimen. Backscattered electrons provide information about the composition of the specimen. The characteristic X-rays have chemical information of the material. The light signal generated due to the electron specimen interaction provide information about the local optical properties. If the specimen is sufficiently thin, electrons are transmitted through it, which contain information about the structure. Electrons undergo elastic, and inelastic scattering as they pass through the sample. Elastic scattering involves change in the direction of the electrons without the

change in energy. Coherent elastic scattering is also known as electron diffraction, and it is used for analysis of the crystal structure. Inelastic scattering occurs when there is a loss of energy of the primary electrons due to the interaction with the specimen. The energy loss of the electrons can be analyzed for phonon spectroscopy and chemical information.

2.2 Scanning electron microscopy

In a scanning electron microscope (SEM), a focused electron beam is scanned on the specimen. The electron beam interacts with the specimen producing various signals as shown in the figure 2.1, which are recorded and analyzed.

2.2.1 Instrumentation

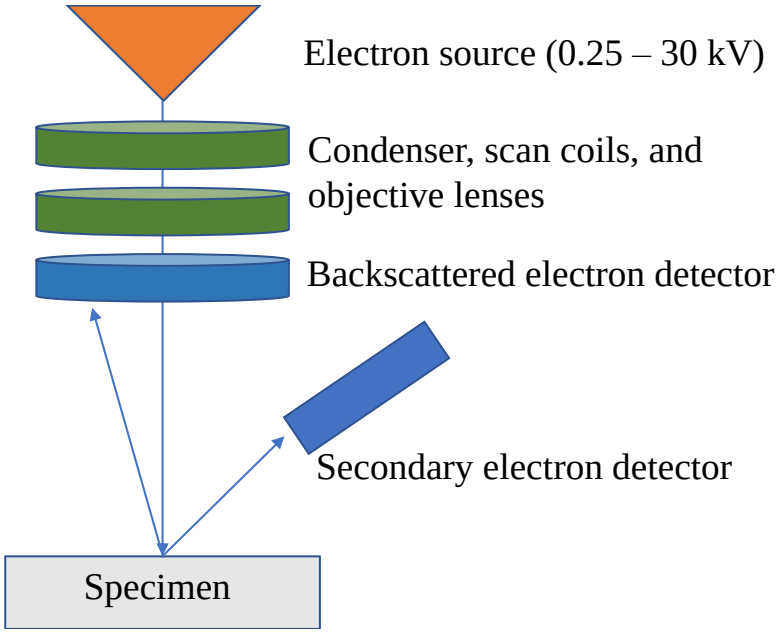

Figure 2.2 Schematic diagram of a scanning electron microscope.

The electron source in an SEM is typically operated in the range of 0.1 -30 kV. Modern SEMs are equipped with a field-emission gun (FEG) which has high coherence, and lifetime as compared to tungsten or LaB_6 filaments.[16] The electron beam passes

through the condenser lens, scan coils, and objective lens before reaching the specimen. The excitation of the condenser lens controls the crossover of the electron beam as shown in Fig. 2.2. With stronger excitation of the condenser lens, electron beam is broader on the objective aperture. Given the size of an objective aperture, the excitation of the condenser lens can control the number of electrons passing through the aperture. Stronger condenser lens excitation results in a lower number of electrons passing through the objective aperture and vice versa. The scan coils control the electron beam by moving the beam in raster format across the specimen. The objective lens focuses the beam before it reaches the specimen. The spot size of the beam is determined by the objective lens. A bad objective lens focusing results in a stigmated beam and produces a blurry image.

2.2.2 Electron specimen interaction

Figure 2.3 shows the typical tear-drop shaped interaction volume of the electron beam with a specimen. In this interaction volume, the primary electrons undergo elastic and inelastic scattering events that result in the generation, and emission of secondary and backscattered electrons. The maximum penetration depth for the primary electrons in a material is a function of the electron beam accelerating voltage. The penetration depth as a function of the accelerating voltage for electrons in GaN is shown in the figure. Some of the electrons undergo inelastic scattering events that result in a complete reversal of their direction; they are called backscattered electrons. Monte Carlo simulations show that, a significant proportion of incident electrons undergo this type of scattering.[17]

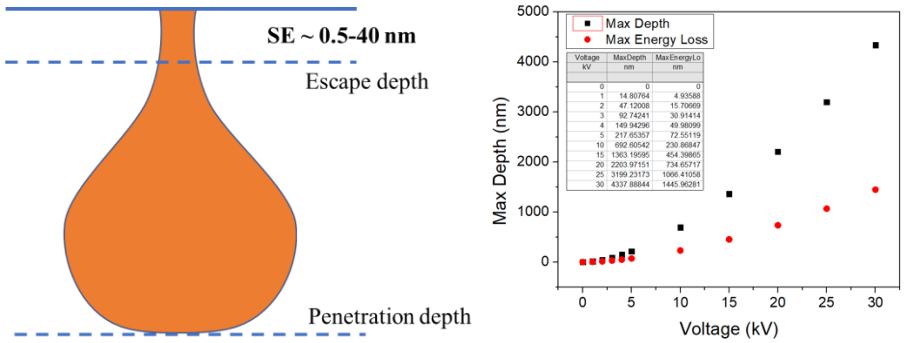

Figure 2.3. Schematic diagram showing the interaction volume of electrons in a sample. The maximum penetration depth and energy loss of electrons in GaN as a function of primary beam voltage is plotted to the right.

Secondary electrons are created when the electron undergoes inelastic scattering ejecting weakly bound valence electrons in case of covalent or ionic materials, and conduction band electrons in the case of metals, which have binding energies below 15 eV to the atoms in the material. Secondary electrons are created throughout the range (penetration depth) of the electrons in the material. Given their low kinetic energies, only a certain fraction of these electrons reach the surface, and are emitted into the vacuum.

The escape depth of secondary electrons depends on the type of material being studied. It is an important parameter to understand the SE emission. This work primarily focuses on SE emission through electron beam excitation. Kanaya et al have calculated the escape depths of electrons in high secondary yield insulators like Al_2O_3, and MgO to be ~12 nm, and ~ 22 nm.[18] In certain studies, it has been argued that the escape depth of secondary electron can be as large as ~18 to 41 nm for MgO, and ~ 23 nm for Al_2O_3.[19,20] High escape depths for MgO is understood as the reason for high secondary electron yields. The wide band gap in an insulator prevents low-energy secondary electrons from losing

energy through electron-electron collisions, thereby resulting in a large escape depth for the secondary electrons, and a large secondary electron yield.[21] The probing depth in photoemission electron microscopy of Ag over layers deposited on Fe was reported to be 16.2 nm.[22] Thus, the escape depths may have a wide range of values depending on the material system, and the surface properties.

A typical energy distribution of the emitted electrons is shown in the Fig. 2.4. The electrons in the lower energy range of the distribution, typically below 50 eV are defined as the secondary electrons.[24] The electrons with energies above 50 eV are defined as the backscattered electrons. The energy distribution of the emitted electrons above 100 eV is independent of the primary electron energies.

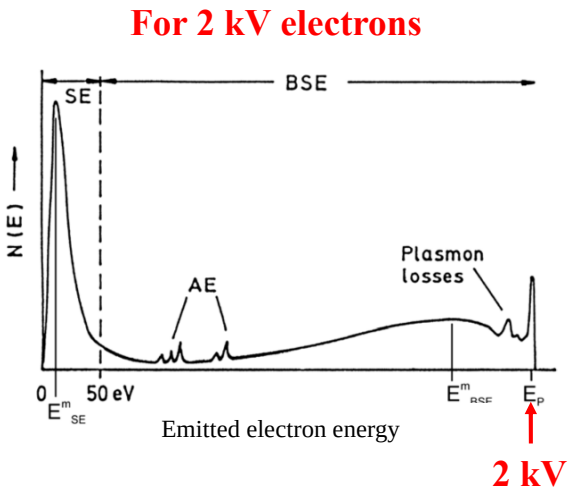

Figure 2.4. Typical energy distribution of emitted electrons for a material excited with 2 kV electron beam. (Adapted from Ref. 24)

2.2.3 Electron yields

The electron yield for a material is defined as the total number of emitted electrons per incident electron. The secondary and backscattered electron yields for most materials tend to be an intrinsic property of the material with a strong dependence on the accelerating voltage of the primary beam.

$$\text{Electron yield} = \frac{No.\ of\ emitted\ electrons}{No.\ of\ incident\ electrons}$$

The distribution of electron yields as a function of primary beam energy is shown in the Fig 2.5. The dependence of the SE yield with primary electron beam voltage is similar for most materials. The yield initially increases up to a maximum value, and then decreases with voltage.[24] This is related to the penetration depth of the primary electrons and to the escape depth of the secondary electrons. The penetration depth increases with beam voltage, and the total number of local secondary electrons increases with excitation volume. Below the voltage at maximum electron yield (V_m), the penetration depth is lower than the escape depth of secondary electrons, resulting in the secondary electrons escaping into vacuum. The penetration depth and escape depth are equal at V_m. Above V_m, the penetration depth is higher than the escape depth of the secondary electrons, resulting in many SEs losing energy before reaching the surface. Therefore, for voltages greater than V_m, the electron yields are lower despite the higher number of secondary electrons generated inside the material.

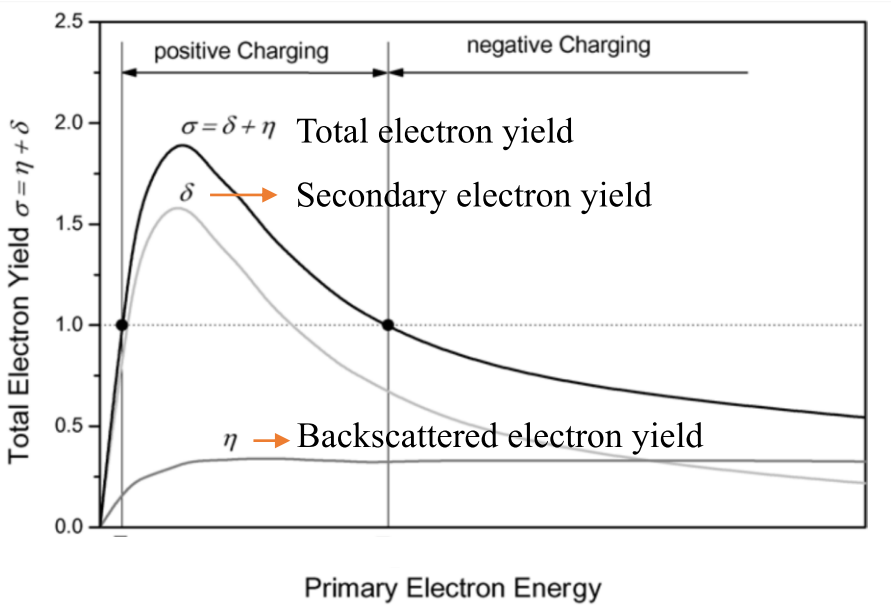

Figure 2.5 Typical electron yield distribution as a function of primary beam voltage. (Ref. 24)

When the electron yield is one, the total number of incident and emitted electrons are equal. This implies that the sample is not charging under the electron beam irradiation. When the electron yield is greater than one, number of emitted electrons are higher than the incident electrons, positively charging the sample. When the electron yield is lesser than one, number of emitted electrons are lesser than the incident electrons, negatively charging the sample. Figure 2.6 shows experimentally measured secondary, and backscattered electron yields for different elements. The BSE yields have little variation throughout the energy range for most materials with atomic number around 35.[25] The secondary electron has a strong and similar dependence on the energy of the primary electron beam.

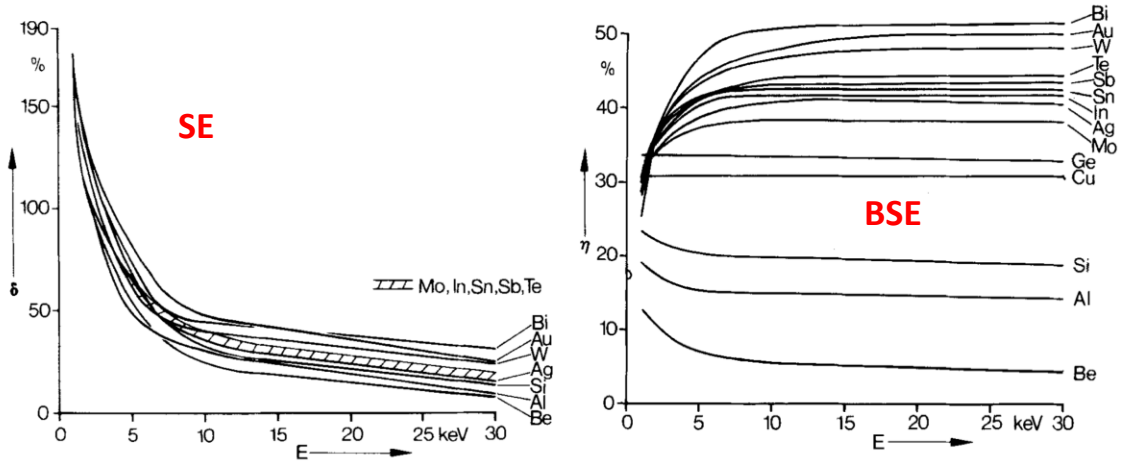

Figure 2.6. Experimentally measured secondary (δ) and backscattered electron yield (η) for various elements as function of the primary electron energy. (Adapted from Ref. 25)

Also, the absolute secondary electron yield of the material is higher for an insulator as compared to that of the metals.[24] This is due to the higher number of electron - electron scattering in metals as compared to insulators. This makes doped semiconductors, and negative electron affinity semiconductors most suitable for applications in electron emission devices.[23, 26]

2.2.4. Detection of secondary electrons

The kinetic energy of the SE's emitted from the specimen is in the range of 0 - 50 eV. In order to collect the low energy electrons, typically an SE detector of the Everhart-Thornley (E-T) type is employed. An E-T detector has a faraday cup which is biased at a positive voltage of about 300 V. This voltage is also called the extractor voltage, which can be typically adjusted from -50V to +300V.[27] The positive voltage on the faraday cup attracts the low energy electron cloud towards the detector. The SE's are then accelerated towards

a scintillator which is biased at a high positive voltage of 10 kV. The photons generated by the scintillator pass through a photomultiplier tube which are then recorded in raster format.

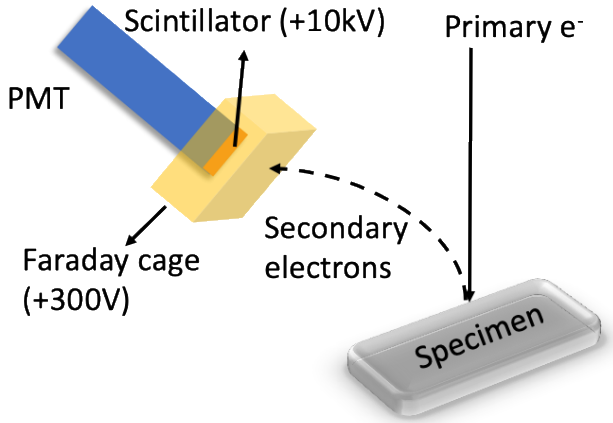

Figure 2.7 Schematic diagram of an Everhart-Thornley type SE detector.

The positive voltage on the faraday cup has a negligible effect on the high energy primary electrons impinging on the sample. But the image recorded has a contribution from various signals. That includes low energy backscattered electrons from the specimen, secondary electrons generated from the interaction of backscattered electrons and the chamber walls, and secondary electrons generated from the interaction of backscattered electrons and the objective pole piece. Above mentioned contributions need to be taken into account for the analysis of images recorded using SE detectors. E-T detectors can be employed in various geometries inside the SEM chamber. Side mounted E-T detector is most commonly found in SEMs. A through the lens detector (TLD) can also be found in newer SEMs which has the advantage of eliminating contribution from BSEs.[27] In TLD, the E-T detector is mounted above the objective pole piece where the SEs are captured by the magnetic field and are spiraled up to the detector.

2.3 Transmission electron microscopy

In a transmission electron microscope, the electron pass through the thin specimen (around 100 nm thick), which are then analyzed. The accelerating voltage of the electron beam in a TEM is in the range of 100 - 300 kV which is much higher than that of the SEM. Electrons interact with the specimen, undergo various scattering events which can be exploited to extract information about the specimen. In an SEM, only reflected electrons are analyzed, whereas in a TEM, transmitted electrons are analyzed. Given the lower scattering cross section of electrons in the TEM, bulk properties can be studied at a much higher resolution in the TEM.

2.3.1 Instrumentation

A TEM consists of an electron gun, condenser and objective lenses, projector lens, and detector. The schematic diagram of a TEM is shown in Fig. 2.8. The thermionic electron gun assembly in a TEM consists of a tip in a Wehnelt cathode, and an anode.

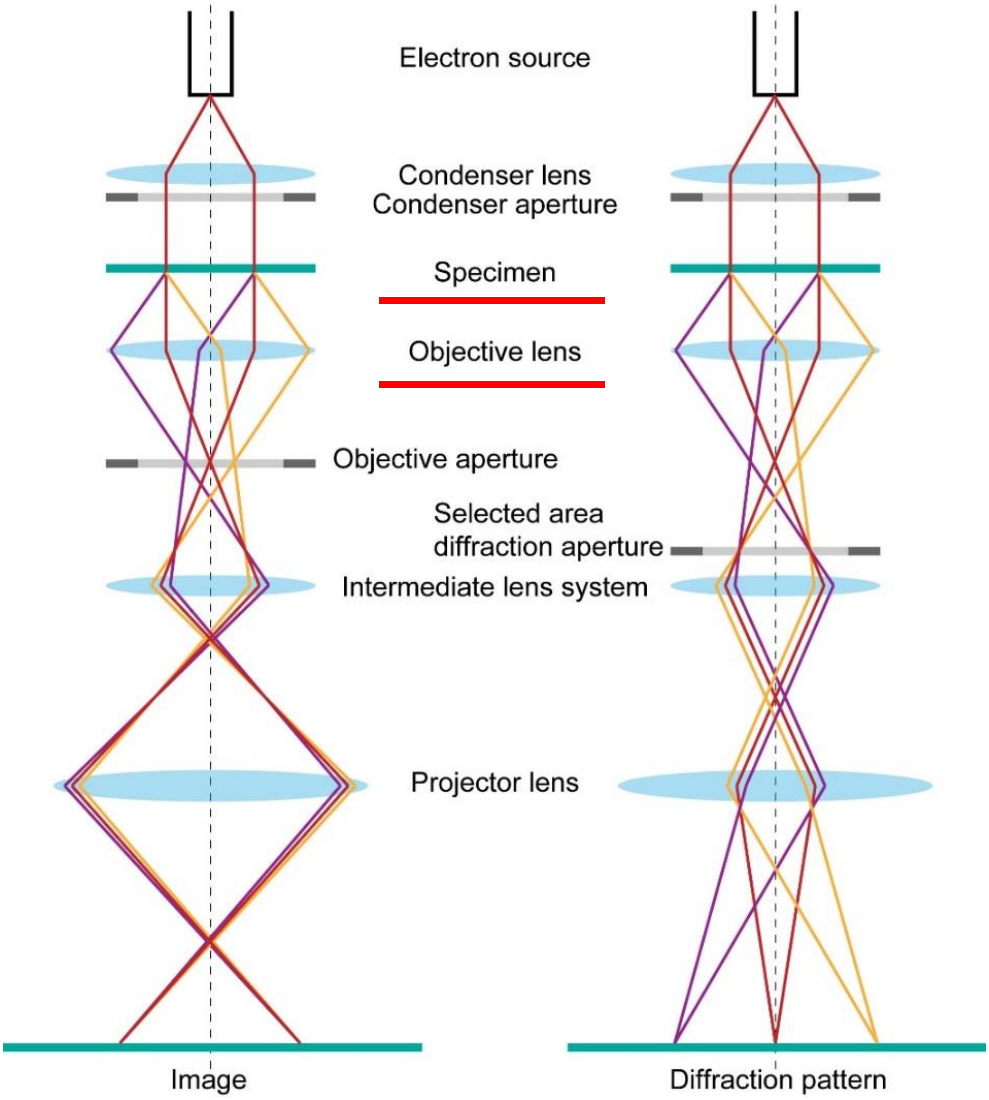

Figure 2.8. Schematic diagram of a TEM in imaging mode and diffraction mode.

In case of a field emission gun, there are two anodes. The bias on the tip extracts electrons and accelerates them between the cathode and anode. The conventional thermionic emission from a tungsten wire is limited in temporal coherence by an energy spread of the emitted electrons of the order of a few eV, and in spatial coherence by the gun brightness. Field-emission guns have a lower energy spread and higher gun brightness.

Table 2.3. Comparison of thermionic and a field emission electron gun.

Parameter	Thermionic	FEG
Cathode temperature	1400-2000 K	300 K or 1500 K
Diameter of source	10-20 μm	2-5 nm
Emission current density	20-50 A/cm^2	10^5-10^6 A/cm^2
Energy spread	1-2 eV	0.2-0.7 eV
E-field at cathode	10^4 V/cm	5 x 10^7 V/cm

Some of the key differences between a thermionic and a field emission gun are shown in Table. 2.3. The high coherence and the brightness of the FEG's are important for applications like electron holography.

The condenser lens in a TEM focuses the electron beam onto the specimen in such a way that there is enough intensity at different magnification ranges. There are typically two condenser lenses in a TEM. The advantage of the having two lenses is to increase the lifetime of the tip. When the first condenser is highly excited to get a small spot size of the beam, most of the electrons fall out of condenser aperture. In order to have enough brightness, having a second condenser lens can help focus the electrons back on to the sample. This eliminates the need for operating the gun at higher extraction voltage, eventually increasing the lifetime of the tip. The first condenser lens controls the spot size of the beam. Stronger the excitation of the first condenser lens, wider the beam spread, lesser the number of electrons passing through the C2 aperture, and smaller the spot size. The C2 lens excitation controls the underfocus or the overfocus mode of the TEM

illumination. Once the electron beam passes through the condenser lenses and the aperture, it passes through the objective lens assembly. The objective lens is the most important lens that determines the resolution and the quality of the image formed. It is the first lens in the TEM that forms an image of the specimen. The objective lens assembly typically consists of two pole pieces with the specimen sitting in between the pole pieces. To have minimal chromatic and spherical aberrations, the bore diameter of the objective lens has to be small with the distance between then smallest. Given most specimen holders are side mounted, there is a limitation on shortening the distance between the magnetic pole pieces. The electron interacts with the specimen, which then forms a diffraction pattern in the back focal plane of the objective lens. Depending on the mode of TEM, i.e. imaging or diffraction modes, the intermediate and the projector lenses project suitable image plane onto the detector. The magnification in a TEM is controlled by the excitation of the intermediate and the projector lenses.

2.3.2 Electron scattering in a TEM

When electrons pass through a specimen, there is coulomb interaction between the fast electrons and atomic nucleus which results in scattering. All the information recorded in a TEM is due to some form of electron scattering. The wave function of the exiting electrons is modified due to scattering inside a specimen. The two basic types of scattering in a TEM are elastic and inelastic. Elastic scattering refers to a change in direction of the electrons without change in their energy. In inelastic scattering, the electrons lose energy due to their interaction with the specimen. Elastic scattering can be coherent or incoherent with respect to the incident electron wave i.e. in or out of phase. Low angle elastically scattered electrons (<10 degrees) are usually coherent, while the higher angles can lead to

incoherent scattering. The higher angle scattering occurs due to the Rutherford scattering of the electrons, which can be used to form Z-contrast atomic resolution images. Inelastic collisions are usually confined to less than ~1^{o}. Inelastically scattered electrons can be analyzed by energy loss spectrometers, to extract chemical information of the specimen.[28]

The coherent electron wave interacts with the atomic scattering centers generating multiple secondary wavelets which interact with each other to generate zero order and higher order diffracted beams. Thus, coherent electron scattering form the basis for electron diffraction in a TEM. Diffraction patterns are the Fourier transforms of the real images, and consist of a periodic distribution of spots. Each spot corresponds to a set of diffracting planes in the crystalline specimen.

2.3.3 Bright field, dark field, and high-resolution imaging

In a conventional imaging mode, all the rays in the back focal plane of the objective lens are used to form the image. This includes all the diffracted beams and the transmitted beam, which produces less contrast. In diffraction contrast imaging, only certain beams can be used to form an image by having an aperture. Such imaging under the excitation of certain diffraction condition i.e. tilting the sample, can produce images with high contrast.[29] In bright-field imaging, an objective aperture is used to block out all the diffracted beams. Dark-field imaging refers to imaging using only a diffracted beam. In a bright-field image, the vacuum is bright and the specimen darker. By selecting suitable diffraction conditions, structural defects with Burgers vector corresponding to specific diffraction spots can be observed with high contrast. Aperture-less imaging has lower contrast due to the suppression of diffraction contrast.

High resolution TEM imaging involves imaging using as many as possible of the diffracted beams. This mode of imaging is also referred to as phase contrast microscopy. The electron beam interferes with itself after diffraction, where phase shifts are induced by the specimen. The interference of various diffracted beams creates lattice fringes that can represent the atomic arrangements in a crystal. The exit electron wave function encodes information about the phase shift induced by the specimen, which is greatly affected by the objective lens spherical aberrations. Thin samples are necessary for imaging in high resolution mode.

2.4 Electron holography

The term holography and hologram was first proposed by Dr. Dennis Gabor in 1948 as a way to surpass the effect of spherical aberrations in a TEM for obtaining the highest resolution possible.[30] The idea is to obtain both the phase and amplitude information of the specimen by interferometry. Typically, optical microscopy or low magnification TEM only captures the intensity variation across the specimen. This is equivalent to mass times thickness of specimen. Therefore, most information regarding the phase change is lost. In case of high-resolution electron microscopy, the resolution is limited by the spherical aberrations of the objective lens. The initial application of holography technique in electron microscopy was impeded by the unavailability of coherent electron sources. The first experiments of holography were carried out using mercury lamp with an aperture size of 0.3 mm to obtain a coherent point source. This is referred to as inline holography mode. The availability of field emission sources has led to the application of electron holography in an electron microscope due to the high coherence of the electron sources. Also, the availability of slow scan charge coupled device (CCD) that have linear response and high

detection quantum efficiency has increased the ease of recording and data analysis.[31] With newer microscopes being equipped with FEG sources and better detectors, many studies were performed using electron holography. Most of the applications involve study of electrostatic and magnetic fields at medium resolution. Given the electric and magnetic fields in a material are pure phase objects, holography can be an unique technique for their characterization. Although surface-based techniques like KPFM, STM can record phase changes, they are restricted to the surface properties. Electron holography has a unique advantage in measuring the bulk properties. There are more than 20 different types of configurations in which holography can be executed.[32]

2.4.1 Instrumentation

In this work off-axis electron holography mode is employed,[33,34] the schematic diagram of which is shown in the Fig. 2.9.

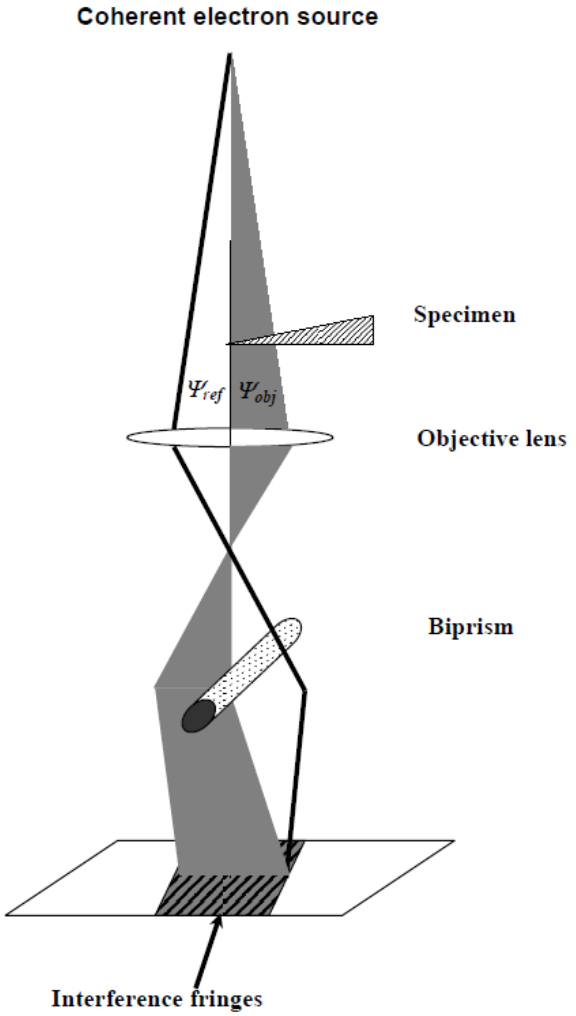

Figure 2.9. Schematic diagram of an off-axis electron holography setup. (Adapted from Ref. 34)

The idea is to interfere the electron waves passing through the vacuum and the specimen in order to obtain an interference pattern, which can then be unwrapped for phase and amplitude retrieval. The experimental arrangement consists of an FEG for coherence

of the electron source. The electrons pass through the condenser lens assembly, and the sample. The electron beam is split into two fronts with a part of it passing through the vacuum and the rest through the sample. The part of the electron wave passing through the vacuum is referred to as the reference wave (ψ_{ref}). The part of the electron wave passing through the specimen is referred to as the object wave (ψ_{obj}). The reference and the objective wave are made to interfere using a biprism. A biprism is typically a thin quartz wire ($d < 1$ μm) coated with gold. A positive voltage of 100 - 200 V is applied on the biprism to interfere the reference and the objective waves. All the holograms in this study are acquired in Lorentz mode. In Lorentz mode, the objective lens is switched off, and a weak mini-lens below specimen is activated. The advantages of using a Lorentz lens are the higher field of view, and weak magnetic field as compared to using the objective lens. Highest magnification achievable with Lorentz mode is in the range of 70,000X with a maximum field of view in the range of ~ 500 nm. This is very useful for the study of interfaces in thin films which are deep within the sample. The recording of interference patterns requires CCD detectors with good quantum efficiency. Care must take to allocate multiple pixels to each interference fringe in order to obtain meaningful data with a good signal to noise ratio. This translates to operating the detector with low binning values.

2.4.2 Interference and holographic fringe formation

The interference between the reference, and the object electron wave is achieved using an electrostatic biprism. Positive potential on the biprism wire deflects the electron beams so that they form interference fringes.[35] The geometric configuration at biprism is shown in the Fig. 2.10. The biprism wire is along the y-direction, the beam propagation

direction is along z-direction. The diameter (r) of the biprism is much smaller than its length (R), which typically is the size of the selective area aperture in which the biprism is housed.

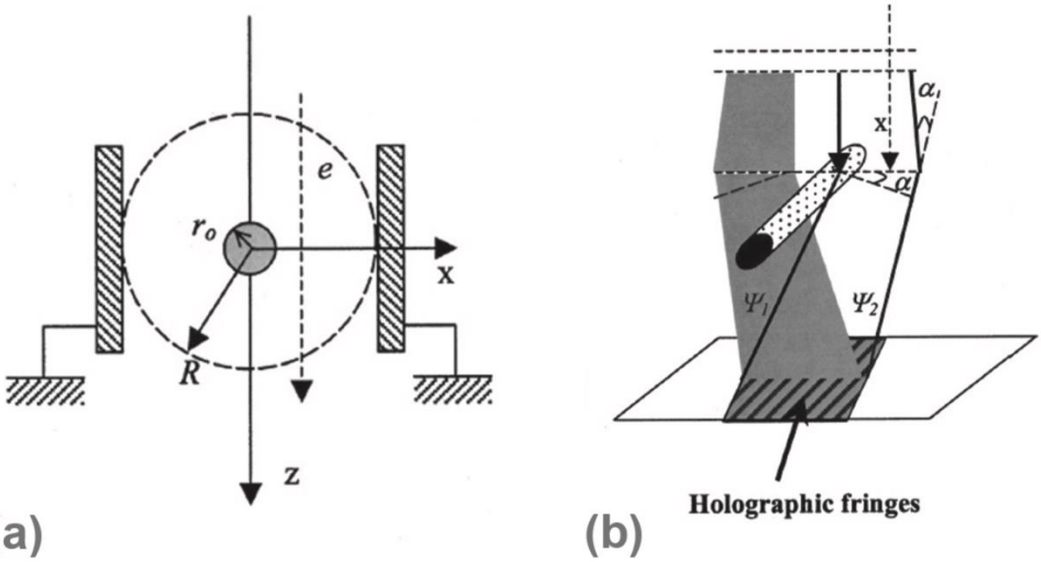

Figure 2.10 Geometric arrangement of a biprism in the microscope column. (Adapted from Ref. 34)

The biprism has a potential Φ_B, and the walls of aperture are grounded. The potential close to the wire can be approximated as

$$\phi(x,z) = \Phi_B \frac{\ln(\frac{\sqrt{x^2+z^2}}{R})}{\ln(r_0/R)}$$

Given the primary electron is much higher than the biprism voltage, the potential ϕ (x,z) near the biprism voltage does not affect the electron velocity (v), and only deflects the beam by angle α. The angle α can be derived to be

$$\alpha = \frac{e\,\Phi_B\,\pi}{m\,v^2\ln(^{r_0}/_R)}$$

The value of α is around 0.2 mrad for a microscope with r = 0.5μm, R = 1mm, Φ_B = 150V, and mv_o^2 = 300 keV. Figure 2.10(b) shows the deflection of beam, where the trajectory change of the electron due to the biprism field is x tan $\alpha \approx x\alpha$, which corresponds to a phase shift of $2\pi x\alpha/\lambda$ where λ is the wavelength of the electrons.

The wave functions ψ_1 and ψ_2 of the electron waves on either sides of the biprism before deflection can be represented by the plane wave functions as

$$\psi_1 = \psi_2 = A_r e^{i\mathbf{k}.\mathbf{r}} = A_r e^{i\theta_r}$$

Where A_r is the amplitude of the electron wave, **k** is the wave vector, **r** is the position vector. After being deflected by the biprism field, the wave functions can be represented by

$$\psi_{2,1} = A_r e^{i(\theta_r \pm 2\pi\alpha x/\lambda)}$$

In the above equation, **k.r** can be replaced with k.z as the k is close to the z-direction. Also, introducing the ψ_{ref} and ψ_{obj} for reference and object waves after deflection, we get

$$\psi_1 = \psi_{ref} = A_r e^{i(\theta_r - 2\pi\alpha x/\lambda)}$$

$$\psi_2 = \psi_{obj} = A_o e^{i(\theta_0 + 2\pi\alpha x/\lambda)}$$

In the above equation, θ_0 is the phase of the electron in the specimen. The interference between the above wave function can be written as

$$I = \left|\psi_{ref} + \psi_{obj}\right|^2 = \left|A_r e^{i(\theta_r - 2\pi\alpha x/\lambda)} + A_o e^{i(\theta_0 + 2\pi\alpha x/\lambda)}\right|^2$$

$$I = A_r^2 + A_0^2 + 2A_r A_o \cos(\theta_r - \theta_0 - 4\pi\alpha x/\lambda)$$

$$I = A_r^2 + A_0^2 + 2A_r A_o \cos(\Delta\theta - 4\pi\alpha x/\lambda)$$

where the term $A_r^2 + A_o^2$ is the background intensity, and the cosine part shows that the phase shift of the object wave relevant to the reference wave, $\Delta\theta$, is superimposed on the carrier fringes with a period of $\lambda/2\alpha$. The equation for interference indicates that electron holograms record both amplitude and the phase shifts of the equation wave.

Figure 2.11 shows interference pattern (holograms) formed by using a biprism for electron wave passing through the specimen and the vacuum. The fringe spacing for the reference hologram shown is ~ 1.7 nm. An average of 7 pixels on the charge coupled detector (CCD) are used to sample each fringe. This can be achieved by operating the CCD detector at lowest binning. The signal from the fringe pattern (Fig. 2.11(c)) is ~25%. It is important to adjust the microscope conditions to achieve highest signal to noise ratio for recording good quality electron holograms. Typically long exposure with low electron beam intensity is ideal for achieving high signal to noise ratio in a hologram. In reality, this is limited by the stability of the microscope. Thus, the signal obtained is a compromise between the electron beam intensity, and the exposure time. Optimal conditions must be found before recording holograms.

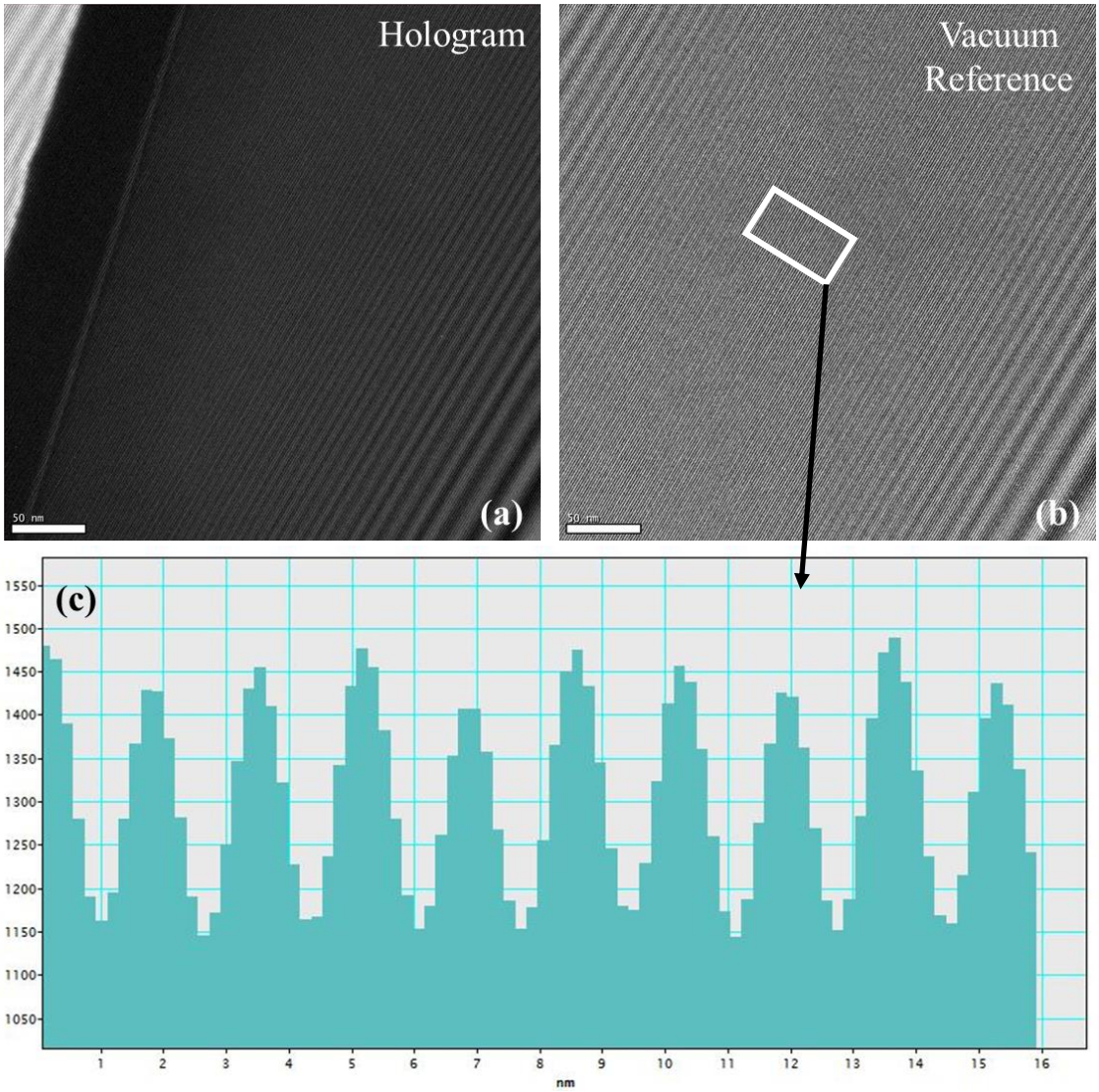

Figure 2.11 Electron wave interference pattern for the beam passing through (a) Specimen (b) vacuum. (c) Line profile of reference hologram showing a fringe spacing of ~ 1.7 nm.

2.4.3 Reconstruction of phase and amplitude

The reconstruction of phase and amplitude from the hologram is done by taking a Fourier transform (FT) of the hologram. Mathematically, the FT is represented as

$$FT(I) = \delta(u) \otimes \mathrm{FT}[A_r^2 + A_0^2]^2 + \delta(u - 2\,\alpha/\lambda) \otimes \mathrm{FT}[A_o A_r \exp(i\Delta\theta]$$

$$+ \delta(u + 2\,\alpha/\lambda) \otimes \mathrm{FT}[A_o A_r \exp(-i\Delta\theta]$$

Where u is the position vector, ⊗ represents convolution, and δ is the delta function.[36] After the Fourier transform, the hologram is divided into three parts. The first term is related to the background intensity of the hologram which corresponds to the central band in the FT of the hologram as shown in Fig. 2.12. The rest two term have identical information, and are complex conjugates of each other. They correspond to the sidebands in the Fig. 2.12.

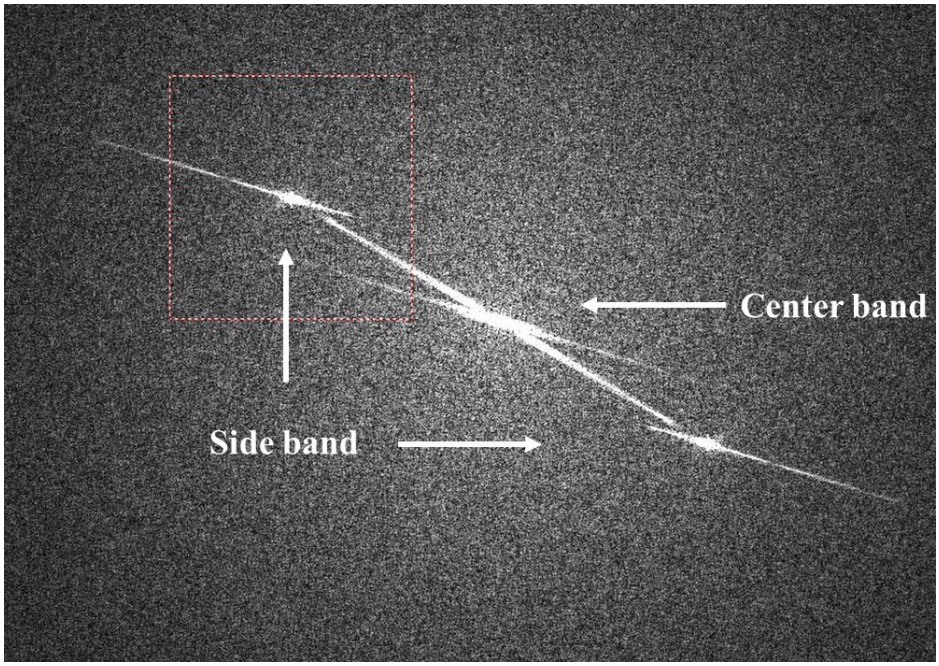

Figure 2.12. FFT of a hologram showing center and side bands.

The sideband contains information about the phase and amplitude of the object wave. Taking an inverse FT after shifting one of the sidebands to the center by $2\,\alpha/\lambda$, we obtain the phase and modulus given by,[37]

$$Phase\ (obj) = \Delta\theta$$

$$Mod(obj) = A_o A_r$$

A reference hologram is recorded under the same conditions with the sample out of field of view. The resulting phase and modulus of the complex image in vacuum are

$$Phase\ (ref) = 0$$

$$Mod(ref) = {A_r}^2$$

The phase shift of the object wave is given by the Phase (obj), and the amplitude of the object wave relative to the reference wave is obtained by dividing the Mod (obj) with Mod (ref) i.e. A_o/A_r. The sample thickness can be derived from the amplitude image using[37]

$$\frac{t}{\xi} = -2 \ln\left(\frac{Mod\ (obj)}{Mod\ (ref)}\right) = -2\ ln\left(\frac{A_o}{A_r}\right)$$

Where ξ is the inelastic mean free path (IMFP) of the electrons in the material. The inelastic mean free path depends on the energy of the electrons, and the intrinsic material properties. Monte Carlo simulations or electron energy loss spectroscopy can be used to find the IMFP of the electrons. This is an important parameter to deduce the thickness of the TEM sample from the amplitude image. There are simpler ways of finding the sample thickness, like, tilting the sample to look at the spread of a sharp interface, convergent beam electron diffraction (CBED) simulations to match the sample thickness, and looking at the TEM sample in an SEM to estimate the thickness of the sample. Also, the thickness mapping from the amplitude images is most suitable for structures with uniform composition. For hetero structures, the IMFP can be different for different layers, which makes it difficult to obtain reliable thickness variation information across the TEM specimen. In this thesis, the phase unwrapping is performed using a script developed by Prof. Martha R. McCartney of Arizona State University, which have been imported to the Digital Micrograph software. I am very thankful to her for training me on the use of scripts, and her guidance in analyzing the electron holograms.

2.4.4 Electrostatic potential from the phase

As the electron wave passes through the TEM specimen, the wave function is modified due to the interaction between the electrons and the specimen. This interaction can be used to study the magnetic and electrostatic fields present in the TEM specimen. The interaction between the electron wave and the specimen can be described by the Schrodinger equation,[38,39]

$$\left[\frac{1}{2m}(-ih\nabla + eA)^2 - eV\right]\psi = E\psi$$

Where m, e, h, ψ, A, V, and E are the electron mass, electron charge, Planck's constant, electron wave function, vector potential of magnetic field, scalar electrostatic field, and electron energy, respectively. Assuming the electron wave function at any point (x,y) to be ψ(x,y) after passing through the specimen, it has the form of

$$\psi(x,y) = A(x,y)e^{i\theta(x,y)}$$

Where $\theta(x,y)$ is phase of the electron wave, and the A(x,y) is the amplitude of the electron wave corresponding to that point. Applying Wentzel, Kramer, Brillouin (WKB) approximation to solve the Schrodinger equation, the phase change of the object wave relative to the reference electron wave is,[38,39]

$$\Delta\theta(x,y) = \frac{\pi}{\lambda E}\int V(x,y,z)dz \; - \; \frac{2\pi e}{h}\iint B_n(x,y)dxdz$$

Integration in the above equation is performed along the z-direction, parallel to the electron beam propagation. λ is the wavelength of the electrons, V(x,y,z) is the electrostatic potential, B_n(x,y) is the component of the magnetic field perpendicular to the beam

direction. E is a constant which depends on the kinetic energy of the electrons, which is given by

$$E = \frac{U}{2}\frac{E_k + 2E_o}{E_k + E_o}$$

Where U is the accelerating voltage of the electron beam, and E_k, E_o are the kinetic energy, and the rest mass energy of electrons. If the magnetic field in the specimen is zero, and the electrostatic potential in the electron beam direction is constant, the phase change in the TEM specimen can be related to the electrostatic potential in the x-y plane as[33]

$$\Delta\theta(x,y) = C_e V(x,y)t$$

$$C_e = \frac{2\pi}{\lambda U}\frac{E_o + E_k}{2E_o + E_k}$$

Where C_e is the interaction constant. C_e depends on the energy of electron beam, λ is the wavelength of the electrons for specific accelerating voltages. For electron beam at an accelerating voltage of 300 kV, the value of C_e is 0.00653 $Rad/(V.nm)$.

Thus the projected electrostatic potential can provide information about the charge distribution across the interfaces. The electron holograms need to be acquired in weak diffracting conditions to avoid any kind of diffraction artefacts in the data. Typically, the interfaces of interest are kept edge on. For a simple *p-n* junction, the potential profile obtained from the electron holography can provide information about the depletion widths near the junction. In order to convert the potential profiles (V) into energy profiles (E), which is commonly seen when discussing the band diagram of the semiconductors, the following equation can be used

$$E = - e V$$

In order to obtain the charge distribution, Poisson's equation can be used to derive it from the potential profiles. Typically, the data obtained from the electron holograms is noisy, which cannot be directly differentiated for charge distribution. The potential profile needs to be fit with smooth lines and curves before using the following equation to determine the Coulomb charge density.

$$\rho = -\varepsilon_0 \nabla^2 V$$

Where ρ is the charge density, and V is the potential profile. A simple comparison of band structures and potential profiles may not be ideal. At high electron energies, the crystal potential is essentially purely electrostatic and classical in origin and independent of the energy of the projectile electrons. In EH, we measure only the pure electrostatic potential component without sensing the exchange correlation part, which leads to a big difference between the potential profile obtained from EH and the potential discussed in the band structures. So, a simplistic comparison is not encouraged. The most reliable information from the holograms can be the charge distribution across the thin layers.

2.4.5. Sample preparation for electron holography

The most critical step for obtaining good holograms is the preparation of a good TEM sample. In this work, cross section TEM samples are prepared by wedge polishing on an allied multi-prep machine. If the TEM specimen surfaces are prepared poorly, the phase obtained is very noisy, and can lead to lot of artefacts. In order to avoid that, great care must be taken during the sample preparation process. In this section, some of the best practices that have yielded good samples during the course of this work are listed. These

can serve as guidelines, and the necessary steps may vary for different material system. Attention to little details is important during the process of sample preparation.

Two main requirements for a good holographic analysis are (a) the thickness of the TEM specimen to be around ~200 nm, and (b) large vacuum area near the sample edge. Wedge polishing has the advantage over dimple polishing in terms of the vacuum area obtainable near the sample edge. Also, the sample can be polished to electron transparency in some cases thus eliminating the need for argon ion milling using. First step in the sample preparation is to cut small pieces of about 1.5 x 2.5 mm, and stick the film faces together with m-bond as shown in the Fig. 2.13.

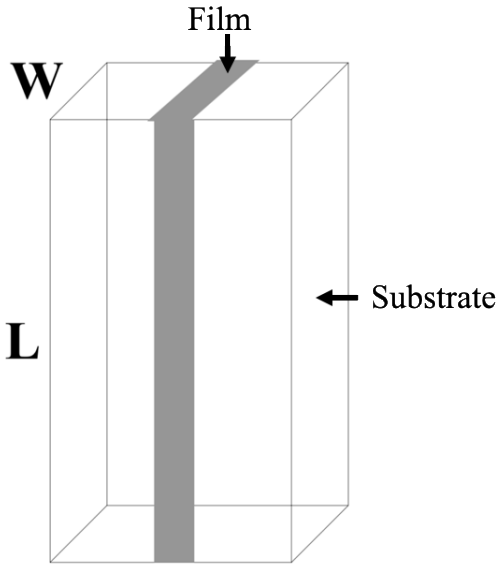

Figure 2.13. Bonding of 1.5 x 2.5 mm wafer pieces for TEM specimen preparation.

Most of m-bond must be squeezed out while bonding the pieces together. This greatly effects the polishing quality. Presence of excess glue can chip off and scratch the sample during the polishing process. Also, sample cannot be thinned to the best possible thickness with the presence of excess glue.

Table 2.4. Polishing parameters for wedge polishing TEM specimen.

Lapping film	Rotation speed	Max. final thickness
30 μm	80	120 μm
9 μm	70	50 μm
6 μm	60	30 μm
3 μm	50	10 μm
1 μm	40	--
0.5 μm	30	--
0.1 μm	20	--

The bonded specimen is then mounted onto a Pyrex polishing paddle using mounting wax. Little amounts of good quality wax are important for obtaining best samples. The next step is to grind the bonded sample suing diamond lapping films. The table 2.4 lists the rotation speeds, and final thicknesses for lapping films of various roughness.

For second side polish, use as little glue as possible and squeeze out as much of it possible from underneath the sample. If extra wax or air bubbles are present, there is a high chance that sample breaks before being thinned down to electron transparency. This would demand longer ion milling times which is undesirable. First side of the TEM specimen needs to be about 700 μm by the end of polishing. Starting with 3 μm lapping film, a tissue paper should be used on the lapping film to collect the fine ground particles to avoid unwanted scratches on the TEM specimen. Also, it is a good idea to try various loads to obtain best surface finish. RMS thicknesses of about 1 nm is routinely achievable for polished surfaces under best conditions. During the second side polish, a wedge angle of ~1-2^0 is set near the

sample holder, once the sample is about 120 μm. The polishing direction for the second side can be from thicker end to the thinner end of the sample. This greatly reduces particles chipping off from the thinner end breaking the sample. This is especially important when the sample is thinner than 10 μm. Once the thinner end of the sample is less than 10 μm, it is hard to measure the thickness with an optical microscope. For GaN, Newton fringes can be observed when the sample gets thinner. Polish using 1 μm paper to observe the Newton fringes, and then further thin it down with 0.5 μm and 0.1 μm lapping films till edge of the specimen starts chipping off. At this stage, it is highly likely that the specimen thickness is close to 1μm.

Finally the Pyrex stage is left a clean beaker filled with acetone for the wax to be dissolved. Once the sample falls off the Pyrex stage, break the two halves that are glued together by applying a little pressure with sharp tweezers on the glue line near thicker end of the wedge. Stick each of the pieces onto a half-cut molybdenum grid as shown in the Fig. 2.14 with as little m-bond as possible. Squeeze out any extra glue in order to avoid redepositing m-bond onto the sample during milling. Also, this may play a role in sample sitting at right height inside the ion milling chamber.

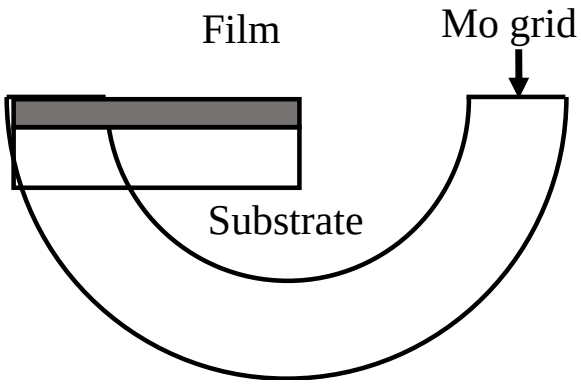

Figure 2.14. Schematic diagram of a sample on a Molybdenum (Mo) grid.

The choice of Molybdenum over copper grids can be greatly beneficial for reduced grid material re-deposition on the TEM specimen during ion milling. The geometry of the sample arrangement on the Mo grid is very important for the reduction of back sputtered material onto the sample edge. This increases the field of view during holographic analysis. For ion milling, the sample is loaded on the PIPS loader with the sample side down, and the grid facing upward. This ensure the thin region of the sample is in eucentric focus of the argon ion guns in the PIPS machine. In this specific arrangement the TEM specimen is milled from the backside using single mode. Low temperature milling may be desirable in order keep the thin region cool. The sample if polished well should require about few minutes of ion milling at ~3 kV. The sample can then be cleaned with lower voltages from 1 kV down to 0.1 kV. Typically, few minutes at each voltage can result in good sample surface. If copper sputtering is seen on the sample due to the use of copper grids, the TEM specimen can be treated with dilute HNO_3 for few minutes to remove the copper particles. The sample must then be treated with DI water for removing residual HNO_3. If there is large amounts of amorphization due to ion milling, there are multiple ways to rectify it. Use a dilute etchant to treat the TEM specimen. For GaN TEM specimen, treatment with dilute KOH for 1-2 minutes can remove surface amorphization. Careful monitoring is necessary in order to not etch more than required amounts. The sample must then be treated with DI water for removing residual etchant. Other non-chemical way to remove the surface amorphization is to plasma trim the sample. This is different from the regular plasma cleaning. Plasma trimming is typically used for FIB samples to clean the surfaces. In plasma trimming, the sample is vertically held at the top of the chamber, where the film side is facing the ground on an aluminum chuck painted with colloidal graphite solution.

The argon ion plasma is accelerated from the bottom of the chamber to the sample in order to etch away the surfaces of the TEM specimen at a controlled low etching rates. This is the best way to achieve excellent surfaces for holographic analysis. More information about the plasma trimming technique can be found on the South Bay Technologies website. Finally, silver paste is used to create an electrical contact from the wedge polished sample to the molybdenum grid in order to avoid sample charging inside the TEM column during the holographic analysis.

2.5 Secondary ion mass spectroscopy (SIMS)

When a surface is bombarded with high energy primary ions, various atoms and molecular species are sputtered from the surface. A portion of these sputtered ions can be extracted with an electric field. The extracted sputtered species can be mass separated and analyzed to determine the chemical composition of the sample surface. This phenomenon forms the basis of the secondary ion mass spectroscopy (SIMS). The incident primary ions are usually oxygen or cesium as they enhance the sputtered electronegative or electropositive secondary ion yields.[40–42]

2.5.1 Introduction to SIMS

SIMS has become the main analysis tool for detecting impurities with concentrations in the range of 10^{12} - 10^{20} cm^{-3} in thin film semiconductors. This kind of sensitivity allows to determine the dopant concentrations and unwanted impurities in the semiconductor systems. Typical SIMS instrument consists of primary ion sources, mass analyzers and detectors. Figure 2.15 shows schematic diagram of a Cameca IMS 6f SIMS instrument. It

consists of two primary ion sources of O_2^+, and Cs^+. Typical accelerating voltages of these source range from 5 kV to 15 kV depending on the application and the requirement of the analyses. When the sample is bombarded with these high energy primary ions, charged or neutral ions and molecular species are sputtered from the sample surface. An electric field is used to extract these ions, which then pass through a mass analyzer for the analyses. In this study we use SIMS for the depth profiling of the impurities. This is done by monitoring the intensity of select secondary ions as a function of sputter time. The sputter time can then be converted into depth.

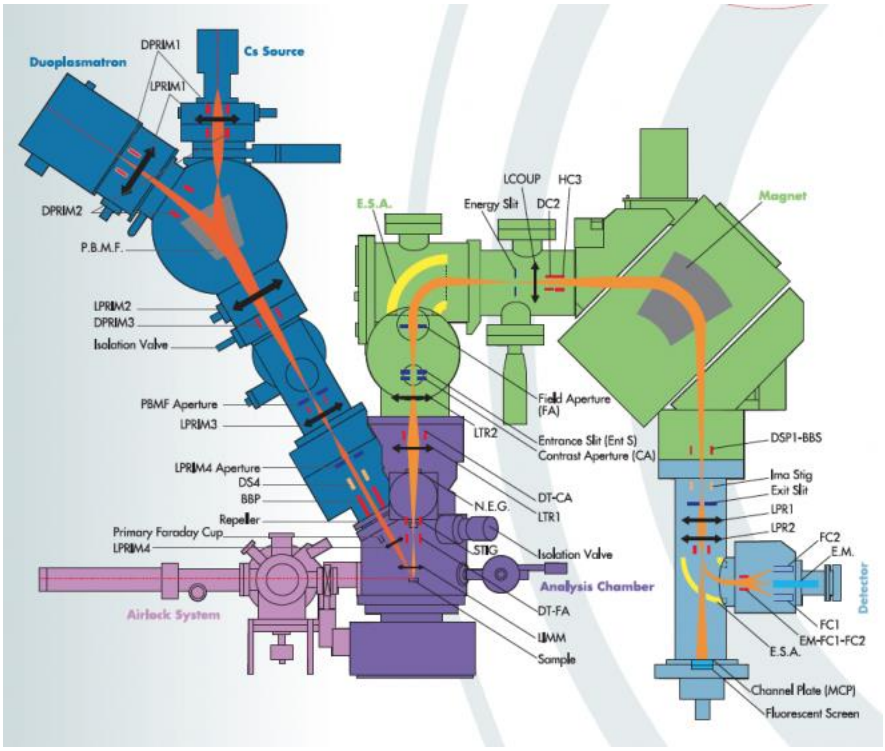

Figure 2.15. Schematic diagram of the magnetic sector Cameca IMS 6f SIMS instrument.

The magnetic sector SIMS instrument has high energy ion sources, which pass through a series of lenses for focusing the beam, and to raster the beam on the sample. The sample is typically held at a voltage of +/- 5 kV depending of the type of secondary ions being analyzed. For positive secondary ions, the sample is held at a positive voltage and

vice versa. The bias on the sample ensures the secondary ions are ejected from the surface without being attracted by the sample surface itself. The beam raster size is typically 250 x 250 μm^2. The beam raster enhances the surface smoothness as the crater is being dug for the depth profiling analysis. The signal is collected from a 60 x 60 μm^2 to eliminate the effects from the sloping sidewalls as a result of the beam raster. The extraction lens in a magnetic sector SIMS is placed at ~4.5 mm from the sample, which is grounded. The charged sputtered secondary ions are extracted by electric field between the sample and the extraction lens.

When the primary ions bombard the sample surface, they transfer kinetic energy to the sample via nuclear collisions. A target atom is set in motion by such collisions, and this displaced atom may transfer a part of this energy to another target atom.[43] This sets in a collision cascade in the sample. Figure 2.16 illustrates the formation of a collision cascade during the interaction of primary ions with the sample.

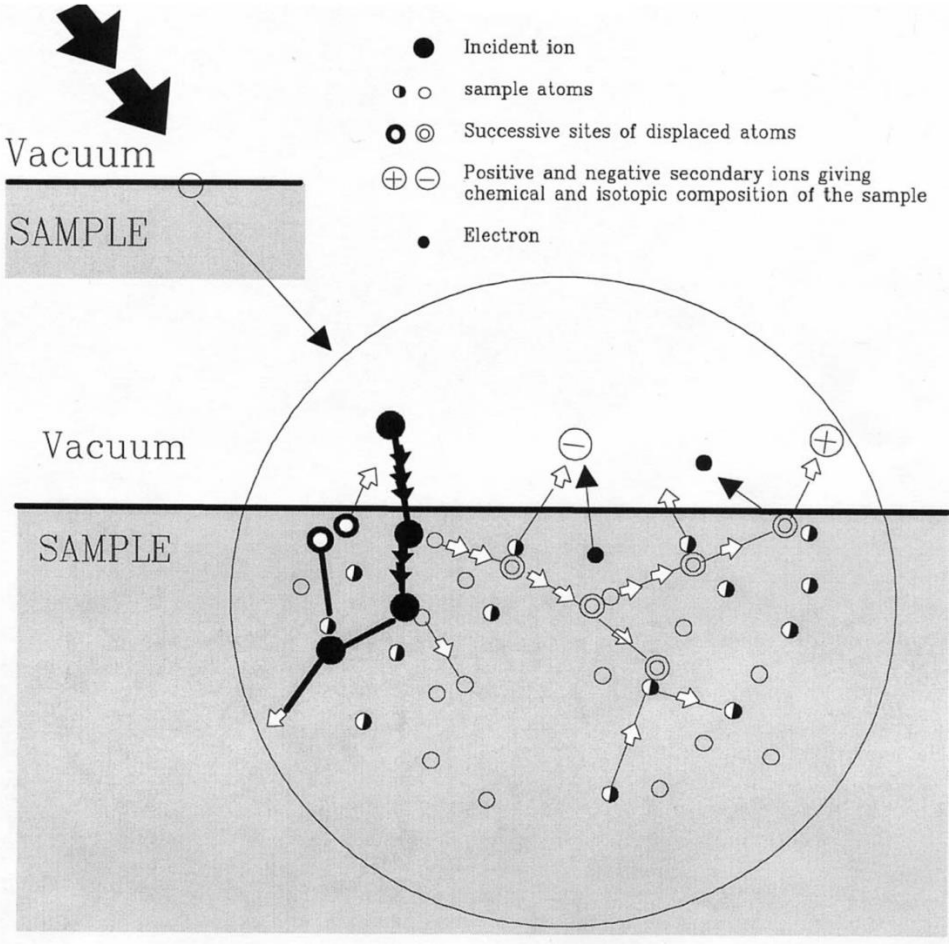

Figure 2.16. Collision cascade set in by the interaction of primary ions with the sample. (Adapted from Cameca IMS 6f user manual).

During the collision, some of the target atoms in the near surface gain sufficient momentum and energy to overcome the surface potential barrier and escape the sample. Most of the sputtered species leave the surface with low energy (mainly in the 0~100 eV range) with a peak in the energy distribution at less than 10 eV. A small fraction of the emitted particles leaves the sample surface in the ionized state, either positive or negative. Also, they combine to form some charged molecular species. These ions and molecular species are then collected by the mass spectrometer and mass analyzed.

2.5.2 Magnetic sector mass analyzer

Magnetic sector analyzers are typically used in a dynamic mode SIMS, where the beam is scanned in a raster pattern on the sample. The sample is continuously eroded as the secondary ions of interest are monitored in a cyclical manner. This section describes the process of analyzing the intensity of secondary ions using a magnetic sector analyzer.

In a typical magnetic sector SIMS, e.g. CAMECA IMS 6F, the sample is maintained at a potential (adjustable from -5 to +5 kV) and the immersion cover plate is grounded which is 4.5 mm above the sample. This setting results in a strong extraction field of secondary ions. The extracted secondary ions leaving the sample surface have kinetic energy given by

$$\frac{1}{2}\, mV^2 = \; qV$$

Where m is the mass of the ion, v is its velocity, q is the charge of the ion and V is the secondary ion acceleration voltage. The ions pass through a magnetic sector flight tube in which the magnetic field (B) is applied perpendicular to the direction of ion motion. The ions are deflected by the magnetic field. Only ions of mass-to-charge ratio that have equal centrifugal and centripetal forces pass through the flight tube as described by

$$\frac{mv^2}{r} = qvB$$

Where r is radius of curvature of the ion path. From the above equations, the mass-to-charge ratio as a function of magnetic field and secondary ion acceleration voltage is obtained as shown in

$$\frac{m}{q} = \frac{B^2 r^2}{2V}$$

By adjusting the strength of the magnetic field, the magnetic sector analyzer will separate the secondary ions of equal energy according to their mass to charge ratio. The resolution of the selecting the species with certain mass to charge ratio is limited by the uniformity of the energy of the secondary ions. The secondary ion species do not have the same velocity. This is analogous to chromatic aberrations in optical microscopy. The secondary ions of certain species have energy distribution within hundreds of eVs with a peak around ~10 eV. In order to focus the secondary ions according to their kinetic energy, an electrostatic analyzer (ESA) is utilized where an electric is applied perpendicular to the ion motion.[44] This acts as a focusing lens for ions with specific energy range. An energy slit can be used to further narrow down the energy window. Figure 2.17 shows a schematic diagram of a magnetic sector double focusing mass analyzers. Once secondary ions of a particular kinetic energy are selected, they can be analyzed with a magnetic sector according to their momentum which is equivalent to selecting mass to charge ratio of mono-energetic secondary ions.

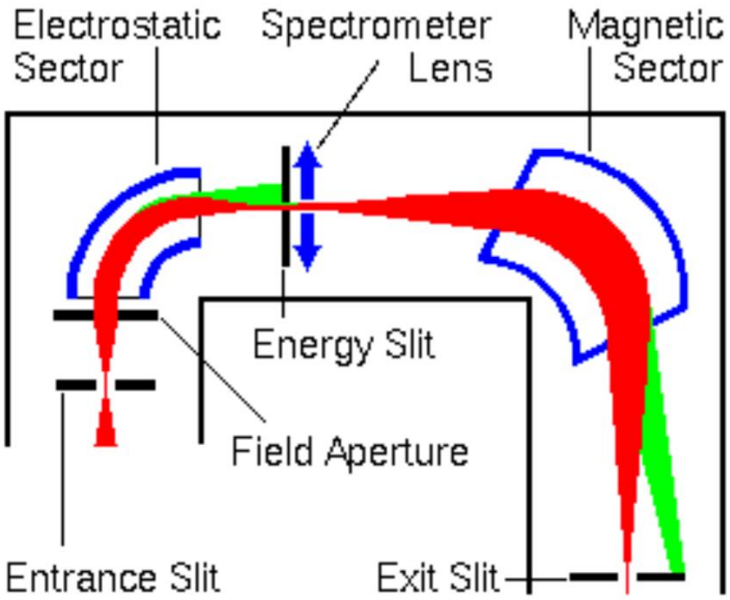

Figure 2.17. Schematic diagram of magnetic sector double focusing mass analyzers, including electrostatic analyzer (ESA) and magnetic sector (MS) (Adapted from Ref. 44).

Typically, ESA is kept at a constant potential, and the magnetic field is varied for mass to charge ratio selection of secondary ions. A magnetic field scan can be used to cover a wide range of mass-to-charge ratios with constant ion transmission, i.e. ion transmission is essentially independent of the mass-to-charge ratio. The disadvantage of a magnetic field scan is that the magnetic field is subject to hysteresis and the mass switching speed is limited. The resolving power of the mass spectrometer depends on the size of the energy slits widths. Smaller slit widths can result in higher mass resolution but secondary ion intensities will be lower.

Once the ions pass through the magnetic sectors, the ion counts are measured either by an electron multiplier (EM) or a Faraday cup (FC). The electron multiplier is used to measure secondary ion count rates from 10^{-1} to 10^{6} counts/second, while the Faraday cup is used to measure count rates in the range of 10^{5} to 10^{9} counts/second.[44] The combination

of these two detectors provides a very high dynamic range for the secondary ion intensity measurement.

Given that the sample is bombarded with charged species and the emitted secondary ions are charged, sample charging is an issue during the analysis of semiconductor and insulators. Some of the common strategies for avoiding the charging of samples during the depth profiling are gold coating, and using electron flux for charge compensation. This is very important in order to avoid damage, and measurement artefacts due to sample charging.

2.5.3. Depth resolution and sensitivity

Depth resolution and sensitivity are the two important factors for the depth profiling analysis of impurities in thin film semiconductors. Depth resolution is the ability detect impurities as they are distributed in the layers. Figure 2.18 shows snapshots of simulation intermixing in the top few monolayers under the impact of high energy primary ions.

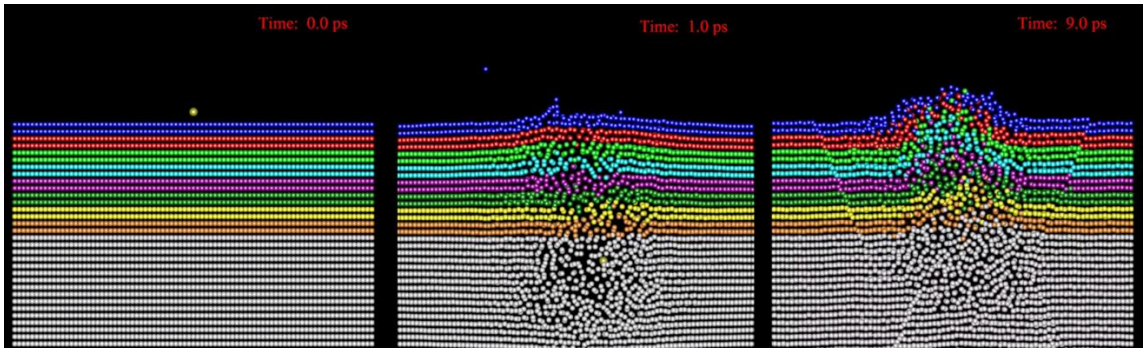

Figure 2.18. Schematic diagram of evolution of intermixing in a target matrix under the impact of high energy primary beam. Layers are color coded in order to observe the effect of intermixing (Adapted from Prof. Barbara J. Garrison's group website – Penn State).

As the primary beam interacts with the target matrix, there are ion and molecular species from the top layer being knocked out. At the same time, there is intermixing of the top few layers. As the crater is dug deeper, the surface roughness at the bottom of the crater, and the intermixing of the layers increases. Also, the beam raster results in slanted crater sidewalls. Thus the depth resolution depends on the intermixing due to the primary beam impact, surface roughness of the crater bottom, and the ability to reject the secondary ions originating from the sidewalls of the crater.[45] Figure 2.19 shows a monolayer of red atoms being smeared as the SIMS analysis is performed. The material is being dug from left to right. With the progression of the crater, the atoms in the monolayer as smeared out and their respective secondary ions are read over a depth range.

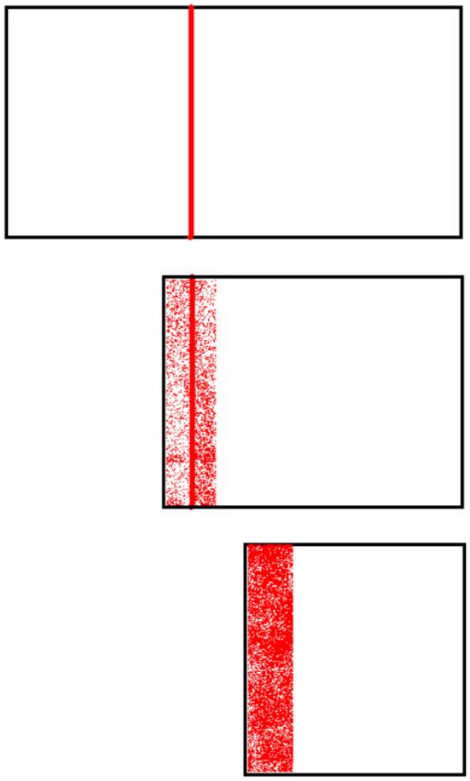

Figure 2.19. Schematic diagram of a monolayer (Red layer) being smeared as the crater is being dug from left to right. (Courtesy of Dr. Peter Williams from ASU).

The depth resolution is thus dependent on the energy of the primary beam. Lower the beam energy, lower the range of the ions in the matrix and higher the depth resolution. Also, the depth resolution depends on the choice of primary ion, angle of incidence and the species of secondary ion being monitored. Crater roughness can also affect the depth resolution due to non-uniform erosion of the sample surface which exposes various depths to the analyzing ion beam. Figure 2.20 shows true dopant concentration vs. measured concentration the measured concentration which is due to all the above-mentioned parameters. The broadening at the interface can get worse with depth due to rougher crater surface with increasing crater depth. Typically, the cesium beam provides with better depth resolution as compared to oxygen beam with same primary energy given the smaller range of cesium ions in the GaN lattice.

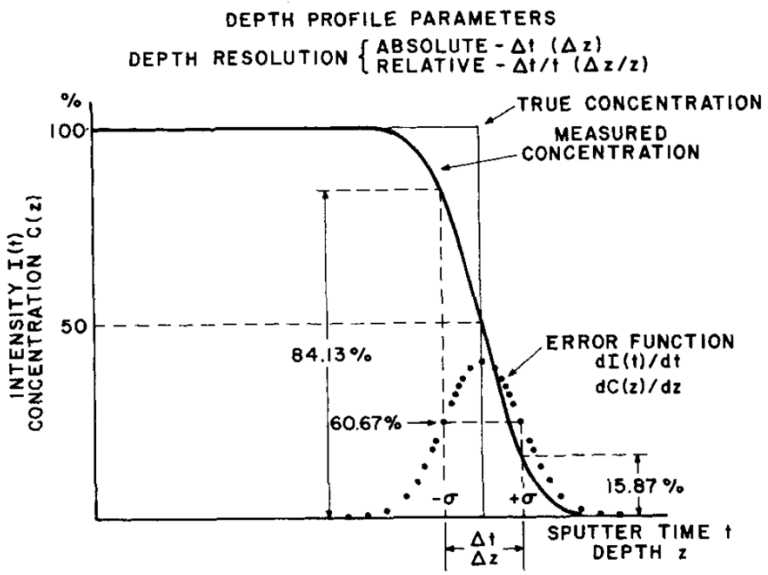

Figure 2.20. True dopant concentration vs. measured dopant concentration in SIMS (Adapted from Ref. 45).

Sensitivity is the ability to detect the low levels of secondary ions. Typically, sensitivity of different impurities depends on the beam current, secondary ion species. Higher the beam density, higher the secondary electron counts thus increasing the detection sensitivity of impurity elements. Also, certain species have higher secondary ion yields as compared to the others. Thus, the choice of secondary ion species can affect the sensitivity.

The requirements for depth resolution, and sensitivity are conflicting in nature. Lower beam energies result in better depth resolution but the lower currents obtainable with lower beam energies yield lower secondary ion counts. This leads to lowered sensitivity. Thus, there is always a compromise between the depth resolution and sensitivity of the impurity elements during SIMS analysis. Also, the focusing of primary beam at lower energies is much poorer. The spot size of the beam affects the quality of the data.

2.5.4. Quantitative impurity analysis in GaN using O_2^+ and Cs^+ as primary ions

Use of oxygen and cesium as the primary ion sources has their own advantages for analysis of impurities in GaN. The main impurities of interest in GaN are Mg, Si, O and C. Mg, Si are the primary *p*-type, and *n*-type dopants in GaN. Oxygen and carbon are impurities in GaN which occur due to the contaminated gas sources and chamber wall impurities.

The oxygen beam increases the positive secondary ion yield whereas cesium increases the negative secondary ion yields in GaN. In order to extract positive and secondary ions efficiently, the sample is biased at a voltage of +5 kV and -5 kV. The accelerating voltage of the oxygen source during SIMS analysis for GaN is typically 12.5

kV, whereas for cesium beam, it is 10 kV. The net impact energy of the primary ions for the case of O_2^+ and Cs^+ beams are 7.5 kV and 15 kV respectively.

The secondary ion count rates for Ga^+, N^+, Mg^+, Si^+ are high when GaN matrix is bombarded with O_2^+ beam. This analysis can be a great method analyze Mg and Si depth profiles simultaneously. Simultaneous analysis of Mg and Si is of high importance in this work. The secondary ion count rates for C is low with oxygen beam. Also, O cannot be analyzed with oxygen beam due to high levels of interference from the primary beam. The table 2.5 shows the ionic and molecular species monitored with O_2^+ and Cs^+ beams for various impurities.[46–48]

Table 2.5. Secondary ion and molecular species monitored for identification of impurities in GaN matrix with O_2^+ and Cs^+ beams.

Species	Oxygen beam	Cesium beam
Ga	Ga^+	GaN^-
N	N^+	GaN^-
Mg	Mg^+	$GaNMg^-$ MgN^- $CsMg^-$
Si	Si^+	$Si(28 \text{ or } 30)N^-$
O	----------	O^-
C	Hard to detect	CN^-

Cesium can be very useful for the detection of O^- and CN^- species as their secondary ion count rates are very high. The secondary ion species have different yields. While analyzing the SIMS data, interference from species with same mass to charge ratio has to be kept in mind. In order to avoid these effects, the choice of species to be monitored is

paramount. Although, the mass to charge ratios for different species are similar, there is always a slight variation in the mass for each species which can be tackled by choosing high mass resolving power or narrow energy slit widths. This reduces the overall count rates of the secondary ions.

Figure 2.21 shows the raw SIMS data obtained from a GaN matrix using O_2^+ as the primary beam. The data plotted is SIMS counts versus the sputter time. The sputter time can be converted to depth by measuring the SIMS crater depth with a profilometer.

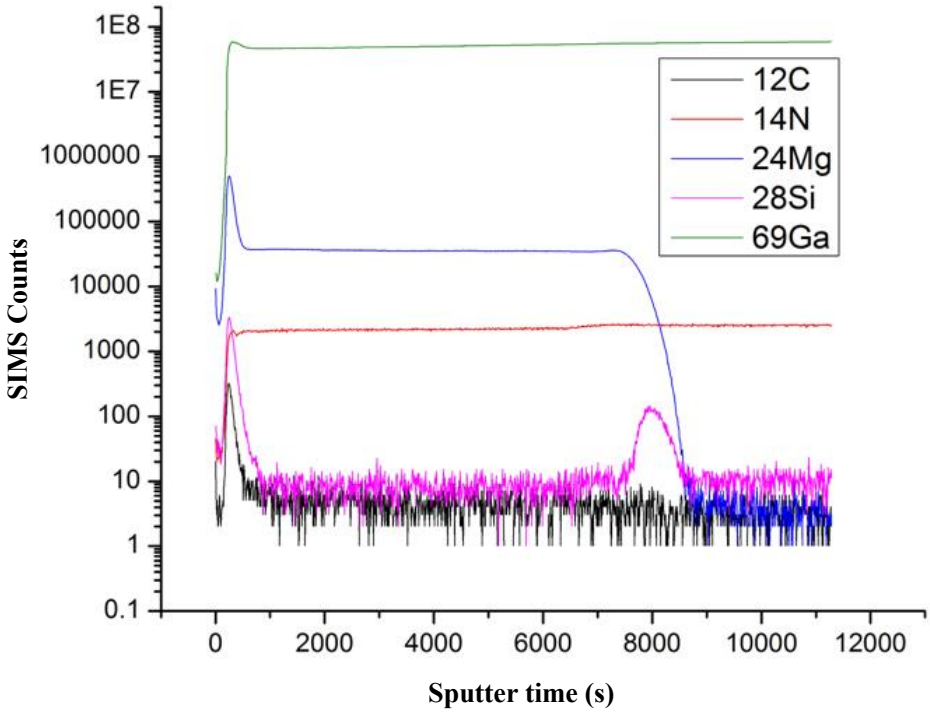

Figure 2.21. As obtained SIMS data obtained from a GaN matrix for different species using O_2^+ as primary beam.

In order to convert SIMS counts of each species into concentration, a widely used method is identifying the relative sensitivity factor (RSF) for individual secondary ion.[40] RSF is used to quantify impurity concentration below 1% of the matrix elements.

$$\frac{I_m}{C_m} = RSF \times \frac{I_i}{C_i}$$

Where I_m and C_m are secondary ion intensity and matrix element concentration, I_i and C_i are secondary ion intensity and impurity element concentration. The RSF can be found using standard implanted samples using the equation[40]

$$RSF = \frac{\emptyset\, I_m t}{d \int I_i}$$

Where ϕ is the implantation dose, I_m is matrix element intensity, t is the total sputter time, d is the crater depth and $\int I_i$ is the integration of the secondary ion counts over the depth profile. Various studies show that the RSF values can have a variation of 50% within the same instrument group. Depending on the analysis conditions, 1-10% accuracy can be obtained under similar analysis conditions.[49] Also, analyzing the samples with known concentration of impurities in the same measurement run can be useful for quantification purposes.

The primary current of the beam can deviate with time during the analysis period as shown in the fig 2.22. The Ga signal shows about ~13% increase in counts through the measurement run. This has to be taken into account during quantification. The reason for sudden shift in the nitrogen sputter yield for differently doped GaN is unclear. The relative secondary ion yields of N, N^+, N^- etc. could be changing with dopant types.

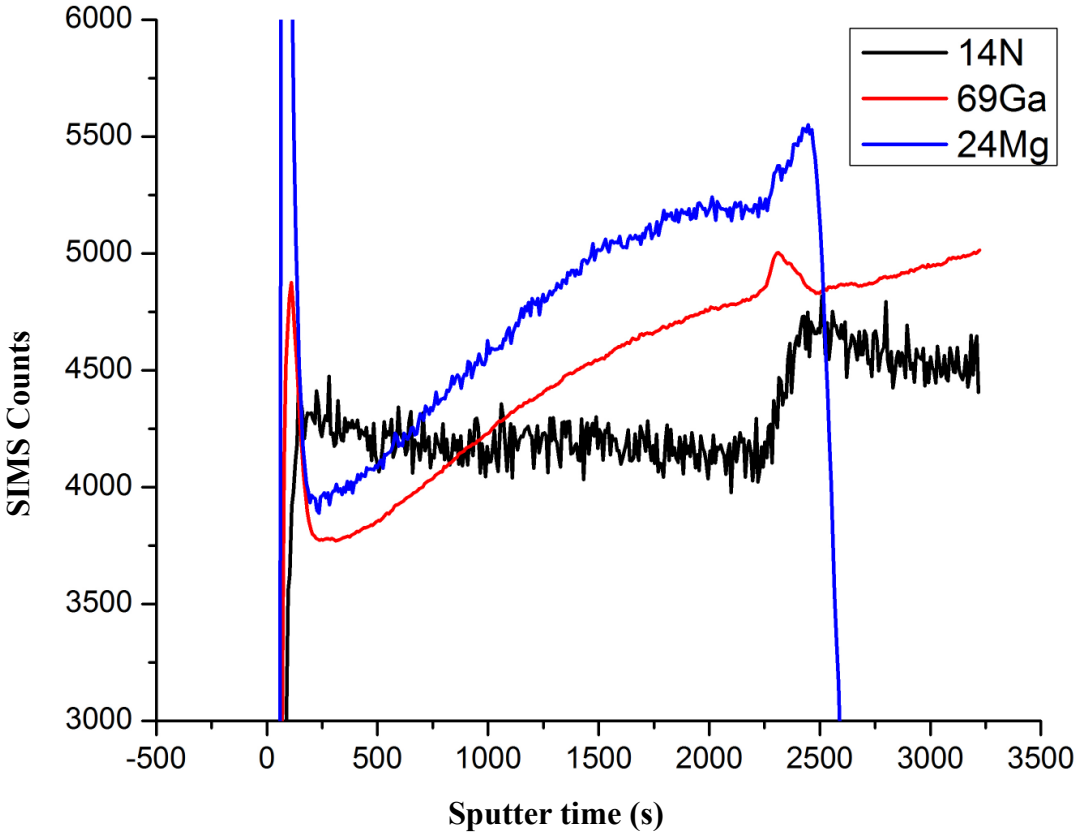

Figure 2.22. Magnified view of signals from Ga, N and Mg ions shown in the Fig. 2.21. Primary current drift is reflected in the matrix element counts. The reason change in sputter yield of N with change in doping of GaN matrix is unclear.

3. DOPANT PROFILING OF *p-i-n* GAN STRUCTURES IN SEM*

3.1 Introduction

Chang and Nixon first reported the observation of contrast between differently doped region of a planar transistor using an SEM in 1967.[50] Multiple groups have subsequently reported on the observation, and the quantification of contrast between layers of differently doped semiconductors.[51–57] Two mechanisms were proposed to qualitatively understand the dopant contrast. One of them attributing the contrast to the difference in band bending at the surface of the p-type, and the n-type regions.[51] The other explained the observed dopant contrast in terms of the spatial variation of vacuum level near the p-n junction, resulting in the variation of ionization energies from p-type, and n-type regions.[55] These explanations were qualitative in nature, and most quantification efforts have primarily focused on analyzing the secondary electron (SE) emission intensity obtained from the SE detector.[58] In one study, surface band bending was measured using Kelvin probe force microscopy (KPFM) which was then correlated to the SE emission intensity by using one dimensional constant loss theory.[53] Therefore the quantification efforts so far have been relative in nature. In this work we have explored a novel method to quantify the electron emission without the use of the conventional SE detector.

---

*Parts of this chapter have been published as

SR Alugubelli, H Fu, K Fu, H Liu, Y Zhao, FA Ponce, "Dopant profiling in *p-i-n* GaN structures using secondary electrons" *Journal of Applied Physics* **126**, 015704 (2019).

We report on a quantitative approach using secondary electrons (SE) for determining both the lateral and vertical dopant distribution profile in *p*-*i*-*n* GaN structures at a sub-micron scale. The SE emission in a material involves three steps, starting with the generation of SEs inside the bulk by the incident primary electrons, the transport of SEs towards the surface, and their emission by escape into vacuum.[57,59] These steps depend on the diffusion length of electrons in the bulk, mean escape depth of electrons near the surface, band bending due to surface states, and the chemical nature of the surface.[24,51,55,57] The electron transport properties and the nature of the surface states depend on the doping characteristics of the semiconductor. This results in variation of secondary electron emission from differently doped regions.

In this study, we use the specimen itself as a detector to measure the specimen current and to plot the variation in SE yields for differently doped GaN thin films.[27,60] The specimen current maintains charge neutrality as the primary beam interacts with the specimen as depicted in Fig. 3.1. The SE yield is defined as the number of secondary electrons emitted corresponding to each incident primary electrons. The differences in the SE yields, obtained from specimen current measurements can be used to explain the observed dopant contrast in *p*-*i*-*n* GaN structures. The SE emission for differently doped GaN has a strong dependence on the primary electron beam voltage, with highest contrast observed at low electron beam voltages.[51,55,61] We observe a strong correlation between electron yields and the Mg concentration in *p*-GaN. We show that this method can potentially augment the existing quantification methods.[53,58,62]

We analyze the effect of experimental parameters such as electron beam voltage, exposure dose, and specimen surface history on the SE emission contrast associated with

dopants. We find that low voltages in the range of 1 to 2kV optimize the contrast between differently doped regions. *p*-type regions have the highest SE emission, followed by n-type regions, and lowest for un-doped regions. Surface conditions have to be optimal to retrieve any meaningful information from SE micrographs. Lower exposure times and smaller dwell times tend to show higher contrast.

3.2 Experimental

3.2.1 Sample preparation

Cross-section samples for SEM were prepared by mechanical polishing with diamond lapping films down to a grit size of 0.1 µm using a tripod polishing tool. Standard cleaning procedures with organic solvents were used. The samples were dipped in a 1:10 HF solution in de-ionized water to remove residual surface oxidation, and then mounted on a SEM stub using a carbon tape. Silver paste was used to ground the sample to avoid charging effects.

3.2.2 Secondary electron detection and imaging

The SE detector is of the Everhart-Thornley (E-T) type, which uses a scintillator with a thin metal coating biased at a positive potential of about 10 kV to detect low-energy secondary electrons. The signal obtained is a convolution of SEs from the beam-specimen interaction, and BSEs originating from the specimen and from the chamber wall, all traveling within the solid angle of the detector.[24] The E-T detector design characteristics, such as solid-angle coverage and signal amplification, is not suitable for the measurement of the absolute number of emitted electrons. Nevertheless, the E-T detector provides information about dopant distribution in GaN *p*-*i*-*n* structures. Contribution of BSEs to the

SE signal can be reduced by utilizing a through the lens detector or an upper SE detector, which utilizes the magnetic field projected by the objective lens to draw the SE electrons.[27]

The secondary electron images in this study were collected in an FEI XL 30 sFEG microscope, operated at working distances of ~ 3-5 mm, using an E-T SE detector. The working distance was kept as short as possible to optimize secondary electron collection efficiency.

3.2.3 The specimen as a detector

In an SEM, the specimen itself can be used as a detector by measuring the current passing through it.[27] The specimen current represents the difference between the primary beam current and the SE and BSE currents, as depicted in Fig. 3.1. The total electron yield can be determined from the specimen current using a charge balance equation given by

$$I_b = I_{sc} + (\delta + \eta) I_b + \Omega \qquad (1)$$

$$\delta + \eta \approx \frac{I_b - I_{sc}}{I_b} \qquad (2)$$

Where I_b is the primary electron beam current, I_{sc} is the current passing through the specimen, $(\delta + \eta)$ represents the secondary and backscattered electron yields, and Ω represents the rate of change of local charge. Local charge can be ignored in conducting materials, but it is an important factor for insulators.[59] For a conducting material, the electron yield can be deduced using Eq. (2). Given the low BSE yield (~0.35) for materials with atomic number of 38,[24,25] the electron yields plotted in this study are referred to as the variations in SE yields (which we find to be as high as 10).

Specimen current measurements were done in a FEI Nova Nano-lab 200 microscope, with the primary electron beam accelerating voltage varying from 250 V to 12 kV, and the beam currents in the 30 to 50 pA range.

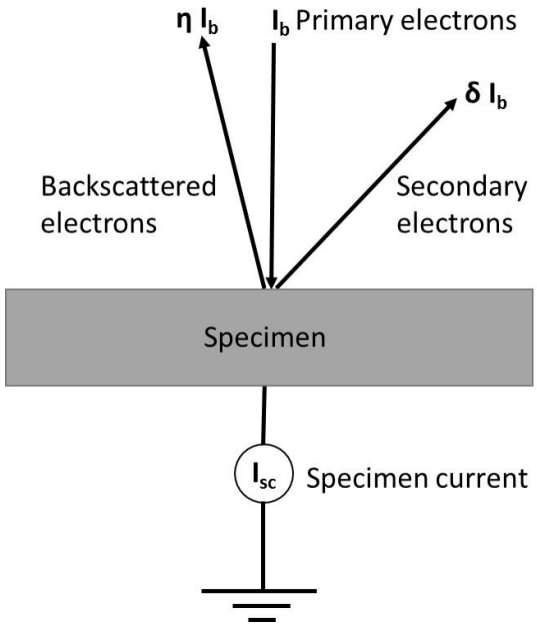

Figure 3.1. Schematic diagram of electronic currents flowing in and out of a specimen in an SEM.

3.3 Results and discussion

3.3.1 Dopant contrast using SE detector at various primary e-beam energies

An SE image acquired at 2 kV from an as-polished surface of a *p*-*i*-*n* GaN thin film structure is shown in the Fig. 3.2. The emission intensity is highest for the *p*-layer, followed by the *n*-layer, and it is lowest for the *i*-layer. The insets in the Fig. 3.3(b) shows SE images of *p*-*i*-*n* structures at 0.25 kV and 5 kV. The contrast between the un-doped and the *n*-type layers vanishes when the voltage is increased from 2 kV to 5 kV, as shown in the inset of Fig. 3.3(b).

The choice of the primary e-beam accelerating voltage is crucial for optimizing dopant contrast in *p*-*i*-*n* GaN thin film structures. The relative SE emission intensities from different layers depend on the primary electron beam accelerating voltage. In order to avoid contrast inversion, and to distinguish all layers, e-beam voltages in the range of 1.5 to 2 kV are preferred. Accelerating voltages below 1 kV can cause a contrast inversion between the *p*-type and the *n*-type layers if the electron dose is higher.

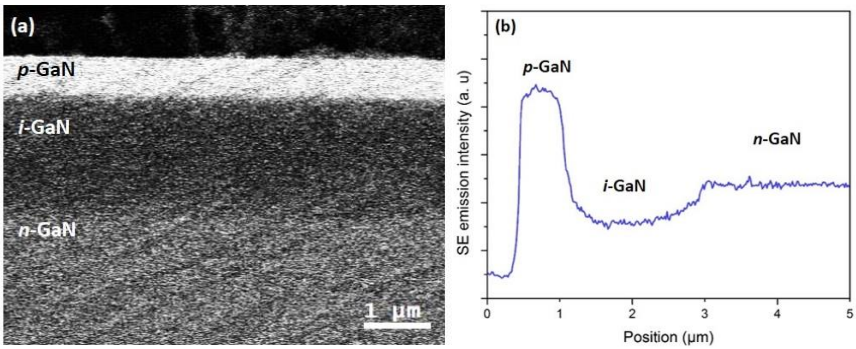

Figure 3.2. SE image and the SE emission intensity profile of the *p*-*i*-*n* GaN structure acquired at primary e-beam energy of 2 kV and beam current of 53 pA.

3.3.2 SE yield dependence on e-beam energy for *p*-, *i*-, and *n*-GaN

Electron yields for *p*-GaN, *n*-GaN, and *i*-GaN are plotted in Fig. 3.3(a). The electron yield is highest for *p*-GaN, followed by *n*-GaN, and it is lowest for *i*-GaN. The maximum electron yield occurs at ~1.25 kV for *p*-GaN, and at ~0.5 kV for both *i*-GaN and *n*-GaN. The difference in electron yields for *p*-GaN and *n*-GaN is shown in the Fig. 3.3(b). Yield difference for *p*-GaN and *n*-GaN is highest for the voltage range of 1 to 2 kV. It is important to note that the yield difference does not have any contribution from BSEs, since BSEs should be independent of doping. Also, the electron yields for the *i*-GaN and the *n*-GaN are equal for the voltages above 3 kV. This can be observed in the SE images in the inset of Fig. 3.3(b), where the contrast between the *i*-GaN and the *n*-GaN vanishes at 5 kV.

The electron yield measurements for our case are similar to the measurements reported by Yater et al.[63]

The dependence of the SE yield with primary electron beam voltage is similar for most materials.[64] The yield initially increases up to a maximum value, and then decreases with voltage. This is related to the penetration depth of the primary electrons and to the escape depth of the secondary electrons. The penetration depth increases with beam voltage, and the total number of local secondary electrons increases with excitation volume. Below the voltage at maximum electron yield (V_m), the penetration depth is lower than the escape depth of secondary electrons, resulting in the secondary electrons escaping into vacuum. The penetration depth and escape depth are equal at V_m. Above V_m, the penetration depth is higher than the escape depth of the secondary electrons, resulting in many SE's losing energy before reaching the surface. Therefore, for voltages greater than V_m, the electron yields are lower despite the higher number of secondary electrons generated inside the material.

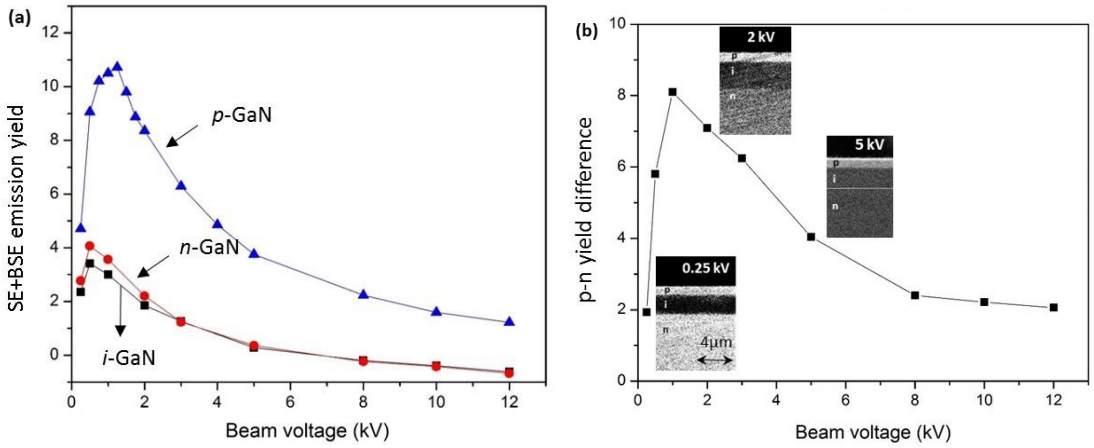

Figure 3.3.(a) Variation in electron yields for *p*-GaN, *n*-GaN and *i*-GaN plotted for primary e-beam energies ranging from 0.25 kV to 12 kV. (b) SE Yield difference between *p*-GaN and *n*-GaN for corresponding e-beam energies. Inset shows SE images of *p*-*i*-*n* structure at 0.25 kV, 2 kV, and 5 kV.

There are two possible explanations for the dopant contrast mechanism. First, Perovic *et al.* attributed the dopant contrast observed in silicon systems to the band bending near bulk-vacuum interface due to the presence of surface states.[51] Later, *Sealy et al.* attributed the observed contrast in Si systems to differences in ionization energies of differently doped regions due to the built-in potential near the surface.[55] Volotsenko *et al.* used semi-empirical 1-D dimensional constant loss theory proposed by G.F Dionne to simulate the dopant contrast observed in Si system.[53,64] They found that the escape depth parameter is the major factor influencing the dopant contrast in Si based systems. Escape depth depends on the electric fields induced by the surface band bending which varies with the dopant type and concentration. The concept of ionization energy does not seem to apply to our case since *i*-GaN has the lowest SE emission (*i*-GaN would be expected to be between the *p*- and *n*-GaN), as explained next. The lower SE yield for *i*-GaN can be attributed to its inability to replenish some of the SE electrons because of the lower

conductivity.[65] In the case of *p*-GaN and *n*-GaN, surface states result in downward and upward band bending near the surface, respectively.[66–68] Using photoelectron and X-ray photoemission spectroscopies at low temperatures, the value of E_f - E_v at the surface has been reported to be about 2.7 eV for *n*-type GaN, and about 1.3 eV for *p*-type. These values correspond to upward band bending of 0.7 eV for *n*-type, and downward band bending of 1.1 eV for *p*-type, as shown schematically in Fig. 3.4.[66,67,69] Downward band bending near the surface of *p*-GaN contributes to electron transport towards the surface, thus enhancing SE emission. On the other hand, upward band bending near the surface of *n*-GaN tends to deplete electrons from the surface, thus diminishing SE emission.[12,20]

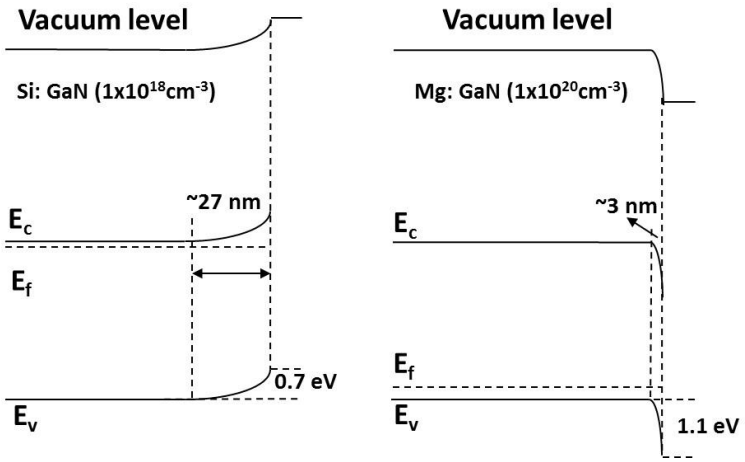

Figure 3.4. Schematic diagram of band bending near the surface for *p*-GaN, and *n*-GaN.

2.3.3 SE yield dependence on Mg concentration in *p*-GaN

Electron yields have a strong positive correlation with Mg concentration as shown in Fig. 3.5(a). Figure 3.5(b) shows the SE emission intensity recorded with an SE detector for *p*-GaN films with different Mg concentrations. The inset shows the relative contrast for the three *p*-GaN films.

The signal recorded using an SE detector is not absolute since it depends on the detector sensitivity, its collection solid angle, and several operational microscope parameters. Therefore, the quantification from the intensities recorded can only be relative.[56,70–72] On the other hand, the specimen current minus the incident beam current provides an absolute value for the total number of emitted (BSE and SE) electrons, which is represented in Fig. 3.5. This method can potentially be used for quantitative dopant profiling of *p*-GaN by first calibrating the electron yields with different Mg concentrations.

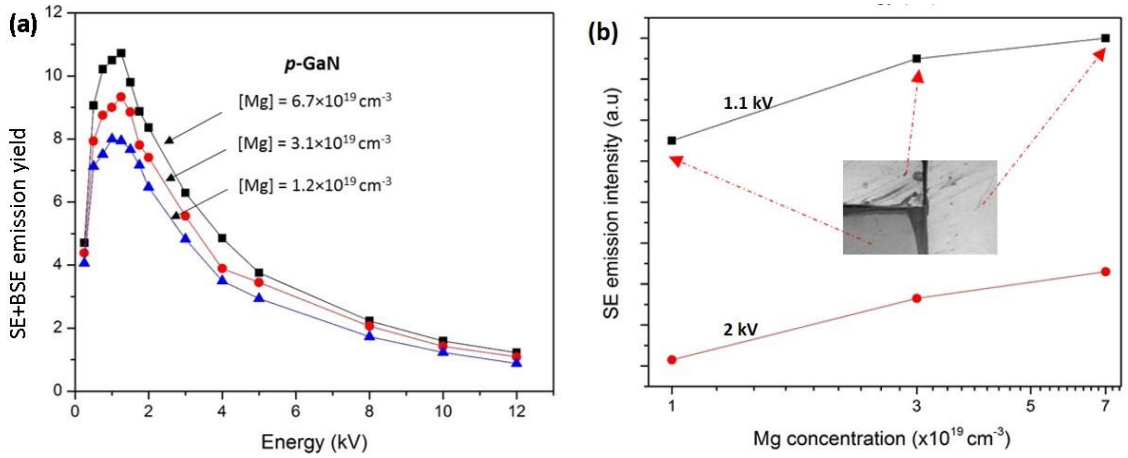

Figure 3.5. Electron emission characteristics for Mg-doped GaN. (a)Variation in electron yields as a function of primary e-beam energy for various Mg concentrations. (b) SE emission intensity dependence on Mg concentration for different primary e-beam energies.

3.3.4 Effect of the nature of the surface on secondary electron emission

The nature of surface significantly affects the observed dopant contrast. SE emission is affected by factors like work function, surface Fermi pinning position, and the doping level. These in turn determine the surface depletion width, the electric field strength, and the electron scattering length.

Figures 3.6 show the effects of air and UV exposure on the SE emission from *p-i-n* GaN thin film structures. A clear reduction in contrast is observed in both cases. HF treatment on a UV exposed surface restores the contrast between layers. (Fig. 3.6).

The SE emission contrast is highest in *p-i-n* GaN thin film structures for freshly polished samples (Fig. 3.2). Oxidation of the surface tends to diminish the contrast observed between layers possibly due to increase in surface work function. Etching the oxide layer formed on the GaN surface using dilute HF restores the contrast between layers. Therefore, a clean surface is crucial for observing optimal dopant contrast.

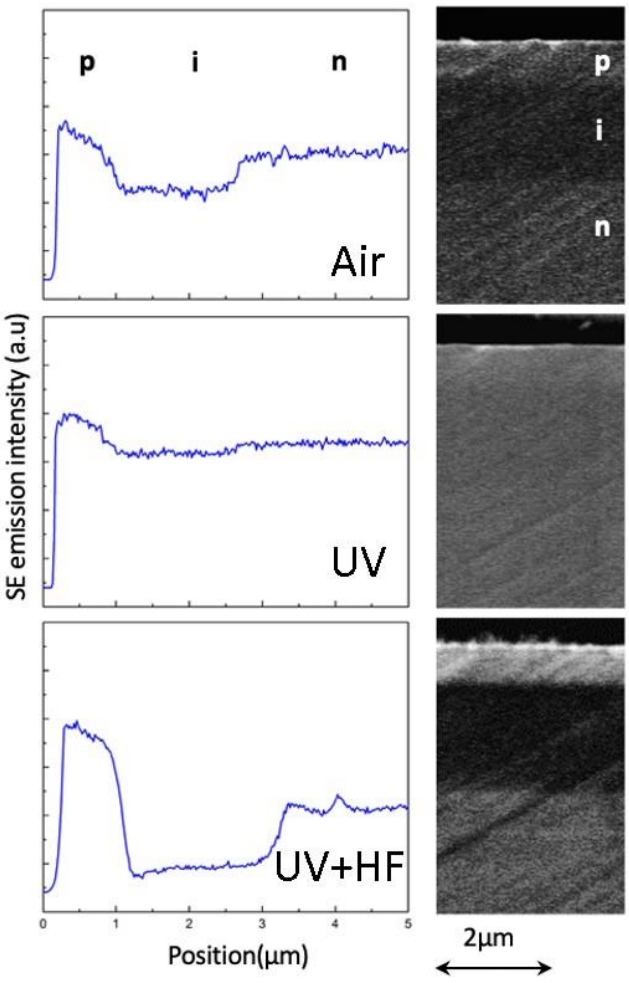

Figure 3.6. SE emission intensity profiles, and images of a *p-i-n* GaN structure with surfaces that were exposed to air for 2 days, exposed to UV for 2 hours, and treated with HF after UV exposure.

3.3.5 Effect of beam dwell time and exposure time

For observing optimal dopant contrast, faster scan rates and lower exposure times are necessary. The contrast observed between *p*-GaN and *n*-GaN layers using an SE detector may be quantified as follows,

$$C_{pn} = \frac{I_p - I_n}{I_n}$$

Where I_p and I_n are the recorded intensities from the *p*- and *n*-layers respectively. Scan rates and exposure time have a significant effect on the dopant contrast.[73] The effect of e-beam dose on C_{pn} is plotted in Fig. 3.7(a). The dose is defined as the product of beam current per unit area and dwell time. The contrast decreases with increasing electron dose. This could possibly be resulting from the flattening of bands near the surface (similar to photovoltaic effect on Fermi level pinning). The dependence of C_{pn} on beam exposure time is plotted in Fig. 3.7(b) for different e-beam voltages. We observe a gradual decrease in contrast with exposure time for 2 kV and 5 kV. The change in contrast could be due to the contamination build-up after prolonged beam exposures. For 10kV, we observe an increase in contrast with time, which may be related to the penetration depth of about 700 nm. The diffusion length of electrons in *p*-GaN increases with time resulting in a higher number reaching the surface at prolonged exposures, which has been attributed to charging of deep levels associated with Mg doping.[74] In conclusion, anomalies in the dopant contrast can be avoided by minimizing electron dose and exposure time.

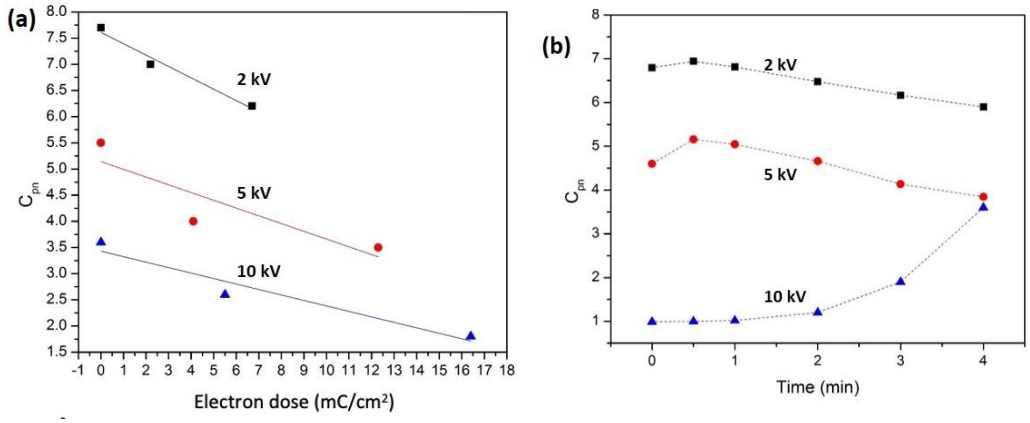

Figure 3.7. SE emission contrast (C_{pn}) of *p-n* GaN structures, for primary e-beam energies of 2 kV, 5 kV, and 10 kV: (a) As a function of electron dose for a single scan. (b) As a function of total exposure time with an electron dose rate of 30 μC/cm^2.s. The raster area in these measurements is 15.5 μm X 11.7 μm.

3.3.6 Applications on high power devices

In power devices, lateral and vertical patterns of *p-i* and *p-n* junctions are used for power delivery. The patterns are produced by a variety of methods such as etch-and-regrowth of differently doped regions or by ion implantation. Devices require good edge definition of the differently doped regions. Faulty material results in high leakage currents and low reverse breakdown voltages. Direct visualization of actual geometry of differently doped regions is important in order to understand the nature of the device structure and performance.

We have utilized SE imaging to visualize the selective area doping. For instance, the horizontal and vertical dopant distribution can be identified from the SE image of the *p-i-n* GaN etched mesa structure in Fig. 3.8(a). The dopant profiles are useful for understanding the growth mechanisms along different crystal orientations, and the lateral

electron transport properties. Another example is in the study of Mg passivation using a H_2 plasma treatment. Fig. 3.8(b) shows an as-grown *p-i* GaN junction partially covered with a metal anode. Fig. 3.8(c) shows a similar region after the H_2 plasma treatment with thermal annealing, revealing a clear difference in the SE emission characteristics for the hydrogenated *p*-GaN region. The exposed *p*-GaN region is deactivated and exhibits *i*-type SE contrast. Edge termination using H_2 plasma treatment can potentially avoid etch damage, and achieve lower leakage currents.[75]

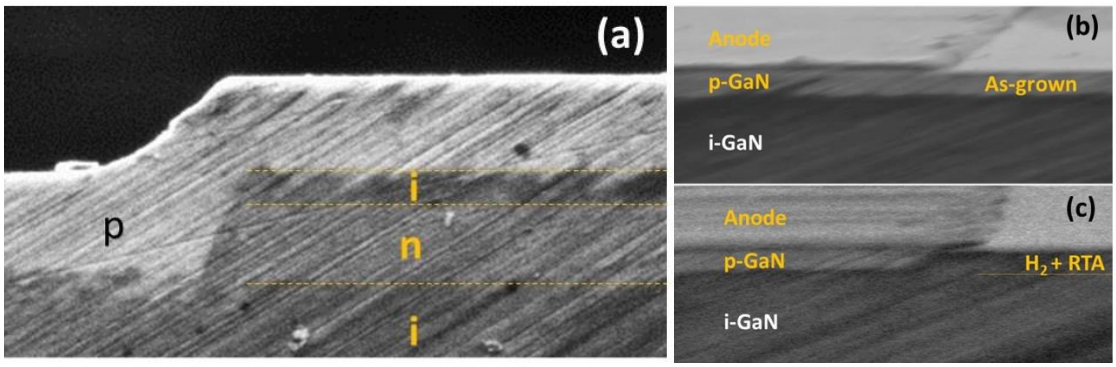

Figure 3.8. SE images of (a) Etched-and-regrown *p-i-n* GaN mesa structure, (b) as-grown *p*-GaN, (c) H_2 + RTA annealed *p*-GaN.

Figure 3.9 shows application of H_2 passivation technique to create a guard ring structures by depositing multiple metal rings on the *p*-GaN. Such structures can improve the breakdown voltage by spreading the electric fields. Introduction of guard ring has increased the breakdown voltage to ~1.7 kV as to ~1 kV for a reference *p-i-n* diode. Dopant profiling using SE's is very helpful for understanding and simulating the performance of such structures.

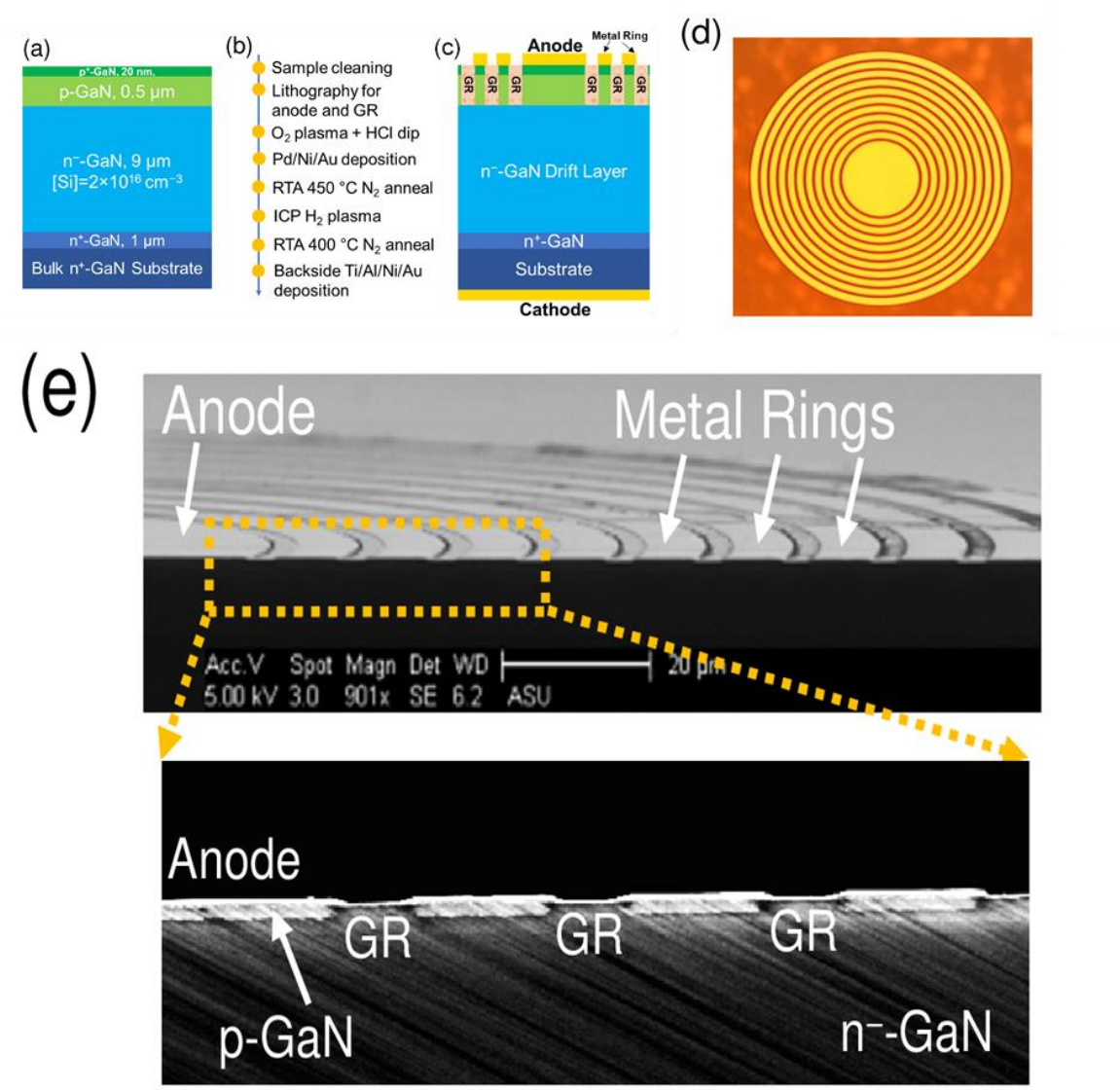

Figure 3.9. (a) Schematic view of the cross-section of the epilayers. (b) Fabrication process for the devices with GRs. (c) Cross-sectional schematics of the devices with GRs. (d) Optical microscopy image (top view) of the p-n diodes with 10 GRs. (e) SEM images of the cross-section of the devices with GRs.

Figure 3.10 shows schematic diagram of trench structures fabricated for the study of leakage current dependence on the trench depth. Leakage current depends on the efficiency of Mg incorporation in *p*-GaN near the sidewalls (gate region), etching profile

(determines the electric field crowding near the edges), surface damage induced due to plasma etching.

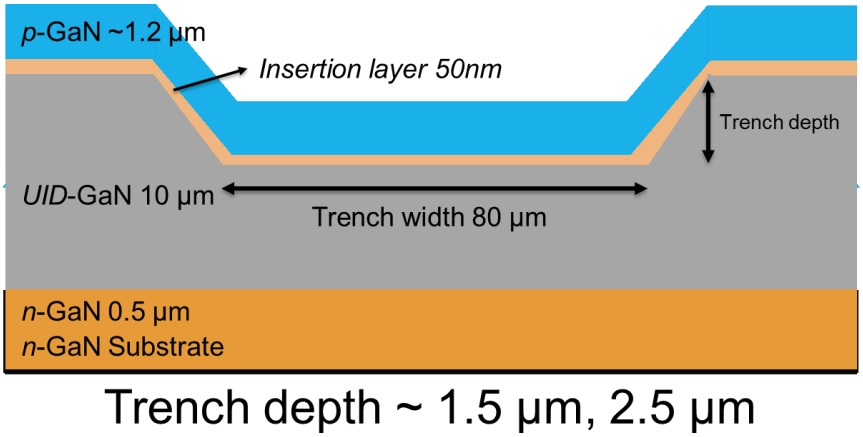

Figure 3.10. Schematic diagram of trench structures for study of leakage current dependence on the trench depth.

Figure 3.11 shows the dopant profiles near sidewalls for different trench depth. Clear differences in the etching profiles can be seen with different trench depths. The angle of etching seems to get steeper with the etch depth. The corner angle are well defined for lower trench depth. The edges seem to be rounded with the increasing trench depths. There seems to be a deeper etch near the mesa bottom corner for trench depth of 2.5 µm. The thin insertion layer can be seen in both the cases. The idea is to move the defective regrowth interface away from the *p*-GaN. The relative SE emission from the insertion layer in deeper trenches is higher. This may be due to crystal defects induced by the etching process.

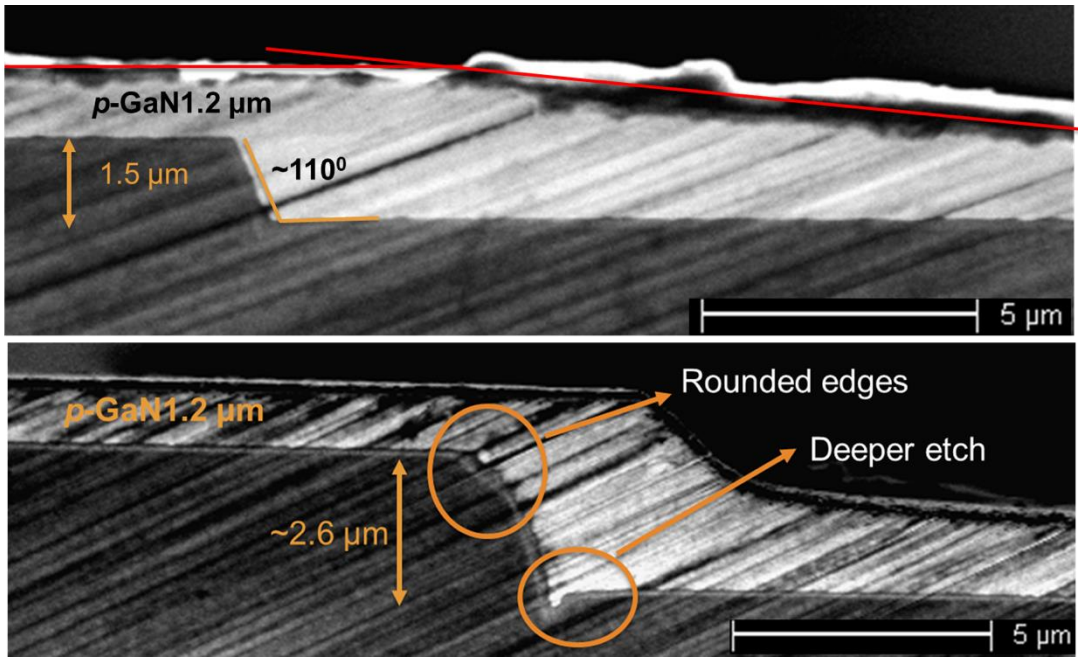

Figure 3.11. Dopant profiles of trench structures with etch depths of 1.5 µm and 2.6 µm.

4. STUDY OF ETCH AND REGROWN INTERFACES IN GAN *p-i-n* STRUCTURES*

4.1 Introduction

A typical power semiconductor switch consists of gate, source, and drain which are essential for controlling the current flow. For example, vertical junction field effect transistor (VJFET) is one of the device designs, which has *p*-GaN region as the gate, undoped GaN (*i*-GaN) as the drift region, and *n*-GaN acting as source and drain. This device design is lucrative due to its superior theoretical device performance in terms of lower switching losses as compared to that of SiC.[76] Such device designs require selective area doping, which are typically realized via etch-and-regrowth or by ion implantation and annealing.[13,14] Etch and regrowth strategy can be relatively easy to implement as compared to ion implantation, given the necessity for annealing in high pressure environment to reduce the lattice damage.

Typically, the gate region (*p*-GaN) is operated at a small positive voltage of 0-10V, drain (*n*-GaN) held at high positive voltage, and the source region (*n*-GaN) is connected to the ground. This translate to a *p-i-n* structure operating at a high reverse bias voltage.

---

*Parts of this chapter have been published as

SR Alugubelli, H Fu, K Fu, H Liu, Y Zhao, MR McCartney, FA Ponce, "Electronic band structure using electron holography on etched-and-regrown GaN *p-i-n* diodes" *Applied Physics Letters* **115**, 201602 (2019) DOI: 10.1063/1.5127014.

Simple *p*-*i*-*n* diodes with regrowth interfaces are investigated to understand the impact of the etching on the diode performance. It has been found that regrowth of *p*-GaN directly over etched *i*-GaN surface results in lower breakdown, and very high leakage currents.[77–79] Introduction of a thin un-doped layer before the regrowth of *p*-GaN films recovers the diode performance.[79] In order to address this issue, it is important to understand the nature of the regrowth interface. Thin un-doped underlayers have been employed in GaN based LED's, with improved electrical characteristics.[80,81]

Typically, in GaN, silicon (Si) and magnesium (Mg) are used as the *n*-type and *p*-type dopants respectively. The activation energies for Si and Mg are about 25 meV and 200 meV respectively. Device quality *n*-GaN is doped with ~10^{18} cm^{-3} which result in the donor concentrations of the same order of magnitude. For *p*-type doping in GaN, Mg concentrations of ~10^{19} cm^{-3} result in acceptor concentrations of ~2 x 10^{17} cm^{-3} post thermal annealing at about 750^{o}C, corresponding to 1-2% ionization. The background impurity concentration in a typical MOCVD chamber is ~10^{15} - $10^{17}$$cm^{-3}$ depending on the condition of the reactor. Thus, undoped GaN (*i*-GaN) has donor concentrations of the same order or magnitude.

In this study, we analyze the electrostatic potentials across the *p*-*i*-*n* structures, to understand the charge distribution near the interfaces. The electrostatic potentials provide us with an insight into the variations from intended dopant distribution in the structures, and identify the interface trap states induced by the etch-and-regrowth process. To obtain the potential profiles across the interfaces, we employ electron holography (EH) in a transmission electron microscope (TEM). EH is an interferometric technique which can used to retrieve both the phase shift, and amplitude with respect to the vacuum. We show

that etch and regrowth introduces high density of charges near the regrowth interfaces resulting from the presence of impurities at these interfaces, and damage induced by etching. Introduction of a thin un-doped layer over the etched surface, yields diodes with electrical performance equivalent to that of as-grown diodes. This is a result of Mg doped GaN being moved away from the regrowth interface.

4.2 Experimental details

The GaN *p*-*i*-*n* structures in this study are grown using metal-organic chemical vapor deposition (MOCVD) on an *n*-GaN substrate with carrier concentration of ~10^{18} cm^{-3}, at a growth temperature of ~1040^{o}C. The precursors were tri-methyl gallium (TMGa) and ammonia (NH_3), with H_2 as the carrier gas. Bis(cyclopentadienyl)magnesium (Cp_2Mg) and silane (SiH_4) were the sources for Mg and Si.[82] The background impurities for *i*-GaN in our reactor were measured using SIMS to be Si ~ $6x10^{15}$ cm^{-3}, O ~ $4x10^{15}$ cm^{-3}, and C ~ $3x10^{16}$ cm^{-3}, as observed in Fig. 4.7

4.2.1 Reactive ion etching of GaN

A chlorine-based inductively coupled plasma (ICP) dry etching recipe was used to etch the samples in this study. Etching was carried out on a Plasmatherm Apex ICP equipment using a 13.56 MHz RF power supply at a pressure of 5 mtorr. The etching rates for RF power is shown in the table 4.1. Silicon was used as the carrier wafer. The etching rates are based on the optimized parameters for obtaining smooth GaN surfaces.

Table 4.1 Parameters for ICP etching of GaN.

ICP power	RF power	Cl_2 (sccm)	BCl_3 (sccm)	Ar (sccm)	Etch rate
400	70	30	8	5	~ 288 nm/min
400	35	30	8	0	~ 140 nm/min
400	5	30	8	0	~ 20 m/min
400	2	30	8	0	~ 8 nm/min

Before the regrowth, samples were first treated with UV-ozone for 45 minutes to oxidize the surface. The samples were then immersed in hydrofluoric (HF) acid, and hydrochloric (HCl) acid for 5 minutes each to remove contaminants. Such treatment has been proven effective in reducing the surface contaminants before the regrowth of material. The charge concentrations near the regrowth interfaces was reported to be least after the above mentioned surface treatment.[3,13,79]

It has been reported that the ICP etching of GaN can results in sub-surface layers that are non-stoichiometric.[83–85] Exposure to air post-etching can oxidize the surface. Presence of deep donors of concentration levels ~$1x10^{20}$ cm^{-3} close to the surface, with estimated layer thickness of 5-8 nm was reported in XPS studies on ICP etched *p*-GaN surfaces.[85] In ICP etched *n*-GaN surfaces, presence of deep acceptors was reported based on XPS measurements.[83,84] Understanding the effect of regrowth interfaces near *p-i* junction is crucial in order to effectively incorporate etch-and-regrowth processes in fabrication of GaN based power devices.

4.2.2 Samples for electron holography studies

In most structures, thickness of the *p*-GaN layer is 500 nm to 1 μm. But studying such samples using holography can be challenging due to the restricted field of view. In order to have the interface of interest within the field of view, the *p*-GaN layer is etched to final thicknesses of about 150 nm using standard process mentioned earlier.

The TEM specimens are prepared using wedge polishing technique on a tripod polisher, and are then thinned to electron transparency using 2-3 kV Ar^+ beam. Silver paste is used to ground the samples to avoid charging due to electron beam irradiation in the TEM. Electron holograms are acquired on a FEI Titan microscope operated at an electron beam accelerating voltage of 300 kV, equipped with a quartz biprism biased at 160V. The holograms were acquired in weakly diffracting condition keeping the interfaces of interest edge on. The phase shift and amplitude were retrieved using the standard process. The electrostatic potential (V) is calculated from the phase shift (Δ∅) of image using the eq. 1, where C_e is microscope constant (0.00653 for 300 kV electrons) and t is the thickness of the TEM sample. The charge distribution (ρ) is obtained using Poisson's equation as shown in eq. 2, where ε is the dielectric constant of the material.

$$\Delta\emptyset = C_e V t \qquad (1)$$

$$\rho = \varepsilon \nabla^2 V \qquad (2)$$

The built-in potentials in *p-n* junctions measured using electron holography technique are usually lower than the actual values. This is due to the presence of electrically dead layers, and surface states on either sides of the thin TEM specimen.[33,86] In our study, the energy scales on the potential profiles are adjusted to GaN *p-n* junction built-in

potential of about 3.2 eV. The inelastic mean free path for 300 keV electrons in GaN used in our studies is 100 nm.[87]

Potential profiles of four structures are investigated in this study. Two of them are continuously grown *p*-*i*-*n* diodes with different *i*-GaN thickness (0.1 μm and 10 μm). The objective is to examine the potential profiles for as-grown structures, at *p*-*i* and *i*-*n* interfaces. The structure in Fig. 4.11(b) places the *i*-*n* interface in the field of view for electron holography. The other two structures include an etched and regrown interface at the *p*-*i* junction, one with *p*-GaN directly on top of the etched surface, and one with an intermediate 50 nm un-doped layer over the etched surface. The structure with *p*-GaN grown directly on top of the etched surface has very low breakdown voltage as compared to the as-grown diode. The structure with an intermediate 50 nm un-doped layer over the etched surface has I-V characteristics comparable to that of the as-grown diode.

4.3 I-V and C-V measurements of GaN *p*-*i*-*n* structures

Figure 4.1 shows the I-V measurements for continuously grown, and etched-and-regrown GaN *p*-*i*-*n* diodes. No field plates or passivation was used for the I-V measurements shown in Fig. 4.1. The metal contact diameter was 80 μm. Continuously grown (non-etched) diodes have excellent blocking voltages with low leakage currents of the order 1 nA. Regrowth of *p*-GaN directly over an etched surface results in a diode which has premature breakdown, and high leakage currents. Also, the introduction of a 50 nm un-doped layer over the etched surface results in recovery of the diode behavior, with the I-V characteristics close to the as-grown *p*-*i*-*n* diode.

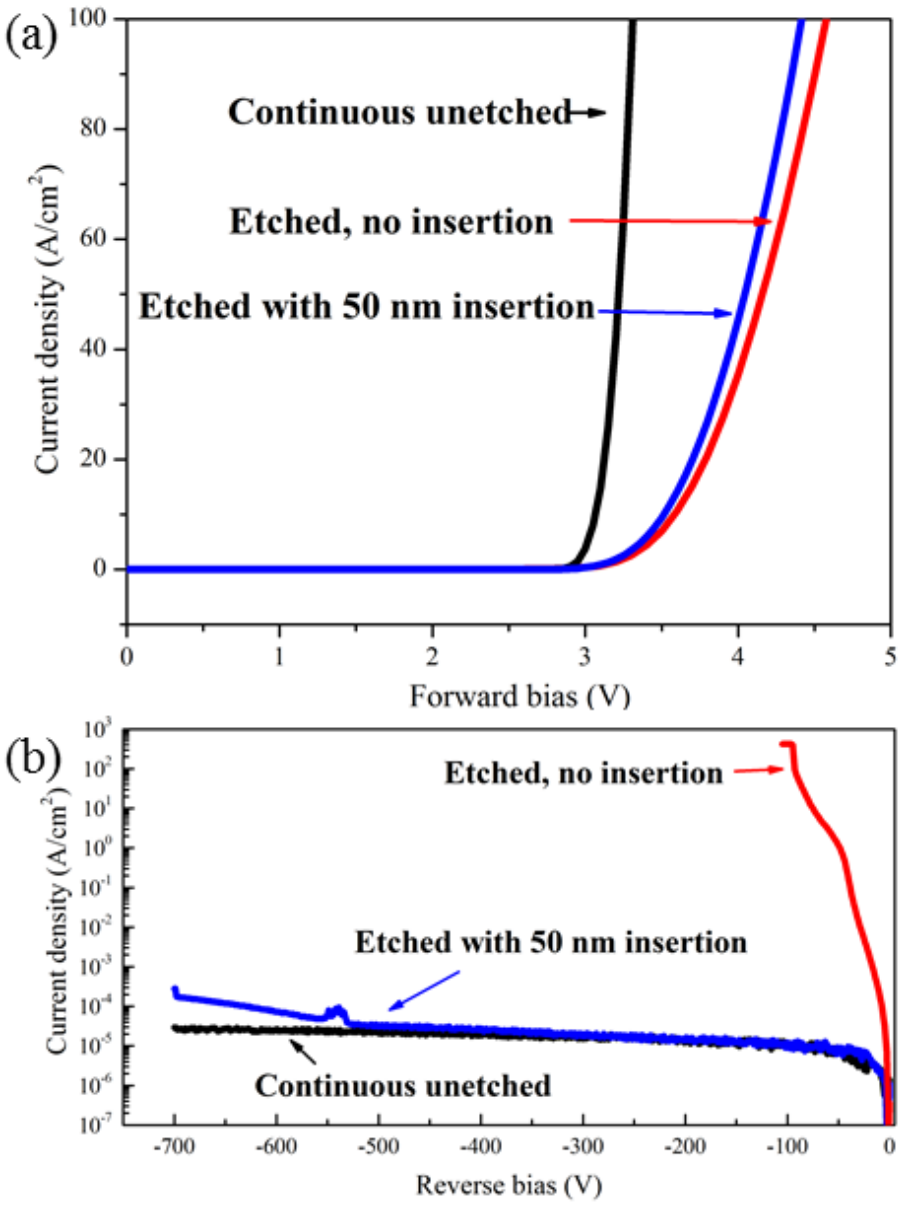

Figure 4.1. I-V characteristics of different GaN *p-i-n* structures.

With slower etch rates, the best leakage currents for the diodes with an insertion layer is 5 nA at 600V. Addition of a thin un-doped layer tends to recover the performance of the diode.

Also, forward current density for the GaN *p*-*i*-*n* structure with *p*-GaN regrown directly over the etched surface increase slightly with temperature (Fig. 4.2). The reverse current densities are independent of temperature suggesting Zener tunneling as the dominating transport mechanism.[13]

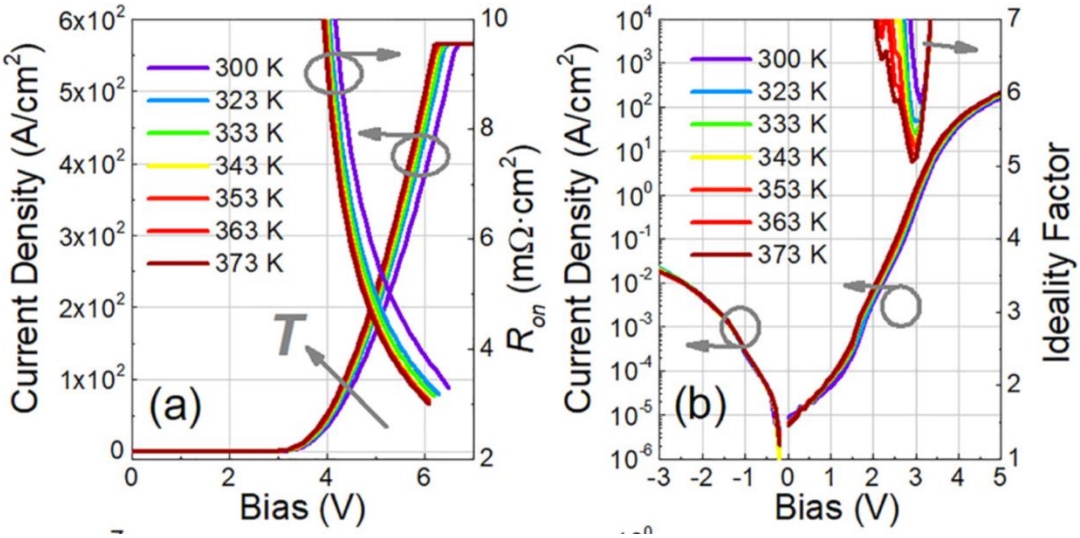

Figure 4.2. Temperature dependent I-V characteristics of GaN *p*-*i*-*n* structures with *p*-GaN grown directly over etched *i*-GaN in (a) Forward bias (b) Reverse bias.

Such tunneling behavior is not observed in the case of diodes with an un-doped layer grown on top of the etched surface. From these results it can be inferred that having an etched interface between the *p*-GaN, and *i*-GaN can be detrimental for holding high blocking voltages.

Capacitance voltage measurements on a *p*-*n* junction can provide information about the charge distribution within the diode. Any interface charges can be identified with C-V measurements. Figure 4.3 shows C-V measurements for diodes with regrown interfaces.

High density of charges was reported at the regrowth interface. Typically, the charge density is in the range of 10^{19} cm^{-3} at the regrowth interface.[13]

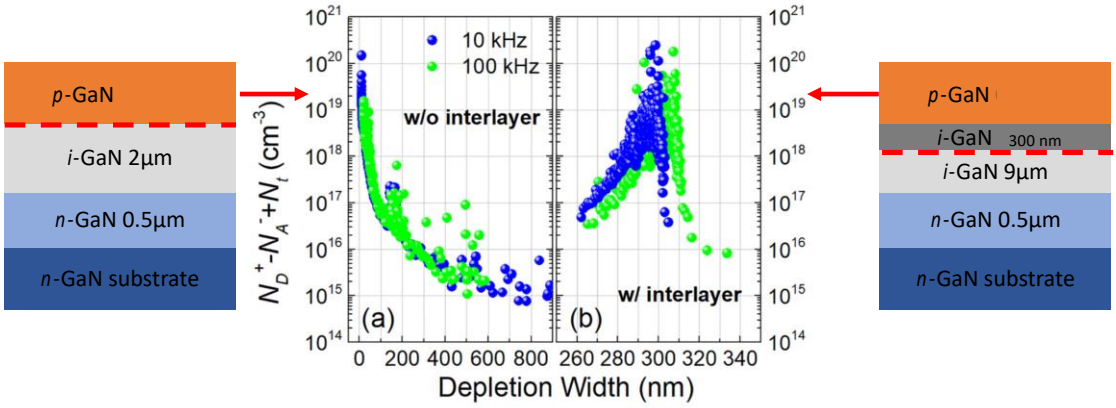

Figure 4.3. C-V measurements for regrown GaN *p-i-n* diodes with and without insertion layer. (Red dotted line indicates the etched interface)

Such charges are not present in the case of continuously grown diodes. This indicates that the etch-and-regrowth process introduces charges at the interfaces. In order to understand the origin of these charges, TEM analysis is performed to look at any structural defects introduced by the etching process. Also, SIMS analysis is performed in order to identify any impurity accumulation at the interfaces.

4.4 TEM and SIMS studies on GaN *p-i-n* structures

TEM analysis is performed on continuously grown GaN *p-i-n* structures, and etched and regrown structures. SIMS analysis is performed to understand the impurity accumulation at the regrowth interfaces.

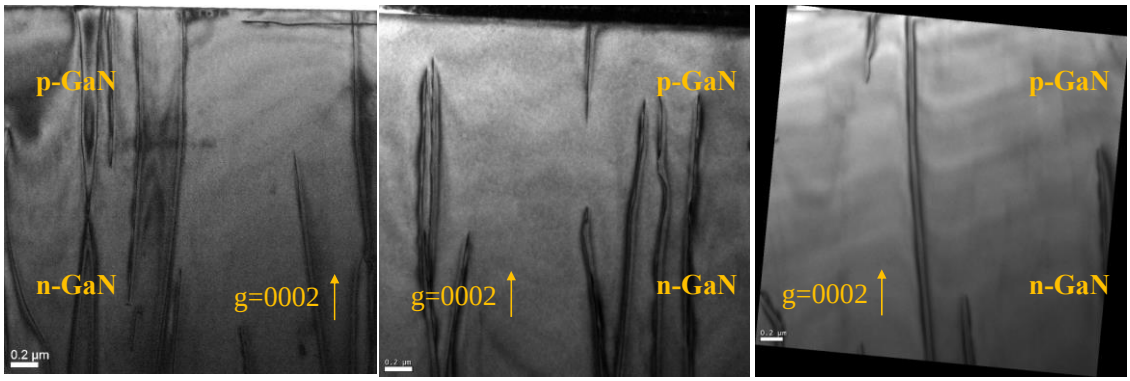

Mg flow rate : 50 sccm
[Mg] ~ 1 x 10^{19} cm^{-3}

Mg flow rate : 100 sccm
[Mg] ~ 3 x 10^{19} cm^{-3}

Mg flow rate : 200 sccm
[Mg] ~ 7 x 10^{19} cm^{-3}

Figure 4.4. Two beam bright field images of continuously grown GaN *p-n* junction with different Mg concentrations.

The above structures (Fig. 4.4) are grown under same conditions except for the Mg flow rate. The Mg flow rate is varied to change the Mg concentration in the *p*-GaN film. No structural defects at the interface between the *p*-GaN, and *n*-GaN can be observed. Threading dislocation can be seen in the images which arise due to the lattice mismatch between the sapphire substrate, and the GaN layers.

In case of etched and regrown structures with *p*-GaN directly over the etched *i*-GaN surface, precipitates can be clearly observed at the regrown interface (Fig. 4.5 and Fig. 4.6). These precipitates are present irrespective of the Mg concentration in the *p*-GaN film.

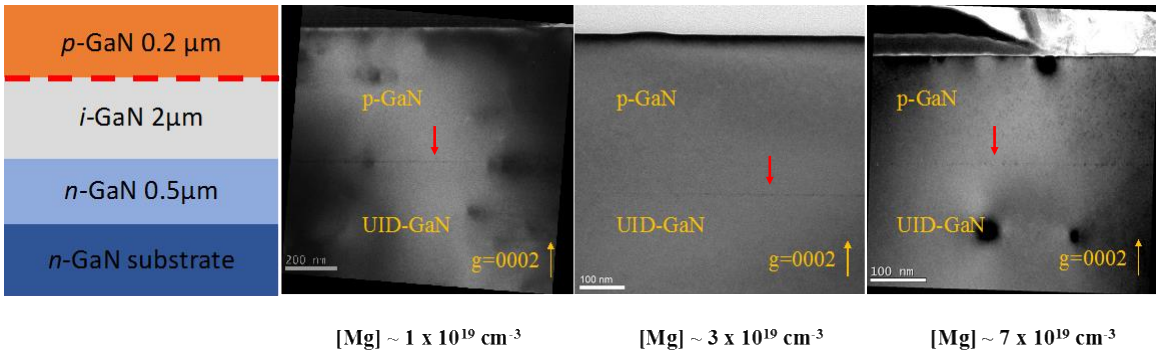

Figure 4.5. Two beam bright field images of *p*-GaN grown directly over etched *i*-GaN surface for different Mg concentrations. Red arrows indicate the etched interface (red dashed line in the schematic diagram).

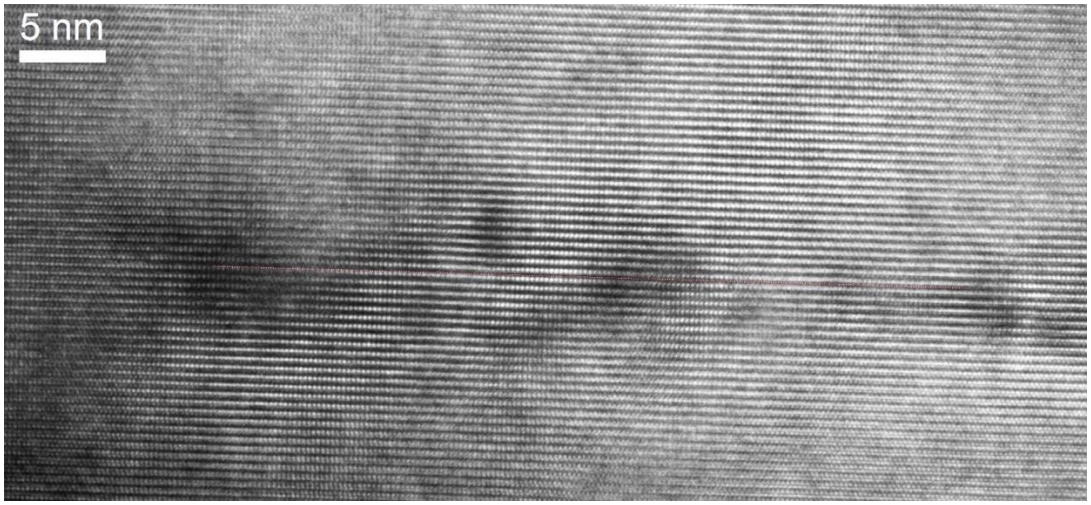

Figure 4.6. High resolution image of interface region with *p*-GaN grown directly over etched *i*-GaN.

The structures shown in Fig. 4.5 are grown on GaN substrate with every parameter remaining the same except for the growth rate for the *p*-GaN film. Growth rate of the *p*-GaN film is varied to obtain films with different Mg concentrations. The growth rates for

the films shown above are 2 μm/hr, 1 μm/hr, 0.5 μm/hr respectively from left to right. Faster growth rate of *p*-GaN results in lower incorporation of Mg into the film. High magnification image of the regrowth interface for samples above is shown in Fig. 4.6. The non-uniform distribution of precipitates can be seen with their size varying between 5 and 15 nm.

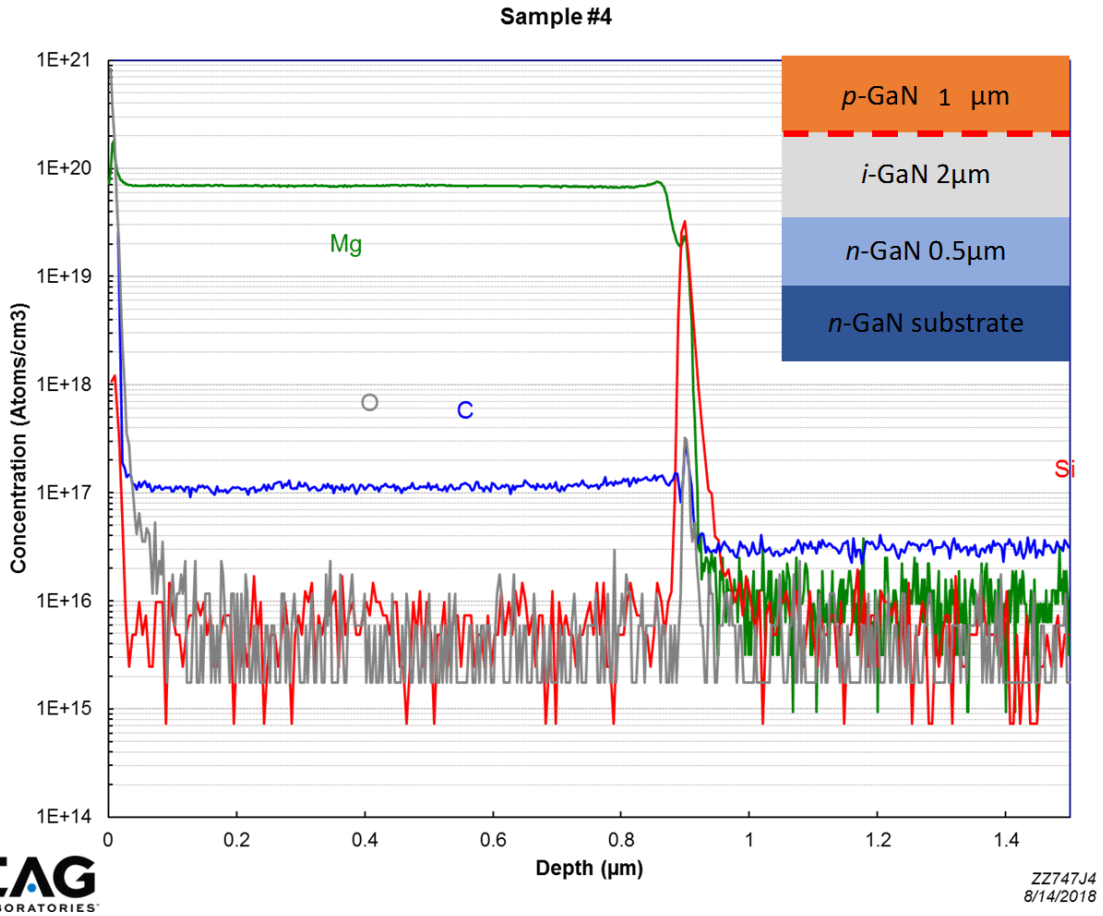

Figure 4.7. SIMS analysis of Mg, Si, C, and O impurities on etched-and-regrown structure shown in the inset.

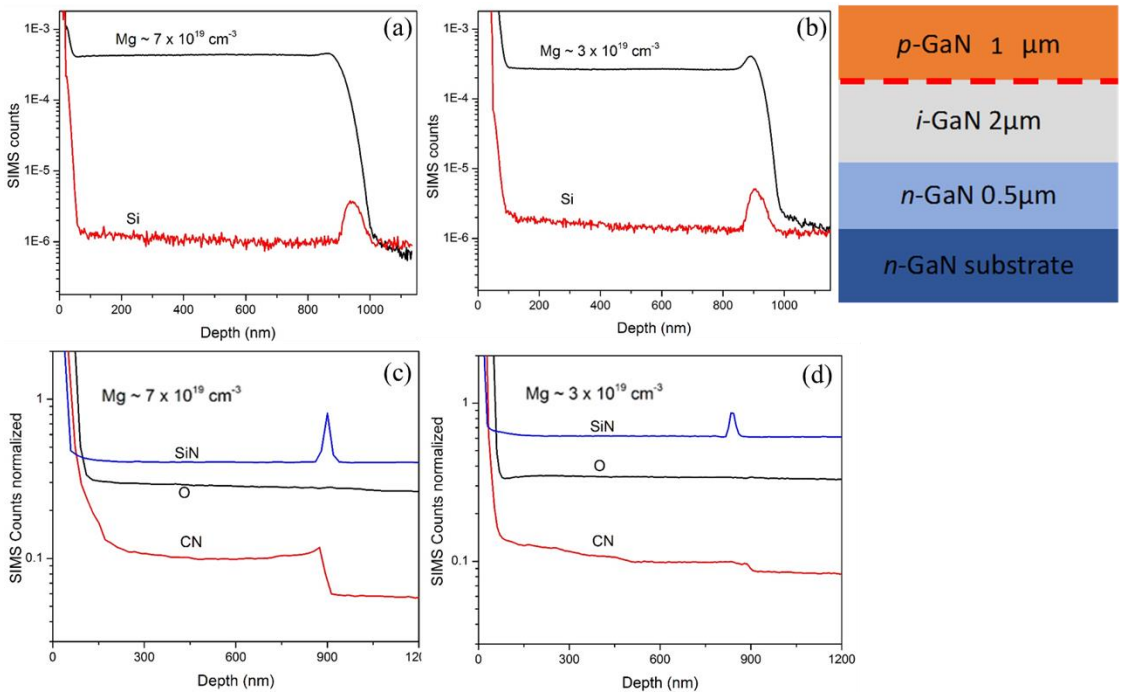

Figure 4.8. (a), (b) Mg and Si profiles obtained simultaneously with O_2^+ beam. (c), (d) Si, O, and C profiles obtained with Cs+ beam. The structure is indicated. These measurements are performed at ASU.

SIMS measurements on the regrowth structures with Mg doped GaN grown directly over etched *i*-GaN surface indicated presence of excess Mg, and accumulation of Si, O at the regrowth interface. (Fig. 4.7 and Fig. 4.8) From the SIMS analysis, it appears that the precipitation at the regrowth interface may be related to presence of excess Mg. The carbon content is higher in the *p*-GaN film as compared to *n*-GaN.

The contrast in the TEM images near the regrowth interface could be due to the strain from lattice damage induced by the etching process, or precipitation due to the *p*-GaN growth. In order to identify the cause of precipitation, two more structures are studied where the etching is performed with a lower etching speeds, and un-doped GaN regrown over the etched *i*-GaN surface.

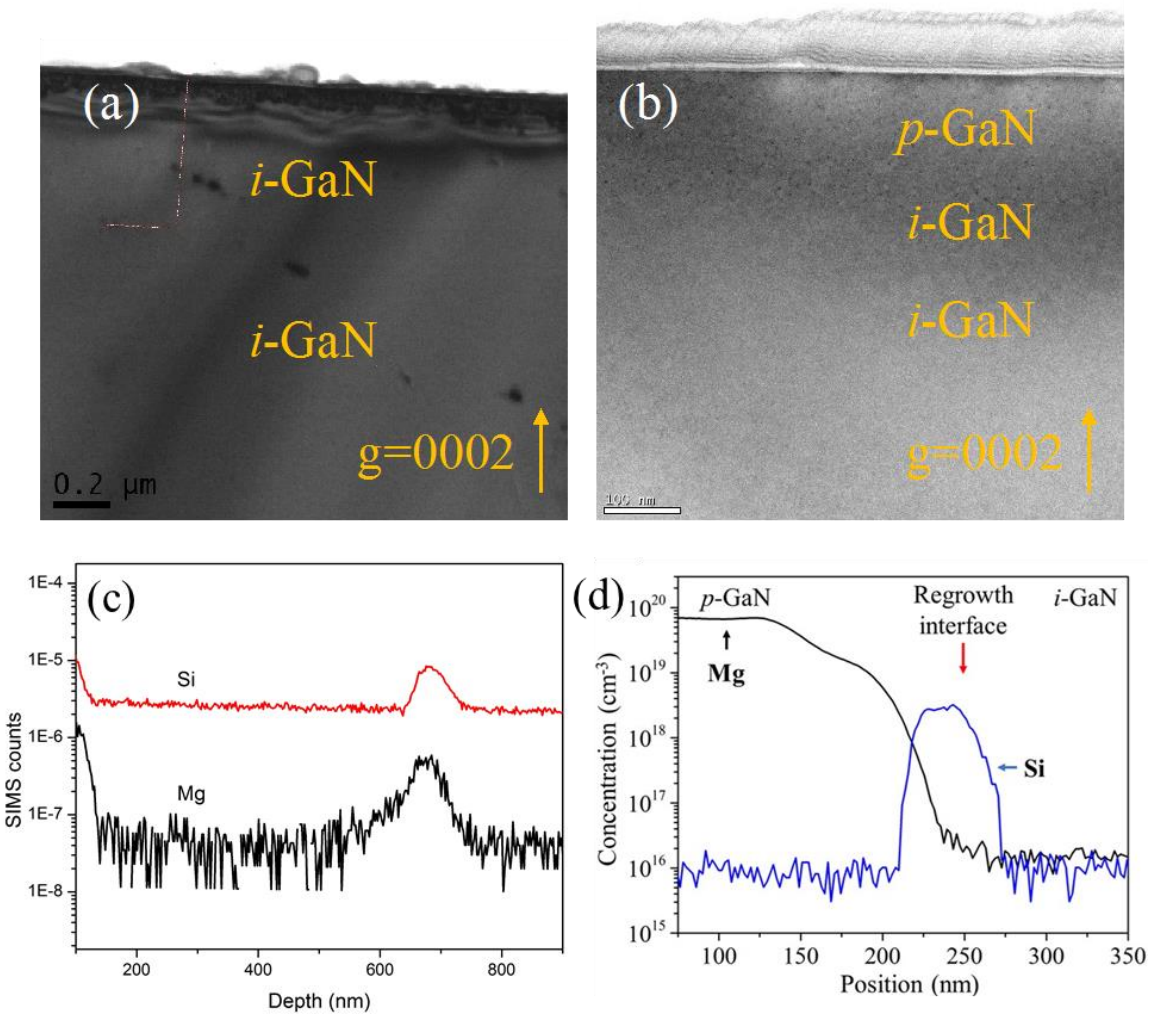

Figure 4.9. Two beam bright field images of (a) *i*-GaN regrown on etched *i*-GaN surface (b) *p*-GaN grown on etched *i*-GaN with a thin un-doped layer between them. (c), and (d) show the SIMS profiles of Mg, and Si corresponding to structures (a), and (b).

Precipitates at the regrowth interface can only be when the *p*-GaN is grown directly over the etched *i*-GaN surface. When un-doped GaN is grown directly over the etched GaN surface, no such precipitation is observed (Fig. 4.9).

The summary of precipitation observed in the samples is listed in the table below. Precipitates are only observed only when the *p*-GaN is grown directly over the top of etched *i*-GaN surface. Accumulation of Si can be seen at all the regrowth interfaces.

Etch rate	*p-i*	*i-i*
Fast	yes	No
Slow	-	No

4.4 Electrostatic potential analysis on GaN *p-n* junction

Figure 4.10 shows unwrapped phase from a hologram, and energy profile deduced from a simple GaN *p-n* junction. The structure was on a grown on 0.35° mis-cut GaN substrate in an MOCVD reactor. The doping concentration on either sides of the junction are Mg: $1.2x10^{19}$ cm^{-3}, and Si: $7.3x10^{18}cm^{-3}$. The electric fields in both the p-type, and the n-type layers are zero (constant electric potential). The measured depletion width of about 20 nm.

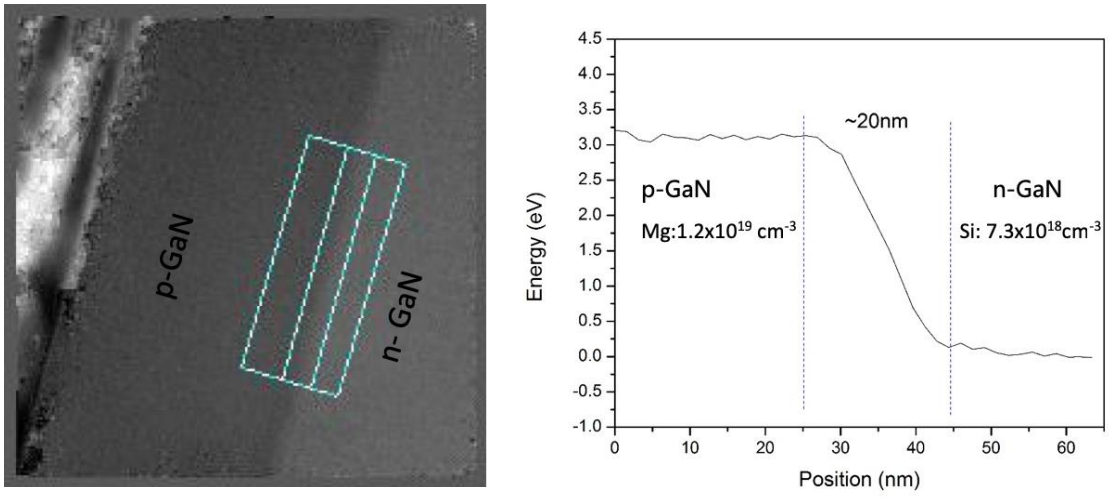

Figure 4.10. Electrostatic potential of a simple GaN *p-n* junction grown on 0.35° mis-cut GaN substrate.

The potential or energy profiles deduced from electron holography studies show the presence of charges, and their associated depletion widths in the structures. Such

analysis can be extended to *p*-*i*-*n* structures to understand the charges present at different interfaces.

4.5 Electrostatic potential analysis on GaN *p*-*i*-*n* junctions

There have been no known reports on potential profile analysis using electron holography of *p*-*i*-*n* GaN structures. In the section, the potential profiles of continuously grown *p*-*i*, and *i*-*n* interfaces are discussed. These can be useful for band structure simulations of GaN *p*-*i*-*n* structures. Electrostatic potential analysis on etched and regrown interfaces show presence of interface states, and possibility of highly doped junction near the interfaces. This information is crucial for understanding the regrowth interfaces and successfully incorporating dry etching techniques in the fabrication of GaN trench structures for various applications.

4.5.1 Un-interrupted GaN *p*-*i*-*n* structures

Figure 4.11(a) shows the potential profile at the *p*-*i* interface of a continuously grown *p*-*i*-*n* GaN structure with an *i*-GaN layer of thickness 10 μm. The schematic diagrams of the sample structures are shown as inset in this and in the following potential energy profiles. The potential in the *p*-GaN looks flat, indicating presence of no electric field due to high doping. In the *i*-GaN, we observe a constant electric field of magnitude ~ 0.003 MV/cm. Figure 4.11(b) shows the potential profile across a *p*-*i*-*n* GaN structure with an *i*-GaN layer of thickness 0.15 μm. A step in the potential profile is observed at the *i*-*n* interface with a flat potential in the *i*-GaN region directly above the *n*-GaN.

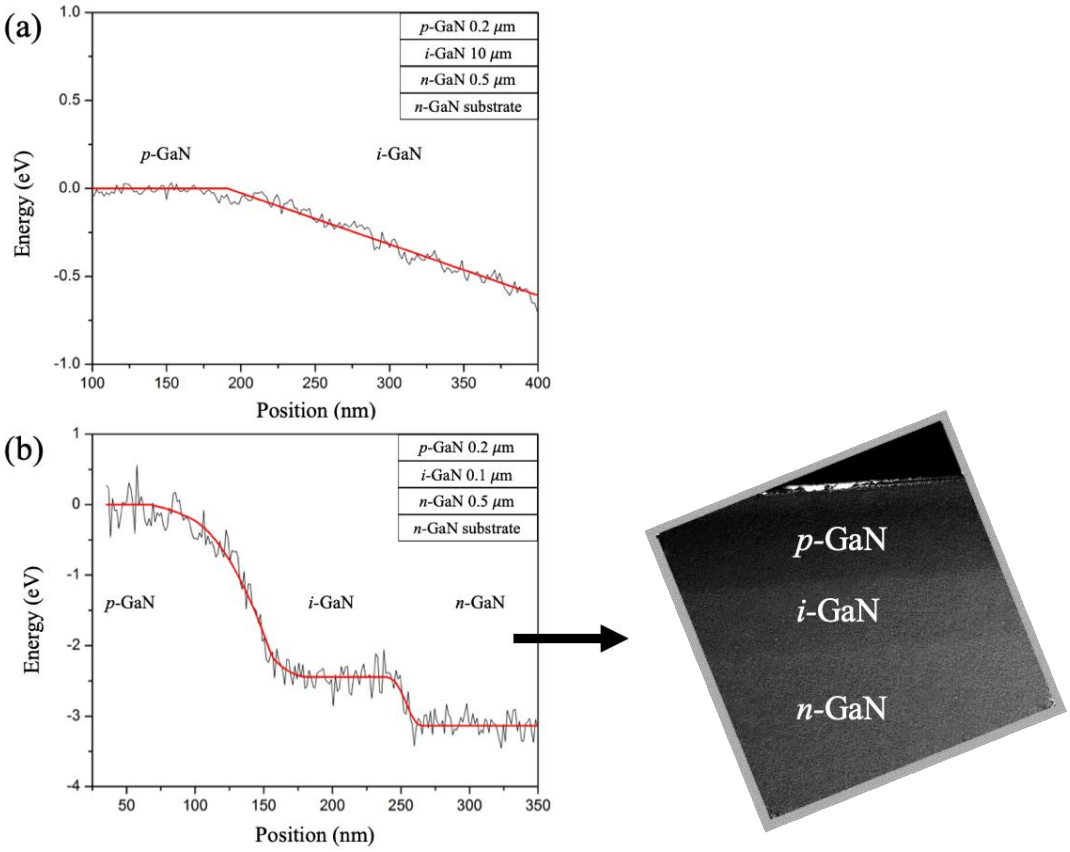

Figure 4.11. Electrostatic potential profile of continuously grown GaN *p*-*i*-*n* structure with *i*-GaN layer thickness of (a) 10 μm (b) 0.1 μm. Inset shows the epilayer structure. The phase image for the structure in 1(b) is shown here.

In the case of continuously grown *p*-*i*-*n* GaN structures, with a 10 μm thick *i*-GaN layer in Fig. 4.11(a), we observe a uniform electric field in the *i*-GaN layer near the *p*-*i* junction. This is due to the large depletion width in the *i*-GaN layer. Potential variation near the *i*-*n* interface may be understood as a result of relative concentrations of carbon and silicon impurities in the *i*-GaN (from SIMS measurements). It has been reported that if [C] > [Si] in GaN, the Fermi level is pinned midgap.[88] This is because the formation energy of C_{Ga} (donor) becomes equal to C_N (acceptor), effectively pinning the Fermi level as it

approaches midgap. Potential profile in the *i*-GaN layer follows the evolution of the Fermi level inside the band gap.

4.5.2 Etched and regrown GaN *p-i-n* structures

The case for etch-and-regrowth is very different from the continuously grown structures. Etch-and-regrowth involves several steps: a growth interruption, removal from the growth chamber, transfer to an etching chamber, the etching process itself, and surface treatment to remove any possible damage and contamination, and reinsertion into the MOCVD chamber for the growth of subsequent layers. SIMS measurements on etched-and-regrown structures show an accumulation of ~ 10^{18} -10^{19} cm^{-3} of Si and O impurities at the regrowth interface, as in Fig. 4.13(b). Such anomalous impurity accumulation has been reported earlier.[89,90] In one particular study, impurity accumulation has been investigated for a variety of growth interruptions, including retaining the wafer in the growth chamber, exposure to air, and etching the surface prior to regrowth. In all the cases, impurity accumulation in the range of 10^{17} - 10^{19} cm^{-3} of Si and O was reported at the regrowth interfaces.[91] The origin of this impurity accumulation is not well understood. Given that a simple growth interruption can result in such accumulation, we can rule out the possibility of etching being the only reason for the presence of impurities. It is possible that impurities on the walls of the MOCVD chamber condense onto the growth surface during the interruption Also, SIMS profiles of Mg (Fig. 4.13(b)) near the etched and regrown interfaces suggest Mg gettering, which is likely associated with the precipitates at the etched interface typically observed by TEM. The presence of Si impurities at the regrowth interface may be influencing the Mg incorporation which results in such precipitation. Perhaps, investigating the impurity accumulation during growth interruptions

with AlN or SiC coated MOCVD chamber can be interesting. Also, the etching process itself introduces deep donors in the sub-surface layers, which may be pinning the Fermi levels near the regrowth interface.

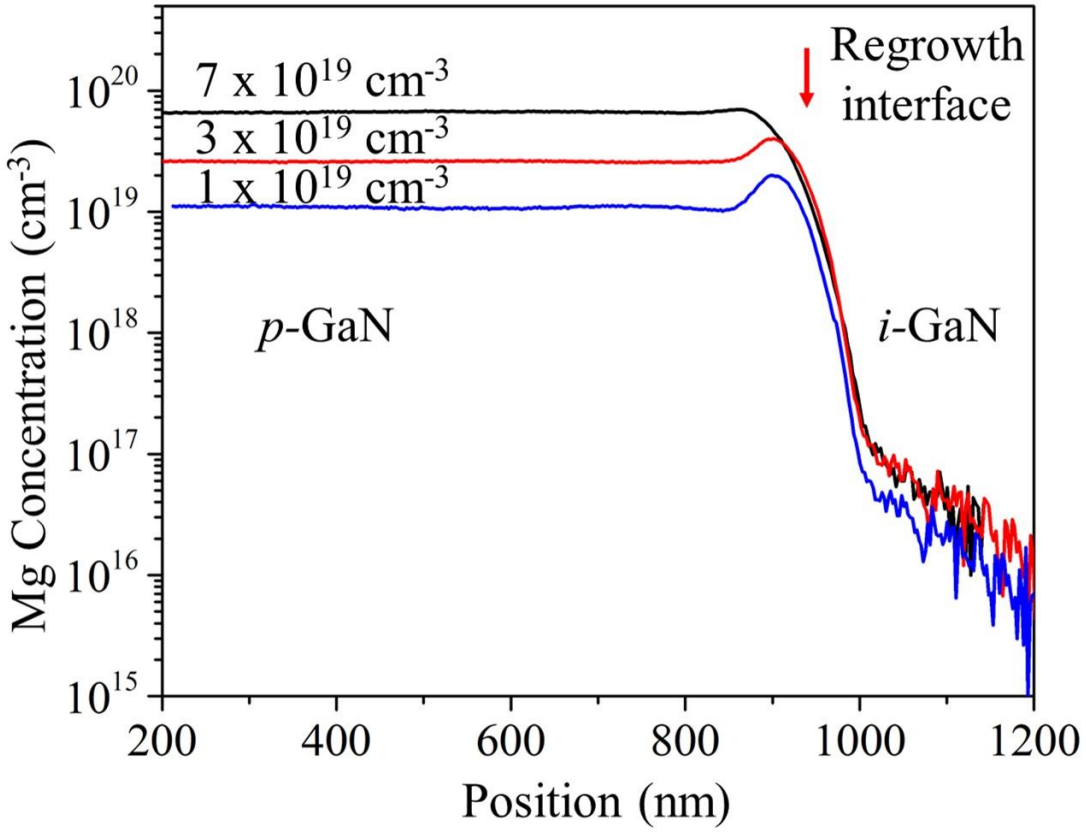

Figure 4.12. SIMS profiles of Mg at the *p*-*i* interface of etched-and-regrown GaN *p*-*i*-*n* structures corresponding to the *p*-GaN layers with Mg concentrations of 1, 3, and 7x10^{19} cm^{-3}. Notice peak in the Mg concentration indicating Mg accumulation at the regrowth interface.

4.5.3 Etched and regrown GaN *p-i* junction without an insertion layer

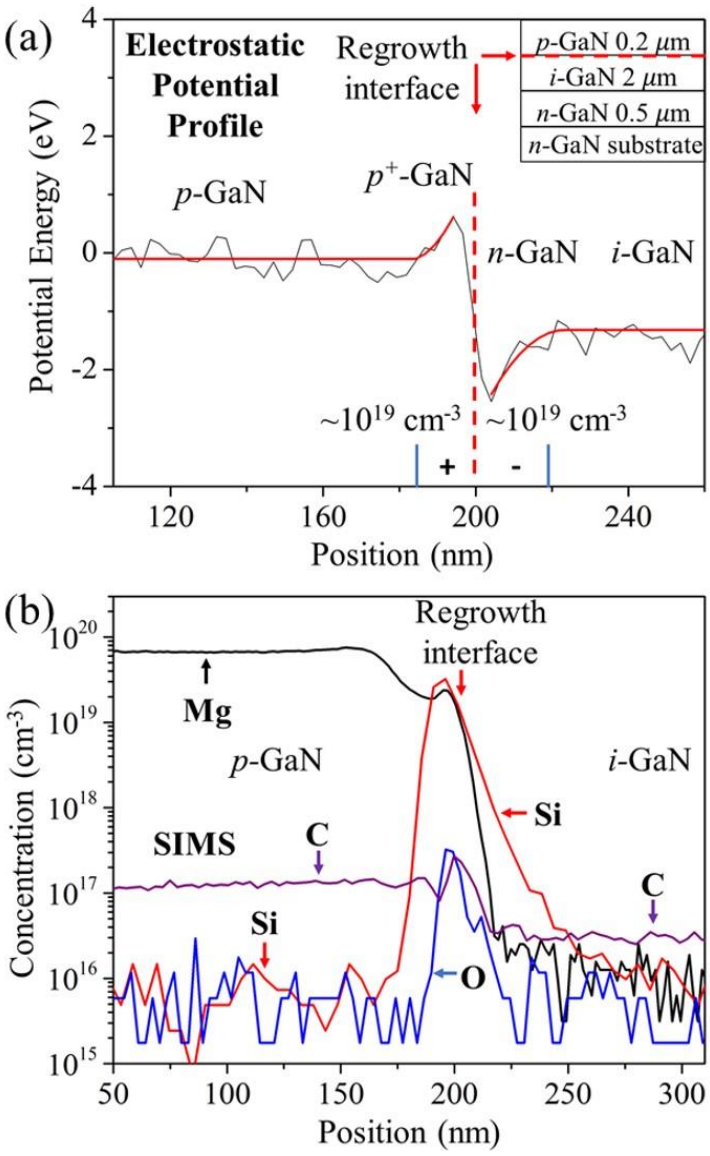

Figure 4.13. (a) Electrostatic potential profile indicating accumulation of negative charge at the *i*-GaN and positive charge at the *p*-GaN regions next to the *p-i* interface. Estimated charge densities near the regrowth interfaces are indicated on the image. (b) SIMS profiles of Mg, Si, C, and O at the *p-i* interface of an etched-and-regrown GaN *p-i-n* structure.

Figure 4.13(a) shows the potential energy profile at the *p-i* junction with an etched interface between the *p*-GaN and the *i*-GaN, with features that indicate ~ 10^{19} cm^{-3}

electronic charge accumulation on each side of the interface. Figure 4.13(b) is a SIMS depth profile showing that the regrowth interface region has an overlap of Mg, Si, C, and O with peak concentrations of ~2 x 10^{19} cm^{-3}, ~3 x 10^{19} cm^{-3}, and ~3 x 10^{17} cm^{-3}, respectively. This indicates that the introduction of an ICP etching step causes accumulation of Si and O impurities at the etched-and-regrown interface. Figure 4.12 shows SIMS profiles for Mg in *p*-*i* junctions with an etched interface for different Mg concentrations in the *p*-GaN films. Each profile shows a local maximum in the Mg concentration at the etched interface, which indicate some form of Mg gettering. Cross-section TEM images exhibit precipitates at *p*-*i* junctions with etched interface for all Mg concentrations (see supplementary information), which are probably associated with the Mg local maxima in the SIMS profiles. The broadening of impurity profiles near the interfaces is associated with the crater roughness, and cascade mixing during the SIMS sputtering process.[45]

We observe an anomalous upward curvature in the energy profile on the *p*-GaN side of the regrowth interface. Also, it is accompanied by a downward curvature on the *i*-GaN side of the regrowth interface. The downward curvature can be due to the highly *n*-type behavior resulting from the excessive donors, and midgap states introduced by the etching damage. The interpretation of the upward curvature is not so intuitive. In order to make sure that the measurement is correct, and the upward curvature is not an artefact, electron holograms are recorder with out of plane tilt. This makes sure that the observed curvatures in the energy profiles are not due to the diffraction effect, and represents real charge distribution in the sample.

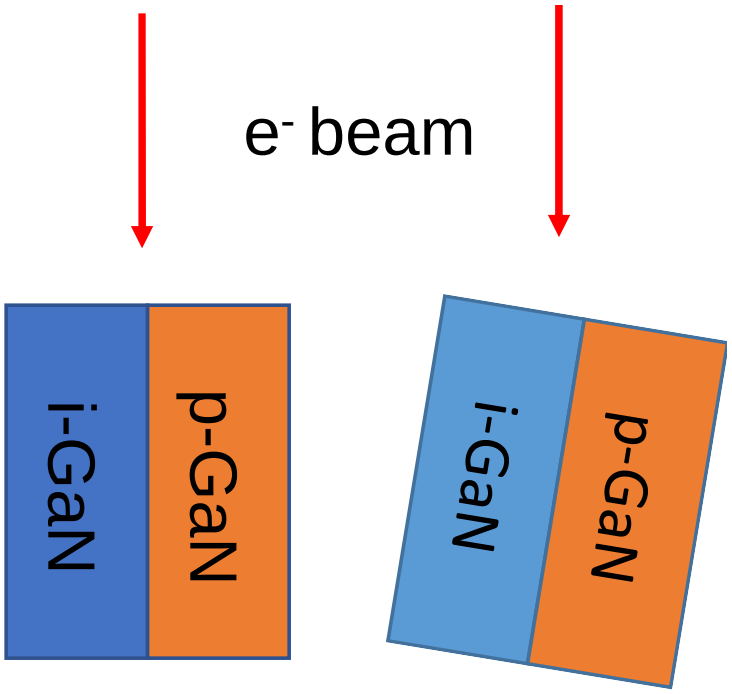

Figure 4.14. Schematic diagram showing in-plane and out of plane tilt of the interface with respect to the electron beam.

Typically, interfaces are kept edge-on when acquiring electron holograms. This ensures that the phase shift signal obtained is not smeared out due to overlap. In our particular case, the explanation for the potential profile obtained is not intuitive. Figure 4.15 and Fig. 4.16 shows potential profiles obtained from holograms with out-of-plane tilting of about ~2^0, both towards and away from the c-direction.

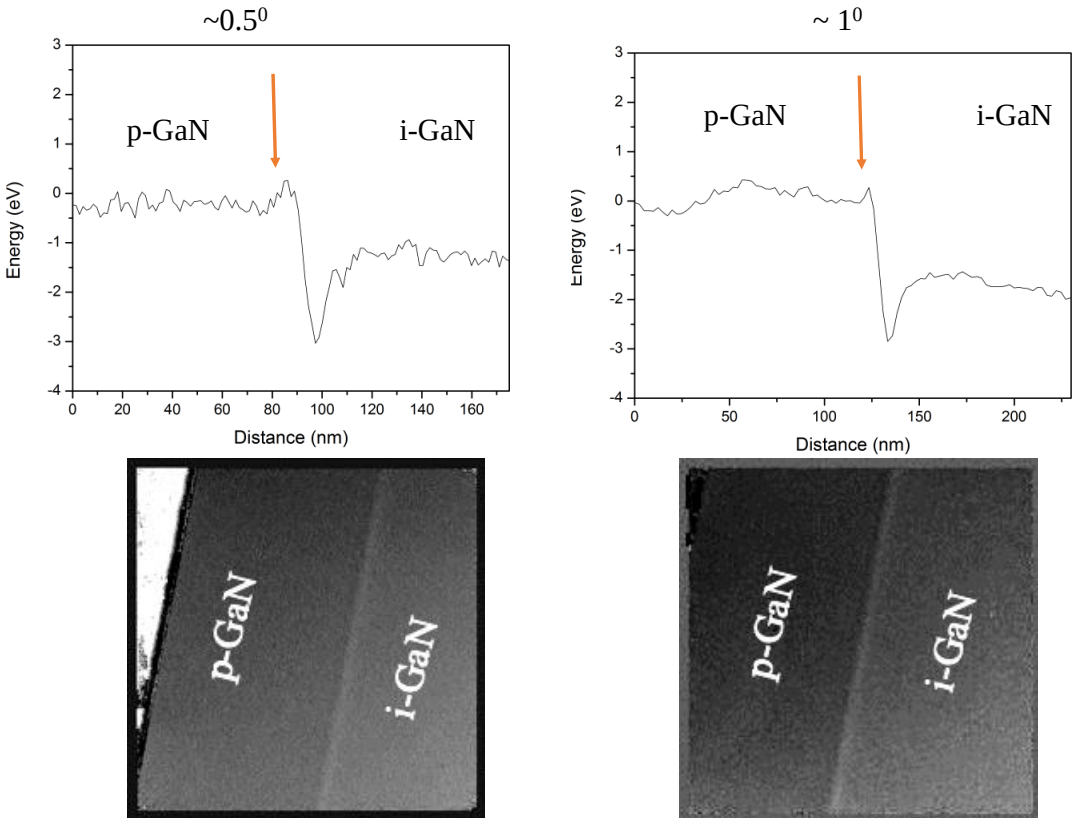

Figure 4.15. Energy profiles of a *p*-GaN grown directly over etched *i*-GaN surface with out of plane tilt of ~0.5^0 and ~1^0 toward c-axis. Extracted phase for each of the energy profiles are shown, where a bright band can be cleared observed at the interface.

With a slight out of plane tilting, the upward curvature in the energy profile on the *p*-GaN side of the regrowth interface can still be seen. This suggests that the observed signal is real and not due to some diffraction effects. Given the diffraction effects are ruled out, the other possibility could be a highly doped *p*-GaN region close to the regrowth interface.

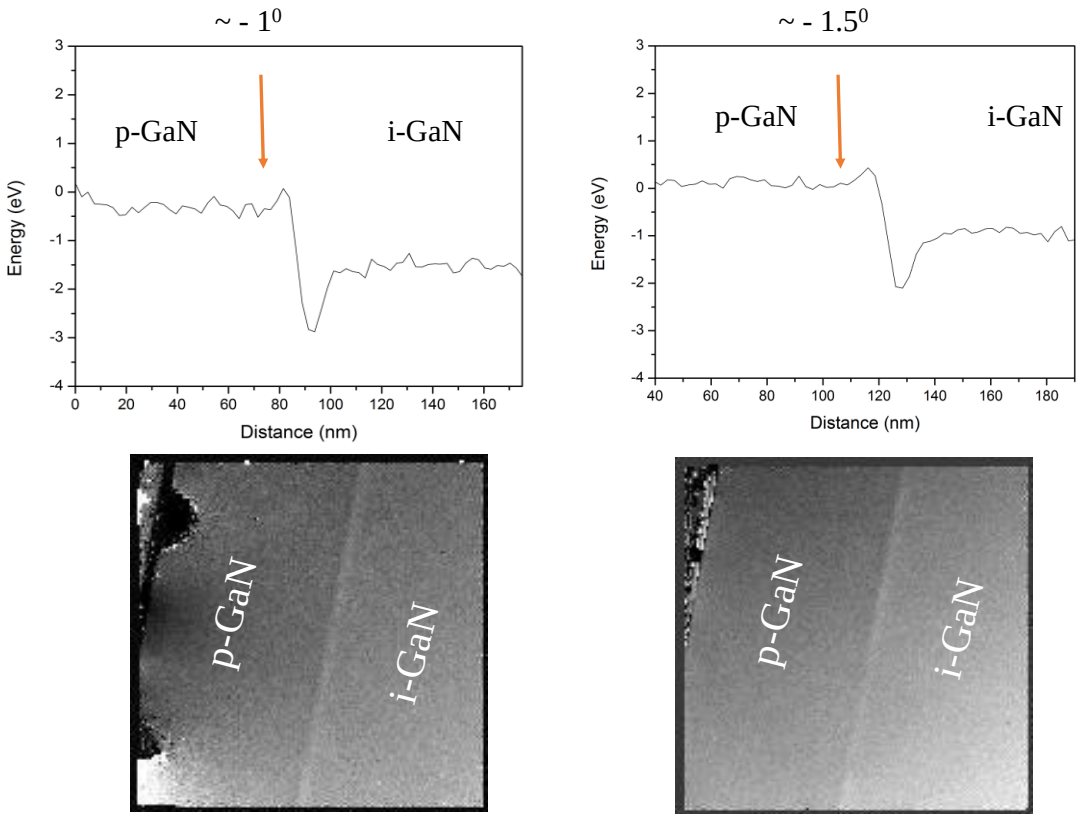

Figure 4.16. Potential energy profiles of a *p*-GaN grown directly over etched *i*-GaN surface with out of plane tilt of ~0.5^0 and ~1^0 away from c-axis. Extracted phase for each of the energy profiles are shown, where a bright band can be cleared observed at the interface.

SIMS analysis shows that the *p*-GaN near the interface region has Mg, Si, and O. The downward curvature of the potential profile on the *i*-GaN side of the interface is related to the presence of significant amounts of Si and O, which may act as donors on the *i*-GaN side of the regrowth interface, resulting in highly *n*-type GaN. The overlap of Mg, Si, and O impurities could lead to a case where *p*-GaN is co-doped close to the etched interface region. It has previously been observed that co-doping Mg doped GaN with Si or O can lead to an enhancement in hole concentration by up to two orders of magnitude.[92–95] Such increased hole concentration would result in an upward curvature in the potential profile

on the *p*-GaN side of the etched interface. Co-doping is a complex phenomenon where multiple factors could be playing a role in enhancement of hole concentration of the *p*-GaN film. The formation of acceptor-donor-acceptor (ADA) complexes has been proposed to result in increased hole concentrations due to lower ionization energies for such complexes.[92] Predictions for hole concentrations using the ADA complex model matches very well with the experimental data for both Si and O co-doping. Thus the upward curvature on the *p*-GaN side can interpreted as a highly doped *p*-region due to possible co-doping. The presence of donor impurities (Si, O), and mid-gap states introduced by the etching of GaN could be pinning the Fermi level on the *i*-GaN side of the regrowth interface. Thus, the etch-and-regrowth interface region behaves like a highly doped *p*-*n* junction. This explains the temperature independent I-V characteristics of these diodes in reverse bias, suggesting tunneling as the reverse transport mechanism. Also, in one of the recent studies on doping profiles in GaN tunnel junctions, it was found that the overlap of Mg and Si at the interface helped obtain low resistive tunnel junctions.[96] Such tunnel junction behavior would result in high reverse leakage currents, which is undesirable for power applications.

4.5.4 Etched and regrown GaN *p-i* junction with an insertion layer

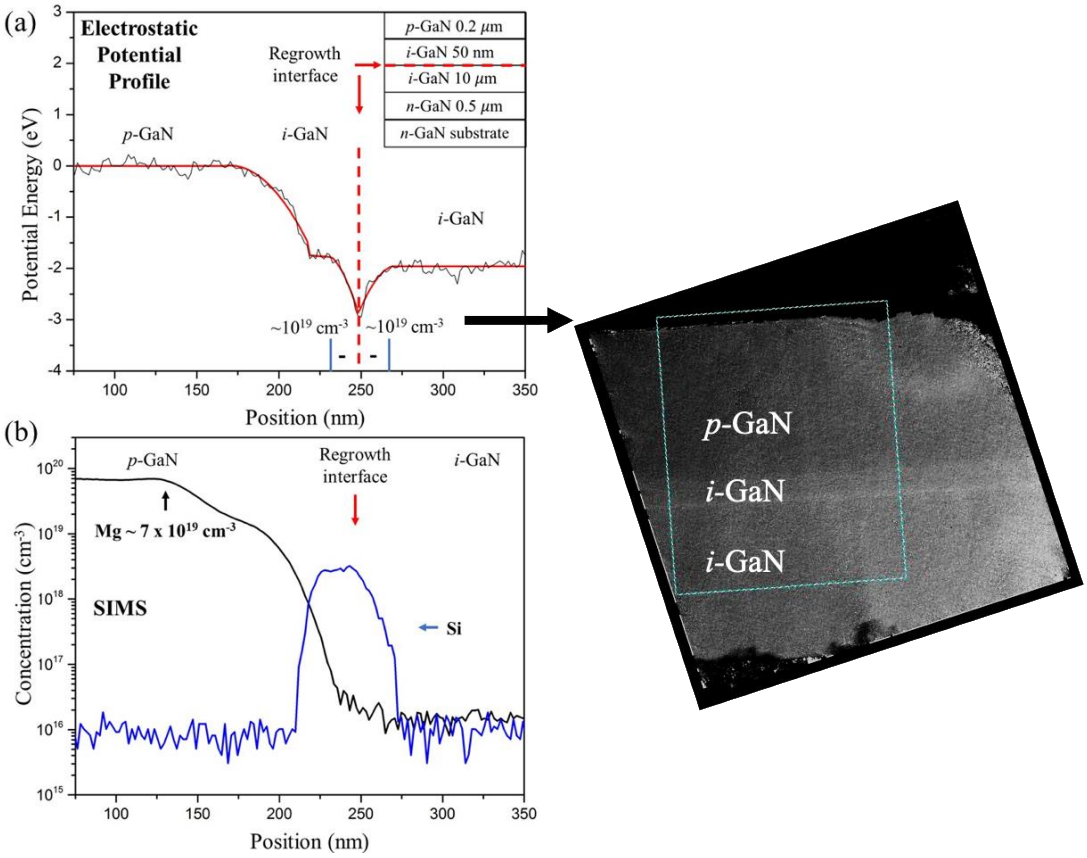

Figure 4.17. Etched-and-regrown GaN *p-i-n* structure with 50 nm undoped GaN insertion layer. Inset shows the epi-layer structure. (a) Electrostatic potential profile of the *p-i* interface. Charges near the regrowth interfaces are indicated. (b) SIMS profiles of Mg and Si. Corresponding phase image is shown here.

Figure 4.17(a) shows the potential profile across a *p-i* junction that contains an un-doped GaN layer of thickness 50 nm deposited on an etched *i*-GaN layer before the growth of *p*-GaN. The dip in potential profile at the regrown interface indicates presence of a positive sheet charge, surrounded by negative charged regions, which are indicated in the Fig. 4.17(a). The Si accumulation due to the regrowth process is shifted from the Mg, compared to the sample in Fig. 4.13(a), due to the introduction of 50 nm intermediate un-

doped layer. The donor impurities, and the mid-gap states in the etched sub-surface layers could be pinning the Fermi level, and thus introducing a positive sheet charge, which reflected in the energy profile (Fig. 4.17(b)). C-V measurements on similar structures indicate presence of ~10^{18} – 10^{19} cm^{-3} positive charges at the regrowth interface. The 50 nm un-doped GaN layer recovers into being a true *i*-GaN close to the *p*-*i* junction. Thus the addition of an un-doped layer on top of the etched surface helps move the defective regrowth interface from the *p*-*i* junction, which prevents the formation of highly doped *p*-*n* junction. The leakage currents measured on the diodes (5 nA at 600 V) with the insertion layer were close to that of as-grown *p*-*i*-*n* structures (1 nA at 600 V).

4.6 Conclusion

In summary, electrostatic potential profiles across continuously grown, and etch-and-regrown diodes were mapped and analyzed. Regrowth interfaces incorporate high levels Si and O impurities as determined from SIMS analysis. Regrowth of *p*-GaN over etched surface results in highly doped *p*-*n* junction behaving like a tunnel junction. Introduction of a thin un-doped layer helps consuming the impurities, which prevents formation of highly doped *p*-*n* junction. In the design of power electronics, care should be taken to consider these effects.

5. CONCLUSIONS AND OUTLOOK

5.1 Dopant profiling using SEM

In summary, dopant profiling in a SEM is used to study structures for power applications. Cross-sectional dopant profiles can be obtained using this technique which can very useful for understanding the layer designs. These profiles can be used as parameter for device simulations. Best conditions to obtain the profiles has been explored. Using specimen itself as a detector to record the specimen currents can potentially be used for quantitative dopant profiling.

An interesting avenue of research could be looking into the energy distribution of the secondary electrons emitted for differently doped GaN films. In one of the recent studies it has been shown that the energy distribution is relatively unaffected by the surface contamination. The study of dependence of energy distribution of SE's on the doping level in the material can improve the understanding of the SE emission from the surfaces. Scanning Auger Electron Microscopy with FEG source can be an ideal equipment to perform such studies. If the energy distribution of SE's and their dependence on doping levels can be understood well, it can have a huge impact on dopant profiling in nanostructures. These applications can be extended to all the semiconductor systems. Also, heterojunction may be interesting for these studies as the energy distribution of SE's should depend on the material and their doping levels.

During the course of this work, the specimen current was recorded on a Nova nanolab 200 FIB microscope. It did not have the capability of recording specimen currents in a raster pattern. Possibility of serial recoding of specimen current as the beam raster on the surface can be very helpful in order to profile the dopants in a cross section of a device

with lateral and vertical junctions. Also, the specimen current recorded is affected by the surface preparation methods.

One of the unresolved areas in the dopant profiling using SEM is the effect of beam current on the observed image contrast. It appears that the contrast reversals between the *p*-layer and *n*-layer in a *p*-*n* junction occurs at lower voltages. With higher beam currents, the voltage at which such a reversal occurs is higher i.e. the contrast reversal phenomenon gets severe with the increasing beam currents. This is illustrated in the figure below. Understanding the exact role of beam current can be an interesting area of research.

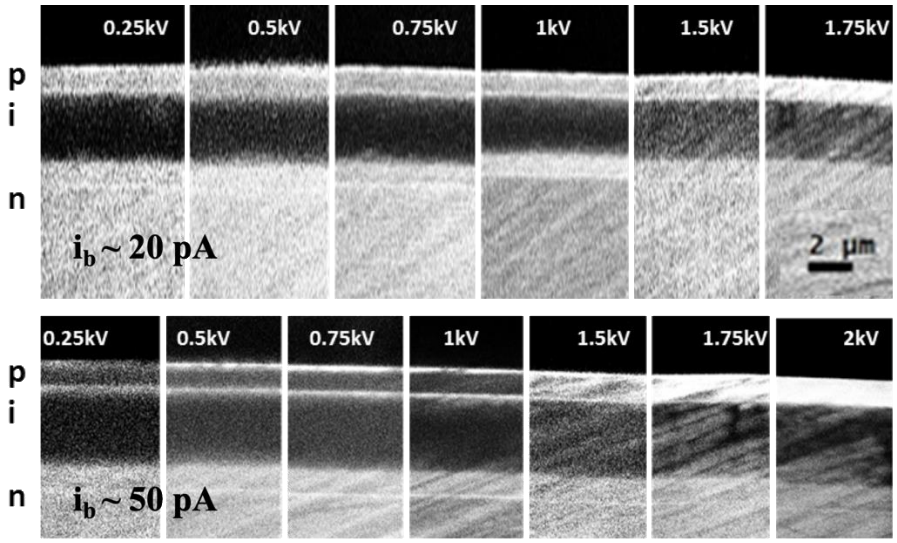

Figure 5.1 Effect of beam current on the contrast reversal between *p*-layer and *n*-layer.

All the measurements in this study are made by making an electrical contact to each layer of interest using a silver paste. Under right conditions, material does not appear to charge. However, it can be interesting to check the effect of intentional Ohmic, and Schottky contacts to the layer of interest on the electron yields.

5.2 Etched and regrown GaN *p-i-n* diodes

There is a lot of room for improvement in the case of etched and regrown GaN *p-i-n* diodes. The idea for studying the etched and regrown devices is to understand the interface in order to effectively implement them in the device structures. The major problem arises when there is a growth interruption for etching purposes. This and the etching in itself introduces impurities at the interfaces. These impurities lead to diodes with lower breakdown voltages and higher leakage currents.

Important factor to be considered is the etch damage itself. The deep donors introduced by the etching process is not well understood. The surface stoichiometric studies also show the Ga/N ratio is more than one. Atomic layer etching (ALE) can be employed to remove top few nm's of etched surface, which ensures removal of sub-surface damage induced by the plasma etching. After ALE, air exposure may oxidize the surface, which can be removed with acid treatment. Also, the stoichiometry of the sample can be improved by thermal annealing in N_2 environment. This may be achieved during the re-insertion of etched surface into the MOCVD chamber. Wet etching of GaN using KOH chemistry has been reported to introduce less non-radiative recombination centers on the etched surface. A combination of dry, and wet etching of GaN can be a great way to maintain the throughput as well as reduce the etch induced damage at the same time.[97]

Current etching equipment available is designed to hold 4" wafers. This results in use of a foreign substrate for etching of GaN wafers. Commercially available GaN wafers are 2" in size during the time of this research. Thus, using carrier wafers similar to that of the material being etched, may eliminate a possible source of contamination.

Currently the surface is oxidized, and then treated with acid to remove the contaminants. It is then reintroduced in the MOCVD chamber for regrowth. There can be some contamination during the handling process. This may be reduced by designing an interconnected system, where the whole process is carried out in vacuum. This can be a solution for high throughput fabrication sites given the cost of system. Chamber wall coatings may also be significantly affecting the impurity accumulation at the regrowth interfaces.

REFERENCES

1. I. C. Kizilyalli, Y. A. Xu, E. Carlson, J. Manser, and D. W. Cunningham,in *2017 IEEE 5th Workshop on Wide Bandgap Power Devices and Applications (WiPDA)* (IEEE, Albuquerque, NM, 2017), pp. 417–417.

2. T. D. Heidel and P. Gradzki,in *2014 IEEE International Electron Devices Meeting* (IEEE, San Francisco, CA, USA, 2014), pp. 2.7.1-2.7.4.

3. Srabanti Chowdhury,AlGaN/GaN CAVETs for High Power Switching Application, UCSB, 2010.

4. G. Lo Calzo, G. Vakil, B. Mecrow, S. Lambert, T. Cox, C. Gerada, M. Johnson, and R. Abebe, "*Integrated motor drives: state of the art and future trends*," IET Electric Power Applications **10**, 757 (2016).

5. D. Ji, M. A. Laurent, A. Agarwal, W. Li, S. Mandal, S. Keller, and S. Chowdhury, "*Normally OFF Trench CAVET With Active Mg-Doped GaN as Current Blocking Layer*," IEEE Transactions on Electron Devices **64**, 805 (2017).

6. B. J. Baliga,Fundamentals of Power Semiconductor Devices (Springer, New York, NY, 2008).

7. S. Chowdhury and U. K. Mishra, "*Lateral and Vertical Transistors Using the AlGaN/GaN Heterostructure*," IEEE Transactions on Electron Devices **60**, 3060 (2013).

8. I. C. Kizilyalli, A. P. Edwards, O. Aktas, T. Prunty, and D. Bour, "*Vertical Power p-n Diodes Based on Bulk GaN*," IEEE Transactions on Electron Devices **62**, 414 (2015).

9. F. A. Ponce and D. P. Bour, "*Nitride-based semiconductors for blue and green light-emitting devices*," Nature **386**, 351 (1997).

10. Isik C. Kizilyalli, A. P. Edwards, O. Aktas, T. Prunty, and D. Bour, "*Vertical Power p-n Diodes Based on Bulk GaN*," IEEE Transactions on Electron Devices **62**, 414 (2015).

11. The Blue Laser Diode The Complete Story. (Springer Verlag, 2010).

12. H. Liu, H. Fu, K. Fu, S. R. Alugubelli, P.-Y. Su, Y. Zhao, and F. A. Ponce, "*Non-uniform Mg distribution in GaN epilayers grown on mesa structures for applications in GaN power electronics*," Applied Physics Letters **114**, 082102 (2019).

13. K. Fu, H. Fu, H. Liu, S. R. Alugubelli, T.-H. Yang, X. Huang, H. Chen, I. Baranowski, J. Montes, F. A. Ponce, and Y. Zhao, "*Investigation of GaN-on-GaN vertical* p - n *diode with regrown* p *-GaN by metalorganic chemical vapor deposition*," Applied Physics Letters **113**, 233502 (2018).

14. S. J. Pearton, C. B. Vartuli, J. C. Zolper, C. Yuan, and R. A. Stall, "*Ion implantation doping and isolation of GaN,*" Applied Physics Letters **67**, 1435 (1995).

15. P. D. Nellist, M. F. Chisholm, N. Dellby, O. L. Krivanek, M. F. Murfitt, Z. S. Szilagyi, A. R. Lupini, A. Borisevich, W. H. S. Jr, and S. J. Pennycook, "*Direct Sub-Angstrom Imaging of a Crystal Lattice,*" Science **305,** 1741 (2004).

16. L. Reimer, Scanning Electron Microscopy: Physics of Image Formation and Microanalysis (2010).

17. D. Liljequist, "*Simplified models for the Monte Carlo simulation of energy istributions of keV electrons transmitted or back-scattered in various solids,*" J. Phys. D: Appl. Phys. **11** 839 (1978).

18. K. Kanaya, S. Ono, and F. Ishigaki, "*Secondary electron emission from insulators,*" J. Phys. D: Appl. Phys. **11** 2425 (1978).

19. R. E. Simon and B. F. Williams, "*Secondary-Electron Emission,*" IEEE Trans. on Nuc. Sci. **15,** 3 (1968).

20. N. R. Rajopadhye, V. A. Joglekar, V. N. Bhoraskar, and S. V. Bhoraskar, "*Ion secondary electron emission from $A1_2O_3$ and MgO films,*" Sol. Stat. Comm. **60,** 675 (1986).

21. A. Shih, J. Yater, C. Hor, and R. Abrams, "*Secondary electron emission studies,*" Appl. Surf. Sci. **111**, 251 (1997).

22. G. K. L. Marx, "*Probing depth of threshold photoemission electron microscopy,*" Appl. Phys. Lett. **83**, 2925 (2003).

23. W. A. Gutierrez, H. D. Pommerrenig, and S. L. Holt, "*Secondary electron emission from GaAs,*" Appl. Phys. Lett. **21**, 249 (1972).

24. H. Seiler, "*Secondary electron emission in the scanning electron microscope,*" Journal of Applied Physics **54**, R1 (1983).

25. L. Reimer and C. Tollkamp, "*Measuring the backscattering coefficient and secondary electron yield inside a scanning electron microscope,*" Scanning **3**, 35 (1980).

26. R. U. Martinelli and D. G. Fisher, "*The application of semiconductors with negative electron affinity surfaces to electron emission devices,*" Proc. IEEE **62**, 1339 (1974).

27. J. Goldstein,Scanning Electron Microscopy and X-Ray Microanalysis, 4th ed. Springer (2017).

28. B. Fultz and J. Howe, "*Transmission Electron Microscopy and Diffractometry of Materials,*" Springer (2012).

29. A. Howie and M.J. Whelan, "*Diffraction contrast of electron microscope images of crystal lattice defects,*" Proc. R. Soc. A 263, 217 (1961).

30. D. Gabor, "*A New Microscopic Principle,*" Nature **161**, 777 (1948).

31. W. J. de Ruijter and J. K. Weiss, "*Methods to measure properties of slow-scan CCD cameras for electron detection,*" Review of Scientific Instruments **63**, 4314 (1992).

32. J. M. Cowley, "*Twenty forms of electron holography,*" Ultramicroscopy **41**, 335 (1992).

33. M. R. McCartney and D. J. Smith, "*Electron Holography: Phase Imaging with Nanometer Resolution,*" Annual Review of Materials Research **37**, 729 (2007).

34. F. A. Ponce, "*Electrostatic energy profiles at nanometer-scale in group III nitride semiconductors using electron holography,*" Annalen der Physik **523**, 75 (2011).

35. G. F. Missiroli, G. Pozzi, and U. Valdre, "*Electron interferometry and interference electron microscopy,*" J. Phys. E: Sci. Instrum. **14**, 649 (1981).

36. M. Gajdardziska-Josifovska and M. R. McCartney, "*Elimination of thickness dependence from medium resolution electron holograms,*" Ultramicroscopy **53**, 291 (1994).

37. M. R. McCartney and M. Gajdardziska-Josifovska, "*Absolute measurement of normalized thickness, t / A, from off-axis electron holography,*" Ultramicroscopy **53**, 283 (1994).

38. J. W. Chen, G. Matteucci, A. Migliori, G. F. Missiroli, E. Nichelatti, G. Pozzi, and M. Vanzi, "*Mapping of microelectrostatic fields by means of electron holography: Theoretical and experimental results,*" Phys. Rev. A **40**, 3136 (1989).

39. A. Fukuhara, K. Shinagawa, A. Tonomura, and H. Fujiwara, "*Electron holography and magnetic specimens,*" Phys. Rev. B **27**, 1839 (1983).

40. F. A. Stevie, "*Secondary Ion Mass Spectrometry: Applications for Depth Profiling and Surface Characterization*" Momentum Press (2016).

41. V. E. Krohn, "*Emission of Negative Ions from Metal Surfaces Bombarded by Positive Cesium Ions,*" Journal of Applied Physics **33**, 3523 (1962).

42. P. Williams and C. A. Evans, "*Anomalous enhancement of negative sputtered ion emission by oxygen,*" Surface Science **78**, 324 (1978).

43. S. A. Schwarz,in *Encyclopedia of Material : Science and Technology* (2001), pp. 8283–8290.

44. https://www.eag.com/resources/tutorials/sims-tutorial-instrumentation/.

45. C. W. Magee and R. E. Honig, "*Depth profiling by SIMS?depth resolution, dynamic range and sensitivity*," Surf. Interface Anal. **4**, 35 (1982).

46. P. K. Chu, Y. Gao, and J. W. Erickson, "*Characterization of III nitride materials and devices by secondary ion mass spectrometry*," J. Vac. Sci. Technol. B **16**, 8 (1998).

47. P. Jörchel, P. Helm, F. Brunner, A. Thies, O. Krüger, and M. Weyers, "*Quantification of matrix and impurity elements in $Al_xGa_{1-x}N$ compounds by secondary ion mass spectrometry*," J. Vac. Sci. Technol. B **34**, 6 (2016).

48. M. Tapajna, A. Vincze, P. Noga, J. Dobrovodsky, A. Svagatova, S. Hasenohr, D. Gregusova, and J. Kuzmik, " Determination of secondary-ions yield in SIMS depth profiling of Si, Mg, and C ions implanted GaN epitaxial layers" *12th International Conference on Advanced Semiconductor Devices and Microsystems* IEEE pp. 1–4 (2018).

49. P. H. Chi, D. S. Simons, J. M. McKinley, F. A. Stevie, and C. N. Granger, "*High precision measurements of arsenic and phosphorous implantation dose in silicon by secondary ion mass spectrometry*," Journal of Vacuum Science & Technology A: Vacuum, Surfaces, and Films **20**, 688 (2002).

50. T.H.P. Chang and W.C. Nixon, "*Electron beam induced potential contrast on unbiased planar transistors*," Sol. Stat. Elec. **10**, 701 (1967).

51. D. D. Perovic, M. R. Castell, A. Howie, C. Lavoie, T. Tiedje, and J. S. W. Cole, "*Field-emission SEM imaging of compositional and doping layer semiconductor superlattices*," Ultramicroscopy **58**, 104 (1995).

52. D. D. Perovic, G. C. Weatherly, R. F. Egerton, D. C. Houghton, and T. E. Jackman, "*On the electron microscope contrast of doped semiconductor layers*," Philosophical Magazine A **63**, 757 (1991).

53. I. Volotsenko, M. Molotskii, Z. Barkay, J. Marczewski, P. Grabiec, B. Jaroszewicz, G. Meshulam, E. Grunbaum, and Y. Rosenwaks, "*Secondary electron doping contrast: Theory based on scanning electron microscope and Kelvin probe force microscopy measurements*," Journal of Applied Physics **107**, 014510 (2010).

54. A. K. W. Chee, "*Quantitative Dopant Profiling by Energy Filtering in the Scanning Electron Microscope*," IEEE Transactions on Device and Materials Reliability **16**, 138 (2016).

55. C. P. Sealy, M. R. Castell, and P. R. Wilshaw, "*Mechanism for secondary electron dopant contrast in the SEM*," Journal of Electron Microscopy **49**, 311 (2000).

56. D. Venables, "*Secondary electron imaging as a two-dimensional dopant profiling technique: Review and update,*" Journal of Vacuum Science & Technology B: Microelectronics and Nanometer Structures **16**, 362 (1998).

57. J. Cazaux, "*From the physics of secondary electron emission to image contrasts in scanning electron microscopy,*" Journal of Electron Microscopy **61**, 261 (2012).

58. A. K. W. Chee, "*Quantitative Dopant Profiling by Energy Filtering in the Scanning Electron Microscope,*" IEEE Transactions on Device and Materials Reliability **16**, 138 (2016).

59. J. R. Dennison, A. Sim, and C. D. Thomson, "*Evolution of the Electron Yield Curves of Insulators as a Function of Impinging Electron Fluence and Energy,*" IEEE Transactions on Plasma Science **34**, 2204 (2006).

60. D. C. Joy, "*Control of charging in low-voltage SEM,*" Scanning **11**, 1 (1989).

61. M. El-Gomati, F. Zaggout, H. Jayacody, S. Tear, and K. Wilson, "*Why is it possible to detect doped regions of semiconductors in low voltage SEM: a review and update,*" Surface and Interface Analysis **37**, 901 (2005).

62. A. K. W. Chee, "*Enhancing doping contrast and optimising quantification in the scanning electron microscope by surface treatment and Fermi level pinning,*" Scientific Reports **8** (2018).

63. J. E. Yater, J. L. Shaw, K. L. Jensen, D. W. Feldman, N. Moody, and P. G. O'Shea,in *2006 IEEE International Vacuum Electronics Conference Held Jointly with 2006 IEEE International Vacuum Electron Sources* (IEEE, Monterey, CA, USA, 2006), pp. 433–434.

64. G. F. Dionne, "*Origin of secondary-electron-emission yield-curve parameters,*" Journal of Applied Physics **46**, 3347 (1975).

65. A. Shih, J. Yater, P. Pehrsson, J. Butler, C. Hor, and R. Abrams, "*Secondary electron emission from diamond surfaces,*" Journal of Applied Physics **82**, 1860 (1997).

66. C. G. Van de Walle and D. Segev, "*Microscopic origins of surface states on nitride surfaces,*" Journal of Applied Physics **101**, 081704 (2007).

67. J. P. Long and V. M. Bermudez, "*Band bending and photoemission-induced surface photovoltages on clean* n - *and* p -*GaN (0001) surfaces,*" Physical Review B **66** (2002).

68. J. Yang, B. S. Eller, and R. J. Nemanich, "*Surface band bending and band alignment of plasma enhanced atomic layer deposited dielectrics on Ga- and N-face gallium nitride,*" Journal of Applied Physics **116**, 123702 (2014).

69. C. I. Wu, A. Kahn, N. Taskar, D. Dorman, and D. Gallagher, "*GaN (0001)-(1×1) surfaces: Composition and electronic properties,*" Journal of Applied Physics **83**, 4249 (1998).

70. S. L. Elliott, R. F. Broom, and C. J. Humphreys, "*Dopant profiling with the scanning electron microscope—A study of Si,*" Journal of Applied Physics **91**, 9116 (2002).

71. I. Müllerová, M. M. El-Gomati, and L. Frank, "*Imaging of the boron doping in silicon using low energy SEM,*" Ultramicroscopy **93**, 223 (2002).

72. M. M. El-Gomati and T. C. R. Wells, "*Very-low-energy electron microscopy of doped semiconductors,*" Applied Physics Letters **79**, 2931 (2001).

73. P. Kazemian, "*Effect of experimental parameters on doping contrast of Si p?n junctions in a FEG-SEM,*" Microelectronic Engineering **73–74**, 948 (2004).

74. L. Chernyak, A. Osinsky, V. Fuflyigin, and E. F. Schubert, "*Electron beam-induced increase of electron diffusion length in -type GaN and AlGaN/ GaN superlattices,*" Applied Physics Letters **77**, 875 (2000).

75. H. Fu, K. Fu, X. Huang, H. Chen, I. Baranowski, T.-H. Yang, J. Montes, and Y. Zhao, "*High Performance Vertical GaN-on-GaN p-n Power Diodes With Hydrogen-Plasma-Based Edge Termination,*" IEEE Electron Device Letters **39**, 1018 (2018).

76. D. Ji, W. Li, and S. Chowdhury,in *2016 IEEE 4th Workshop on Wide Bandgap Power Devices and Applications (WiPDA)* (IEEE, Fayetteville, AR, USA, 2016), pp. 114–117.

77. K. Fu, H. Fu, H. Liu, S. R. Alugubelli, T.-H. Yang, X. Huang, H. Chen, I. Baranowski, J. Montes, F. A. Ponce, and Y. Zhao, "*Investigation of GaN-on-GaN vertical* p - n *diode with regrown* p *-GaN by metalorganic chemical vapor deposition,*" Applied Physics Letters **113**, 233502 (2018).

78. Z. Hu, K. Nomoto, M. Qi, W. Li, M. Zhu, X. Gao, D. Jena, and H. G. Xing, "*1.1-kV Vertical GaN p-n Diodes With p-GaN Regrown by Molecular Beam Epitaxy,*" IEEE Electron Device Lett. **38**, 1071 (2017).

79. K. Fu, H. Fu, X. Huang, H. Chen, T.-H. Yang, J. Montes, C. Yang, J. Zhou, and Y. Zhao, "*Demonstration of 1.27 kV etch-then-regrow GaN p-n junctions with low leakage for GaN power electronics,*" IEEE Electron Device Lett. 1 (2019).

80. A. M. Armstrong, B. N. Bryant, M. H. Crawford, D. D. Koleske, S. R. Lee, and J. J. Wierer, "*Defect-reduction mechanism for improving radiative efficiency in InGaN/GaN light-emitting diodes using InGaN underlayers,*" J. Appl. Phys. **117**, 134501 (2015).

81. C. Haller, J.-F. Carlin, G. Jacopin, D. Martin, R. Butté, and N. Grandjean, "*Burying non-radiative defects in InGaN underlayer to increase InGaN/GaN quantum well efficiency*," Appl. Phys. Lett. **111**, 262101 (2017).

82. Y. Zhao, H. Fu, G. T. Wang, and S. Nakamura, "*Toward ultimate efficiency: progress and prospects on planar and 3D nanostructured nonpolar and semipolar InGaN light-emitting diodes*," Advances in Optics and Photonics **10**, 246 (2018).

83. Y.-J. Han, S. Xue, W.-P. Guo, C.-Z. Sun, Z.-B. Hao, and Y. Luo, "*Characteristics of n-GaN After Cl_2 /Ar and Cl_2 /N_2 Inductively Coupled Plasma Etching*," Jpn. J. Appl. Phys. **42**, 6409 (2003).

84. S. Tripathy, A. Ramam, S. J. Chua, J. S. Pan, and A. Huan, "*Characterization of inductively coupled plasma etched surface of GaN using Cl2/BCl3 chemistry*," Journal of Vacuum Science & Technology A: Vacuum, Surfaces, and Films **19**, 2522 (2001).

85. T. Narita, D. Kikuta, N. Takahashi, K. Kataoka, Y. Kimoto, T. Uesugi, T. Kachi, and M. Sugimoto, "*Study of etching-induced damage in GaN by hard X-ray photoelectron spectroscopy*," Phys. Status Solidi A **208**, 1541 (2011).

86. W. D. Rau, P. Schwander, F. H. Baumann, W. Höppner, and A. Ourmazd, "*Two-Dimensional Mapping of the Electrostatic Potential in Transistors by Electron Holography*," Phys. Rev. Lett. **82**, 2614 (1999).

87. S. Yazdi, T. Kasama, R. Ciechonski, O. Kryliouk, and J. B. Wagner, "*The measurement of electrostatic potentials in core/shell GaN nanowires using off-axis electron holography*," J. Phys.: Conf. Ser. **471**, 012041 (2013).

88. C. H. Seager, A. F. Wright, J. Yu, and W. Götz, "*Role of carbon in GaN*," Journal of Applied Physics **92**, 6553 (2002).

89. H. Xing, S. P. DenBaars, and U. K. Mishra, "*Characterization of AlGaN/GaNp-n diodes with selectively regrown n-AlGaN by metal-organic chemical-vapor deposition and its application to GaN-based bipolar transistors*," Journal of Applied Physics **97**, 113703 (2005).

90. M. Monavarian, G. Pickrell, A. A. Aragon, I. Stricklin, M. H. Crawford, A. A. Allerman, K. C. Celio, F. Leonard, A. A. Talin, A. M. Armstrong, and D. Feezell, "*High-Voltage Regrown Nonpolar m-Plane Vertical p-n Diodes: A Step Toward Future Selective-Area-Doped Power Switches*," IEEE Electron Device Lett. **40**, 387 (2019).

91. I. Stricklin, M. Monavarian, A. Aragon, G. Pickrell, M. Crawford, A. Allerman, A. Armstrong, and D. F. Feezell,in *Wide Bandgap Power and Energy Devices and Applications III*, edited by M. Matin, A. K. Dutta, and S. Chowdhury (SPIE, San Diego, United States, 2018), p. 1.

92. H. Katayama-Yoshida, T. Nishimatsu, T. Yamamoto, and N. Orita, "*Codoping method for the fabrication of low-resistivity wide band-gap semiconductors in p-type GaN, p-type AlN and n-type diamond: prediction versus experiment,*" J. Phys.: Condens. Matter **13**, 8901 (2001).

93. R. Y. Korotkov, J. M. Gregie, and B. W. Wessels, "*Codoping of wide gap epitaxial III-Nitride semiconductors,*" Nitride semiconductors No. 4, 9 (2002).

94. A. M. Soomro, C. Wu, N. Lin, T. Zheng, H. Wang, H. Chen, J. Li, S. Li, D. Cai, and J. Kang, "*Modified pulse growth and misfit strain release of an AlN heteroepilayer with a Mg–Si codoping pair by MOCVD,*" J. Phys. D: Appl. Phys. **49**, 115110 (2016).

95. T. Yamamoto and H. Katayama-Yoshida, "*Materials Design for the Fabrication of Low-Resistivity p-Type GaN Using a Codoping Method,*" Jpn. J. Appl. Phys. **36**, L180 (1997).

96. Y. Akatsuka, S. Iwayama, T. Takeuchi, S. Kamiyama, M. Iwaya, and I. Akasaki, "*Doping profiles in low resistive GaN tunnel junctions grown by metalorganic vapor phase epitaxy,*" Appl. Phys. Express **12**, 025502 (2019).

97. N. Asai, H. Ohta, F. Horikiri, Y. Narita, T. Yoshida, and T. Mishima, "*Impact of damage-free wet etching process on fabrication of high breakdown voltage GaN p–n junction diodes,*" Jpn. J. Appl. Phys. **58**, SCCD05 (2019).

APPENDIX A

LIST OF PUBLICATIONS DURING THE STUDY TOWARDS THE DOCTORAL DEGREE

SR Alugubelli, H Fu, K Fu, H Liu, Y Zhao, FA Ponce, "Dopant profiling in *p-i-n* GaN structures using secondary electrons" *Journal of Applied Physics* **126**, 015704 (2019).

SR Alugubelli, H Fu, K Fu, Y Zhao, MR McCartney, FA Ponce, "Electronic band structures of etched and regrown *p-i-n* GaN structures using electron holography". *Applied Physics Letters* **115**, 201602 (2019) DOI: 10.1063/1.5127014.

H Liu, H Fu, K Fu, SR Alugubelli, PY Su, Y Zhao, FA Ponce, "Non-uniform Mg distribution in GaN epilayers grown on mesa structures for applications in GaN power electronics" *Applied Physics Letters* 114 (8) 082102 (2019).

H Fu, K Fu, H Liu, SR Alugubelli, X Huang, H Chen, J Montes, TH Yang, C Yang, J Zhou, FA Ponce, Y Zhao, "Implantation-and etching-free high voltage vertical GaN p–n diodes terminated by plasma-hydrogenated p-GaN: revealing the role of thermal annealing" *Applied Physics Express* 12 (5) 051015 (2019).

K Fu, H Fu, H Liu, SR Alugubelli, TH Yang, X Huang, H Chen, I Baranowski, J Montes, FA Ponce, Y Zhao, " Investigation of GaN-on-GaN vertical p-n diode with regrown p-GaN by metalorganic chemical vapor deposition" Applied Physics Letters 113 (23), 233502 (2018).

H Fu, X Zhang, K Fu, H Liu, SR Alugubelli, X Huang, H Chen, I Baranowski, J Montes, FA Ponce, Y Zhao, "Nonpolar vertical GaN-on-GaN p–n diodes grown on free-standing m-plane GaN substrates" Applied Physics Express 11 (11), 111003 (2018).

K Mehta, YS Liu, J Wang, H Jeong, T Detchprohm, YJ Park, SR Alugubelli, S Wang, FA Ponce, S-C Shen, RD Dupuis, PD Yoder, “Lateral Current Spreading in III-N Ultraviolet Vertical-Cavity Surface-Emitting Lasers Using Modulation-Doped Short Period Superlattices” *IEEE Journal of Quantum Electronics* 55 (3) (2018).

K Mehta, YS Liu, J Wang, H Jeong, T Detchprohm, YJ Park, SR Alugubelli, S Wang, FA Ponce, S-C Shen, RD Dupuis, PD Yoder, “Theory and Design of Electron Blocking Layers for III-N-Based Laser Diodes by Numerical Simulation” *IEEE Journal of Quantum Electronics* 54 (6), 1-11 (2018).

K Mehta, T Detchprohm, YJ Park, YS Liu, O Moreno, SR Alugubelli, S Wang, FA Ponce, S-C Shen, RD Dupuis, PD Yoder, “High Reflectivity Hybrid AlGaN/Silver Distributed Bragg Reflectors for Use in the UV-Visible Spectrum” IEEE Journal of Quantum Electronics 53 (6), 1-8 (2017).